Collective Behavior of Self-Propelled Rods in Quasi-Two Dimensional Systems

Inaugural-Dissertation

zur

Erlangung des Doktorgrads

der Mathematisch-Naturwissenschaftlichen Fakultät

der Universität zu Köln

vorgelegt von

Masoud Abkenar

aus Teheran, Iran

Jülich 2014

Berichterstatter: Prof. Dr. Gompper

Prof. Dr. Dhont

Tag der mündlichen Prüfung: 27. Juni 2014

Zusammenfassung

Angetriebene mikroskopische Teilchen, z. B. Bakterien, Spermien und Proteinfilamente, zeigen Selbstorganisation in Strukturen wie Clustern, Wirbeln und Wellen. Einige dieser Strukturen sind mehrere Grössenordnungen größer als einzelne Schwimmer. Es ist oft noch unverstanden wie sich diese komplexen Strukturen bilden und wie sich "intelligente" Mechanismen für die Strukturbildung durch die Wechselwirkung der vielen "einfachen" Einheiten herausbilden. Die Erklärung der Strukturbildung ist jedoch nicht nur wichtig um das Verhalten der Schwimmer zu kontrollieren, sondern auch um die Eigenschaften "aktiver Materie" im Allgemeinen zu verstehen—von biologischen Mikroschwimmern und Nanorobotern für das gezielte Einbringen von Medikamenten bis hin zu neuartigen Materialien.

Das kollektive Verhalten von Mikroschwimmern wird auf der Basis verschiedener Modelle untersucht. Angetriebene Punktteilchen, die entsprechend vorgegebener Regeln wechselwirken, wurden in den letzten Jahren intensiv erforscht. Die Einfachheit dieser Modelle erlaubt die Anwendung analytischer Theorien, jedoch können solche Modelle keine Verbindung zwischen dem kollektiven Verhalten vieler Schwimmer und den physikalischen Wechselwirkungen zwischen einzelnen Schwimmern herstellen. Untersuchungen mit Hilfe von Modellen, die die physikalischen Wechselwirkungen zwischen stäbchenförmigen Teilchen berücksichtigen, deuten darauf hin, daß die sterischen Wechselwirkungen zusammen mit der Antriebskraft ausreichend sind um kollektive Strukturbildung zu erklären. Viele Aspekte, wie zum Beispiel der Einfluß von Teilchendichte, Teilchenform, Aktivität, Fluktuationen der Umgebung, Polydispersität, hydrodynamischer Wechselwirkungen und gegenseitiger Reibung, wurden noch nicht systematisch untersucht; ein komplettes Verständnis des kollektiven Verhaltens von Mikroschwimmern fehlt derzeit noch.

In dieser Arbeit wurde ein neuer Ansatz verwendet um das Verhalten angetriebener Stäbchen in der Nähe von Oberflächen zu simulieren. Anstelle des kompletten dreidimensionalen Systems—das sehr aufwendige Computersimulationen erfordert—werden Stäbchen untersucht, die sich nur in einer Ebene bewegen. Eine essentielle Eigenschaft des dreidimensionalen Systems wird jedoch beibehalten: die Stäbchen können sich durchdringen, wobei eine Energiebarriere überwunden werden muß. Dieser Ansatz kombiniert die Effizienz zweidimensionaler Simulationen mit der Möglichkeit Strukturen zu finden, die mit zweidimensionalen Modellen sich nicht durchdringender Stäbchen nicht zugänglich sind. Diese quasi-zweidimensionalen Systeme sind Teil einer Klasse aktiver Systeme, die sowohl Mikroschwimmer in der Nähe von Wänden als auch Filamente auf einem Substrat beinhaltet. Die Computersimulationen für zwei sich kreuzende Filamente sind konsistent mit Experimenten für Proteinfilamente, die sich in Motilitäts-Assays kreuzen.

Mit Hilfe von Monte-Carlo-Simulationen wird der Phasenübergang zwischen der isotropen und der nematischen Phase passiver Stäbchen untersucht. Zusätzlich zur Stäbchendichte ist die Energiebarriere für das Kreuzen der Stäbchen wichtig, um den Übergang zu bestimmen. Eine erweiterte Onsager-Theorie zur Bestimmung des Phasenübergangs der sich durchdringenden Stäbchen stimmt sehr gut mit den Simulationsdaten überein.

Simulationen der Langevin-Gleichung (Brownsche Dynamik) werden verwendet um die Strukturbildung für verschiedene Antriebskräfte der Stäbchen, Fluktuationen der Umgebung und Energiebarrieren für Überlapp zu untersuchen. Häufig werden große, wurmartige Cluster beobachtet, die mit hoher Richtungsstabilität in einem "Gas" zufällig orientierter, einzelner Stäbchen schwimmen. Die charakteristische Gasdichte der Stäbchen, sie sowohl durch Simulationen als auch durch einfache analytische Rechnungen charakterisiert wird, ist unabhängig von der Gesamtdichte der Stäbchen im System. Sie ist nur durch die Antriebskraft und die Länge einzelner Stäbchen bestimmt. Der Beginn der Clusterbildung korrelliert mit der charakteristischen Gasdichte und weist Ähnlichkeiten zur homogenen Keimbildung bei nicht angetriebenen Systemen auf. Obwohl die Wechselwirkungen zwischen Stäbchen rein repulsiv sind, können effektive Bindungsenergien im Cluster bestimmt werden. Diese Bindungsenergien sind vergleichbar mit Bindungsenergien, die in Kolloidlösungen gefunden wurden.

Im Gegensatz zu Modellen für Stäbchen, die sich nicht durchdringen können, führt beim vorliegenden Modell eine Erhöhung der Antriebskraft nicht notwendigerweise zur parallelen Orientierung der Stäbchen, da sich gleichzeitig die effektive Energiebarriere für das Kreuzen zweier Stäbchen erniedrigt, was die Clusterbildung vermindert. Bei starken Antriebskräften, für hohe Schimmgeschwindigkeiten, kreuzen sich einzelne Stäbchen und Cluster wieder häufiger, so daß das Modell ein "Fenster" für die Clusterbildung aufweist. Cluster werden für mittlere Antriebskräfte der Stäbchen beobachtet, wenn die Antriebskräfte groß genug sind um über die Fluktuationen der Umgebung zu dominieren und gleichzeitig klein genug sind, so daß die Stäbchen sich noch nicht einfach durchdringen können.

Polydispersität ist in den meisten experimentellen Untersuchungen von Mikroschwimmern unvermeidbar. In dieser Arbeit wird erstmalig geometrische Bidispersität in Suspensionen aktiver Teilchen untersucht, die aus kurzen und langen Stäbchen bestehen. Abhängig von Dichten und Längen der Stäbchen zeigen diese Systeme ein komplexes Phasenverhalten: eine ungeordnete Phase bei geringen Stäbchendichten, eine Phase mit einem Cluster der langen Stäbchen in Koexistenz mit einem Gas aus vorwiegend kurzen Stäbchen, eine Phase mit Clusterbildung sowohl der kurzen als auch die langen Stäbchen und eine "gemischte" Phase bei sehr hohen Stäbchendichten. Interessanterweise wird im bidispersen System Clusterbildung der langen Stäbchen auch in einem Bereich des Phasendiagramms beobachtet, in dem ohne die kurzen Stäbchen keine Clusterbildung auftreten würde.

Das vorab für homogene Systeme entwickelte Konzept der charakteristischen

Gasdichte kann zur Erklärung aller beobachteten Phasen im bidispersen System verwendet werden. Die Dichte und Länge der Stäbchen bestimmt sowohl die Clusterbildung, als auch die Phasentrennung von kurzen und langen Schwimmern. Für festen Stäbchen-Volumenanteil kann mit Hilfe der Simulationsdaten und analytischer Rechnungen eine kritische Länge der kurzen Stäbchen für den Entmischungsübergang bestimmt werden, die von der Antriebskraft der Stäbchen abhängt.

Abstract

Microscopic particles that swim by their own, such as bacteria, sperm cells, or protein filaments, self-organize into delicate structures like clusters, vortices, and wave-like ripples. Some of these structures are orders of magnitude larger than the size of a single swimmer. It is not yet understood how such complex structures form, or in other words, how "smart" mechanisms needed for constructing such structures arise from seemingly "dumb" units. Explaining the formation of these structures is not only important to control the behavior of the swimmers, but also to understand the properties of "active matter" in general, which span from biological microswimmers to nanorobots used in drug-delivery or advanced materials.

Several models have been suggested to explain the collective behavior of microswimmers. Self-propelled *point* particles that interact via imposed alignment rules have been studied to a great detail in the recent years. Although the simplicity of such models allows the formulation of analytical theories, these generic models cannot provide a connection between the structures they generate and the physical interactions that govern the motion of real microswimmers. Study of models that account for physical interactions between rodlike swimmers suggest that steric interactions between the particles together with self-propulsion are sufficient to explain many of the experimentally observed large-scale structures. However, the effects of the density of the particles, their shape, activity, environmental noise, polydispersity, hydrodynamic interactions, and frictional forces are not yet systematically investigated, and a complete picture for the collective behavior based on these parameters is missing.

In this study, we have devised a new approach to simulate self-propelled rods near substrates. Instead of simulating a full 3D system with rods—which is computationally very demanding—we map the rods to the 2D plane. The key idea is that, while doing so, we keep an essential feature of a 3D system: We allow the rods to intersect—as if they were crossing over each other in 3D—via a tunable energy barrier. This approach combines the efficiency of 2D simulations with the possibility to find structures that are unavailable using 2D models with impenetrable rods. Such self-propelled particles in quasi two dimensions describe a class of active systems that encompasses microswimmers close to a wall and filaments propelled on a substrate. Our detailed comparison shows that the way the swimmers intersect in our model is consistent with experiments in which protein filaments cross over each other in motility assays.

Using Monte Carlo simulations, we first determine the isotropic-nematic transition for passive rod suspensions. We show that, in addition to the density, the energy barrier for rod crossing controls the formation of a nematic phase for

penetrable rods. Moreover, we generalize the Onsager theory for the isotropic-nematic transition to the case of penetrable rods, and demonstrate its excellent agreement with our simulations.

Using Brownian dynamics simulations for self-propelled rods, we characterize cluster formation for rods as a function of propulsion strength, noise, and energy barrier. We find very large worm-like clusters that swim persistently inside a "gas" of randomly oriented rods. An important result is that self-propelled rods have a characteristic gas density. We demonstrate by performing both computer simulations and analytical calculations that this gas density is independent of the total rod density, and it only depends on the activity and the rod length. We argue that the onset of cluster formation for self-propelled rods is related to this characteristic gas density, and we discuss the similarities to homogeneous nucleation processes. Although the interaction between the rods is purely repulsive, we can also estimate a binding energy for rods that are part of a cluster. We show that this binding energy is comparable to the binding energies at the liquid-gas critical point in colloidal systems.

Contrary to models with impenetrable rods, an increase of the propulsion strength in our model does not only favor alignment, but also effectively decreases the potential barrier that prevents crossing of rods. We thus find that at high propulsion strengths (i.e. at high swimming velocities) individual rods and even clusters frequently pass through each other. We therefore find a "clustering window": Clusters only form at intermediate propulsion strengths, where the propulsion is strong enough to dominate the noise, but also weak enough so that rods cannot easily cross.

Polydispersity is inevitable in most experimental studies of microswimmers. For the first time, we study the effect of geometric bidispersity in active rod suspensions, where the system is composed of short and long rods. Depending on the density and the length of each rod species, we find a rich phenomenology for the bidisperse system: a disordered phase at low densities, a segregated phase with clusters of only the long rods, a phase where both long and short rods form giant clusters, and a "remixed" phase at very high densities. We also report on a phase where the presence of short rods imposes clustering of long rods in an otherwise homogeneous long-rod suspension.

We employ the concept of characteristic gas density that we developed earlier to explain the formation of all observed phases. We show that the density and the length of rods control the cluster formation and segregation of short and long swimmers. At fixed rod volume fractions, we measure the critical short-rod length for the mixing-demixing transition, and we show that this critical length depends on the activity of rods, in agreement with our analytical calculations.

Contents

Chapter 1

Introduction

Systems that contain a large number of units (e.g. molecules, cells, birds) sometimes exhibit collective phenomena: Every unit in the system behaves entirely differently than it would do alone, and the behavior is dominantly affected by the "others" in the system. Collective behavior is one of the most intriguing aspects of complex systems. Examples of collective behavior bridge over several orders of magnitude in length scales. Crystallization of matter, bacterial colonies, fish schooling, pedestrian lane formation, and tornadoes are just a few examples; see Fig. 1.1.

(a) ice crystal (b) Bacillus subtilis (c) Caranx latus

(d) pedestrian flow (e) tornado

Figure 1.1: Examples of collective behavior, from millimeters to kilometers: (a) Microscopic image of a dendritic ice crystal [1], (b) growth pattern of Bacillus subtilis bacteria [2], (c) schooling of Caranx latus (horse-eye jack) fish [3], (d) lane formation in pedestrian flow [4], and (e) early stage of formation of a tornado [5].

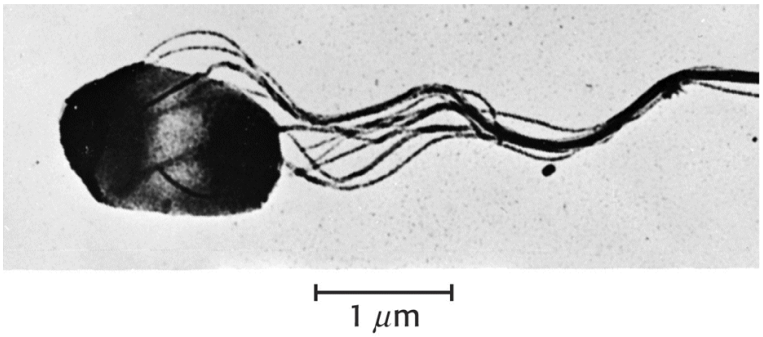

Figure 1.2: Salmonella swims by rotating a bundle of helical flagella. Figure is taken from Ref. [6].

In this thesis, we are interested in the collective behavior of microscopic swimming objects. We first review some examples for such "microswimmers", followed by a short review of the hydrodynamic equations. We then introduce important theoretical as well as experimental studies that have been performed on different systems of microswimmers in the recent years. We conclude this chapter by drawing an outline of the results in the current thesis.

1.1 Self-propelled particles

Movement is an essential part of life for many living organisms. For most animals, self-propulsion is often a way to find food, escape from predators, search for convenient environmental conditions (like temperature or acidity), or to find mates for reproduction. Movement is also important in the case of micro-organisms like cells and bacteria, where it actually means *swimming* in an often aqueous living environment. These microscopic swimmers use several different mechanisms for self-propulsion. Here we review a few of biological as well as artificial microswimmers.

1.1.1 Bacteria

Many bacteria like *Escherichia coli* [7] or *Salmonella* [6] swim using a helical filament that is attached to their body and is called flagellum; see Fig. 1.2. Rotation of several of such flagella causes a backward flow in the surrounding fluid, hence generates a reaction force that propels the bacterium forward [6–8]. Each flagellum rotates using a molecular motor that is anchored to the membrane of the bacterium.

While coordinated rotation of all flagella in a bacterium ideally generates a movement in a straight line, the bacteria actually swim using a process called "run-and-tumble"; see Fig. 1.3. The process works as follows: In the "run"

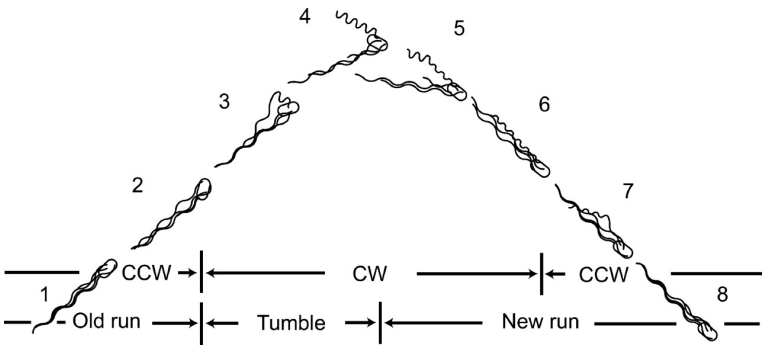

Figure 1.3: Bacteria like *E. coli* and *Salmonella* swim in a process called "run-and-tumble." While in the run phase swimming is on a straight direction, in the tumble phase the direction of motion changes due to the non-coordinated rotation of one or a few of the flagella. Figure is taken from Ref. [9].

phase, all flagella rotate synchronously, resulting in motion in a straight line. In the "tumble" phase, one or a few of the flagella start rotating in the opposite direction, which leads to a tumbling movement that changes the direction of motion for the bacterium, apparently randomly. Before the next "run" phase, all flagella become coordinated again, and the self-propulsion continues in the new acquired direction. Although the run-and-tumble process seems completely random, the bacterium actually regulates this process to search for better environmental conditions: If the bacterium feels that the conditions are improving upon moving in a particular direction, it extends the period of the run phase, and vice versa.

1.1.2 Sperm cells

Sperm cells swim using snake-like rippling of a flexible flagellum; see Fig. 1.4. Each sperm is composed of a spherical head and a long flagellum. While the head contains the nucleus and the genetic material, the flagellum tail is mostly

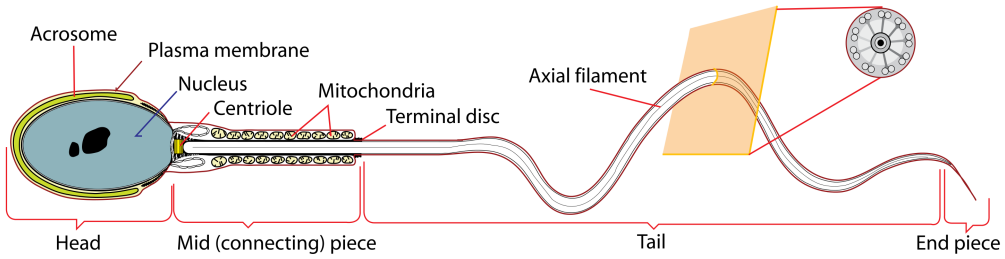

Figure 1.4: Schematic diagram showing a simple description of a human spermatozoon. Figure is taken from Ref. [10].

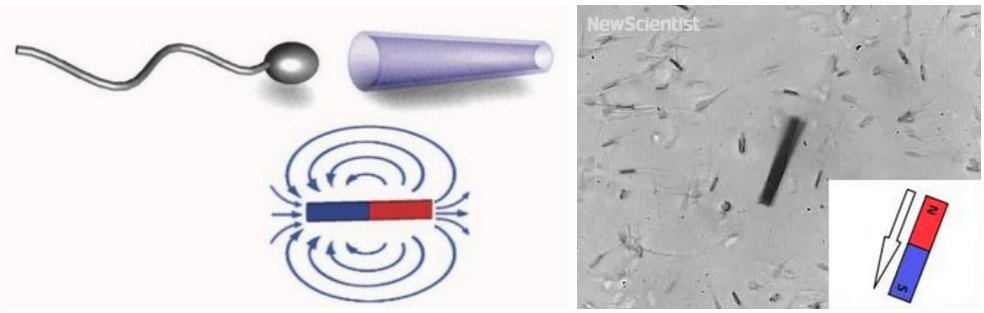

Figure 1.5: (a) Schematic diagram of a sperm-based biobot. (b) Snapshot of the biobot made of bull sperm cells. Figures are adapted from Ref. [12] and [13], respectively.

composed of several protein filaments called microtubules that are arranged in a joist-like structure. Using molecular motors that are placed between the filaments, these microtubules can slide along each other, causing the whole flagellum to bend. Sperm cells swim by actively deforming the flagellum, forming snake-like ripples that generate a backward flow, and employing the reaction force that pushes the sperm forward.

1.1.3 Artificial swimmers

There have been several attempts to construct artificial objects that can swim on their own. Motivations for constructing such micro- and nano-robots span from medical treatments to synthesizing advanced materials. One example of such artificial swimmers are metallic Pt-Au nanorods that are made of platinum at one end and gold at the other end [11]. When the rod is immersed in H_2O_2, a chemical reaction at the platinum end happens that causes a propulsion force for the rod.

Another example, which combines biological and non-biological mechanisms, are "sperm-based biobots" that combine the propulsion mechanism of sperm cells with the possibility to control the motion using external fields [12]; see Fig. 1.5. Microtubes made of magnetic material trap sperm cells that enter the tubes from their wider ends. The heads of the sperm are trapped, while their flagella are still free. The moving microtube can then be steered using an external magnetic field.

1.2 Life at low Reynolds number

In his famous lecture entitled *Life at low Reynolds number* (1977) [14], Edward Purcell pointed out that swimming in water for microscopic organisms is quite

different than for macroscopic objects like humans. While humans employ inertial effects to swim, these effects are negligible at the very different lengths and velocities of microswimmers. In fact, a good way to think about a bacterium swimming in water is to think about a human swimming in a very viscous fluid like grease or honey.

The difference between the swimming of macroscopic and microscopic objects can be easily demonstrated using the Navier-Stokes equation, which governs the dynamics of incompressible fluids. The Navier-Stokes equation is

$$\rho \left[\frac{\partial \mathbf{v}}{\partial t} + (\mathbf{v} \cdot \nabla)\mathbf{v} \right] = \eta \nabla^2 \mathbf{v} - \nabla p + \mathbf{f}_{\text{ext}} \,, \tag{1.1}$$

where $\mathbf{v} = \mathbf{v}(\mathbf{r}, t)$ is the instantaneous velocity of fluid at each point in space, ρ is the fluid density, η is the fluid viscosity, $p = p(\mathbf{r}, t)$ is the pressure, and $\mathbf{f}_{\text{ext}} = \mathbf{f}_{\text{ext}}(\mathbf{r}, t)$ is the external force that is applied to the fluid. Using the characteristic length L and velocity v_0 of the swimmer under consideration, this equation can be simplified if all variables are rescaled to their dimensionless forms,

$$\mathcal{R} \left[\frac{\partial \mathbf{v}'}{\partial t'} + (\mathbf{v}' \cdot \nabla)\mathbf{v}' \right] = \nabla^2 \mathbf{v}' - \nabla p' + \mathbf{f}'_{\text{ext}} \,. \tag{1.2}$$

While this dimensionless form of the Navier-Stokes equation has the same mathematical structure, the contributions from the physical properties of the system are all distilled in the dimensionless *Reynolds number*

$$\mathcal{R} = \frac{L \, v_0 \, \rho}{\eta} \,. \tag{1.3}$$

The Reynolds number, named after the British engineer and physicist Osborne Reynolds, characterizes the importance of inertial effects in the left hand side of the Navier-Stokes equation.

One can estimate a numerical value for the Reynolds number by substituting the density ρ and viscosity η of water, and the size L and the typical velocity v_0 of a swimmer under consideration. We find the Reynolds number

$$\mathcal{R} \approx 10^4 \tag{1.4}$$

for human swimming in water and

$$\mathcal{R} \approx 10^{-4} \tag{1.5}$$

for bacteria swimming in water. This means that while inertial effects are very important for swimming of a human in water, they can be safely neglected in the case of microswimmers: For a bacterial swimmer, motion stops immediately when it ceases to generate a propulsion force. In this case, the left hand side

(a) (b) (c)

Figure 1.6: (a) Flock of starling. (b) Reconstruction of the 3D velocities of birds in a flock. (c) A linear relation between correlation length of the velocity fluctuations and the flock size indicates that the correlations are scale-free. Figures are taken from Ref. [28].

of Eq. (1.2) is practically zero, and the motion is governed by the much simpler Stokes equation,

$$\nabla p - \eta \nabla^2 \mathbf{v} = \mathbf{f}_{\text{ext}} \,. \tag{1.6}$$

Contrary to the nonlinear and chaotic Navier-Stokes equation, the Stokes equation in Eq. (1.6) is both linear and time-independent. An important consequence of this fact is the "scallop theorem" formulated by Purcell: A reciprocal motion (like opening and closing of a scallop shell) is insufficient to generate a net movement, even if the two steps are performed at different speeds. Because of the scallop theorem, microswimmers generate motion using a set of movements that breaks the time symmetry, i.e., the motion is different when the movie is played backward in time.

1.3 Experimental studies

Collective behavior of active bodies is frequently found in macroscopic systems such as bird flocks and fish schools [15], but also is found in microscopic systems such as sperm cells [16,17], bacteria [18–21], motility assays with protein filaments [22, 23], and manmade microswimmers that propel themselves forward using a chemical or physical mechanism [11, 24–27].

1.3.1 Flocking of birds

Birds are known to flock for increased foraging efficiency and to defend against predators [29]. Recently, individual velocities and 3D positions of birds in starling flocks have been measured; see Fig. 1.6. It has been shown that the correlations between the velocity fluctuations of individual birds increase with the flock

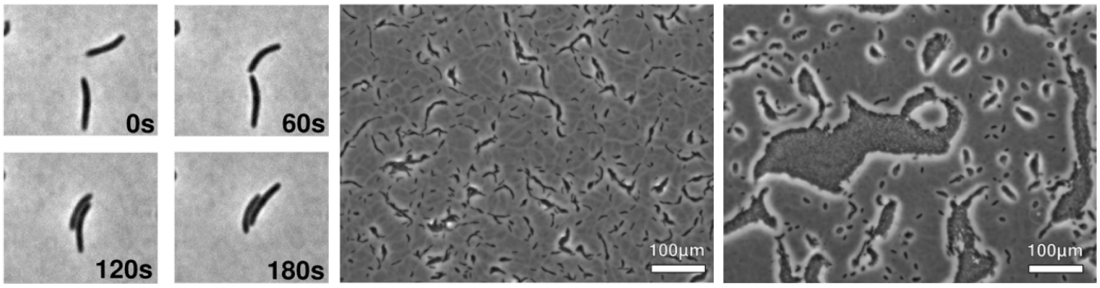

(a) (b) (c)

Figure 1.7: Cluster formation for *Myxococcus xanthus* bacteria gliding on an agar substrate. The bacteria are approximately 4μm long and have aspect ratios $a = 9 \pm 2$. (a) Bacteria align when they collide. (b) At low packing fractions, small clusters form. (c) At high packing fractions, very large clusters are observed. Figures are taken from Ref. [20].

size [28]. Such scale-free correlations suggest that bird flocks behave as critical systems to increase the efficiency for response to environmental perturbations.

1.3.2 Clustering of bacteria

Many types of bacteria are known to aggregate and form clusters. For example, *Myxococcus xanthus* bacteria which glide on an agar substrate form clusters above a critical concentration of the bacteria [20, 30]. Bacteria align when they collide, which results in cluster formation; see Fig. 1.7(a). At low densities, only small clusters form, and the cluster size distribution (CSD) decays like a scale-free power law, as predicted by previous simulations [31–35]; see Fig. 1.7(b). At high packing fractions, a second peak in the CSD appears at high cluster sizes, indicating the formation of large clusters; see Fig. 1.7(c).

1.3.3 Structure formation in motility assays

Biological microswimmer systems are often mimicked by minimal "toy models", since it is easier to control the experimental conditions in these model systems, and to isolate the effect of different physical interactions. One class of such model systems are motility assays [22, 23] in which protein filaments move using a "carpet" of propelling molecular motors that are anchored to the substrate; see Fig. 1.8(a).

Motility assays with actin filaments have been studied and shown to form large-scale structures at different filament densities. Those include moving clusters, swirls, and ripples of low- and high-density regions, called density waves; see Fig. 1.8(b). The lateral dimension of each wave front of those waves is about 50 times the length of each actin filament [22]. Although phenomenological models

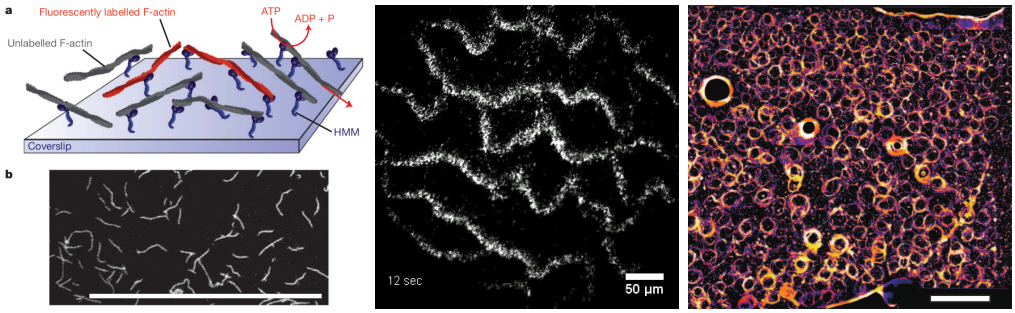

(a) (b) (c)

Figure 1.8: (a) Schematic diagram of a motility assay with actin filaments. Filaments (red and gray) move upon temporarily binding to molecular motors (blue). Only a fraction of the filaments are fluorescently labeled. (b) Wave-like density inhomogeneities (density-waves) at high densities of actin filaments. The structures move to the top right. Figures are taken from Ref. [22]. (c) Large-sclae lattice of vortices in motility assays with microtubules. Scale bar is 2 mm. Figure is adapted from Ref. [23].

that will be discussed in Sec. 1.4 (including a cellular automaton model presented in Ref. [22]) can reproduce the formation of density waves, no model with physical interactions is known that can generate such density wave structures.

In another experiment with microtubules that were propelled on a surface by molecular motors, the filaments spontaneously self-organized into vortices, inside which they move in both directions. Some of the vortices have diameters of about 30 times the length of a single filament [23]. On longer timescales, the vortices form a lattice structure; see Fig. 1.8(c).

1.4 Theoretical approaches

Microswimmers are a very interesting class of systems that exhibit collective behavior. The different manifestations of collective behavior are studied—and sometimes understood to a quantitative level—using statistical physics. In *equilibrium* systems, a systematic understanding of a wide range of physical phenomena has been made possible for the last several decades, using concepts like phase transitions, scaling, and universality.

In the last 20 years, the investigation of systems that are far from equilibrium has found increasing attention. Most biological processes such as swarm behavior, cell locomotion, and viscous flows are of non-equilibrium nature. Many of these systems exhibit remarkable features that are reminiscent of equilibrium systems, such as dynamic phase transitions and scaling of order parameters. Considering the very rich phenomenology of such nonequilibrium systems, however, a deep

(a) (b) (c) (d)

Figure 1.9: Snapshots of systems of self-propelled point particles in the Vicsek model. (a) Random initial configuration of points. (b) For small densities and noise, motile clusters are found that move in random directions. (c) For high densities and noise particles move randomly but with some correlation. (d) For high density and small noise, all particles move orderly in a spontaneously chosen direction. Figure is taken from Ref. [36].

understanding of the phenomena in terms of a unified picture of statistical physics is still missing.

1.4.1 The Vicsek model

Study of self-propelled particles (SPPs)—one important class of nonequilibrium systems—brought to the attention of many physicists for the first time by the pioneering study of Vicsek *et al.* (1995) [36]. In the short paper entitled "Novel Type of Phase Transition in a System of Self-Driven Particles," Vicsek and coauthors proposed a step-wise model which, in spite of its striking simplicity, could exhibit interesting dynamical properties. The proposed model which is now called the Vicsek Model (VM) consists of N polar point particles that move on a two-dimensional plane with periodic boundary conditions; see Fig. 1.9. The entire dynamics of the system can be summarized in the following simple rule:

> "[A]t each time step a given particle driven with a constant absolute velocity assumes the average direction of motion of the particles in its neighborhood of radius r with some random perturbation added." [36]

By means of computer simulations, Vicsek and coauthors showed that the system undergoes transitions from disordered phases with vanishing average velocity [Fig. 1.9(a)] to ordered phases where all particles move in the same spontaneously chosen direction [Fig. 1.9(d)].

Given the position $\mathbf{x}$, velocity $\mathbf{v}$ and the direction θ for particles, the equations of motion for particle i at time $t+1$ are

$$\mathbf{x}_i(t+1) = \mathbf{x}_i(t) + \mathbf{v}_i(t)\Delta t\,, \tag{1.7}$$

$$\theta_i(t+1) = \langle\theta(t)\rangle_r + \Delta\theta\,, \tag{1.8}$$

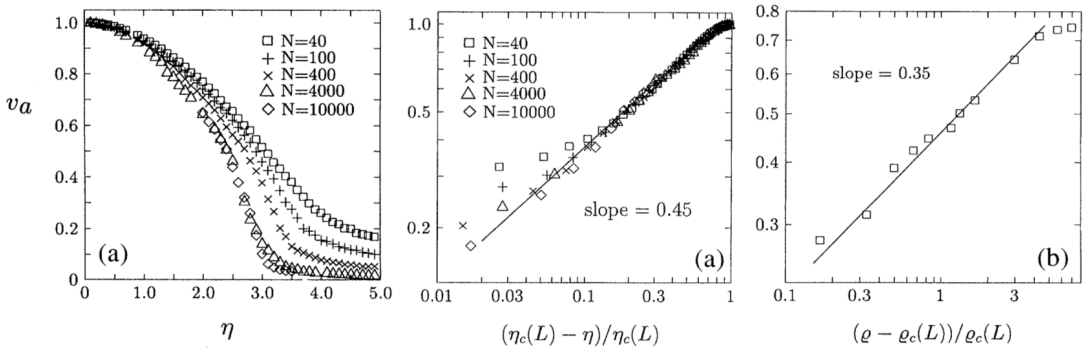

Figure 1.10: Phase transitions for systems of self-propelled point particles in the Vicsek model. (a) The order parameter v_a [Eq. (1.9)] vs noise η for a fixed density ρ and different system sizes. (b) and (c) The assymptotic behavior of v_a with respect to η and ρ, respectively. The slopes give the critical exponents β and δ. Figure is taken from Ref. [36].

where $\langle\theta(t)\rangle_r$ is the average over the orientations of all particles within a circle of radius r, and $\Delta\theta$ is a random noise term which is drawn uniformly from the interval $[-\eta/2, \eta/2]$. The important parameters in the Vicsek model are therefore the density of the particles ρ, the noise strength η, and the propulsion velocity v in units of $r/\Delta t$.

Using the magnitude of the average velocity as an order parameter,

$$v_a = \frac{1}{Nv} \left| \sum_{i=1}^{N} \mathbf{v}_i \right| , \tag{1.9}$$

one could identify kinetic phase transitions by changing η and ρ, as shown in Figs. 1.10(a)–1.10(c). The transitions are analogous to continuous phase transitions in equilibrium systems, characterized by the scaling relations

$$v_a \sim [\eta_c(\rho) - \eta]^{\beta} \tag{1.10}$$

and

$$v_a \sim [\rho - \rho_c(\eta)]^{\delta} . \tag{1.11}$$

Vicsek and coauthors found $\beta = 0.45 \pm 0.07$ and $\delta = 0.35 \pm 0.06$ from their simulations. They proposed that the observed behavior is the sign of an effective long-range interaction due to the particle mixing in the system. However, it was shown later that this transition is of discontinuous type, and the apparent continuity in Ref. [36] is due to strong finite-size effects [37].

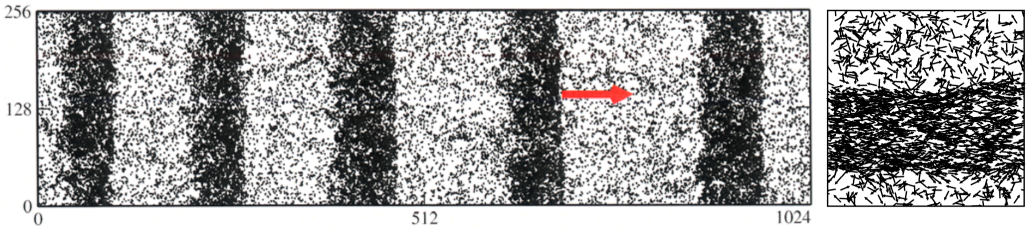

(a) (b)

Figure 1.11: (a) Formation of density waves in the Vicsek model. The red arrow shows the average direction of motion. Figure is taken from Ref. [53]. (b) Particles move along the nematic bands in the modified Vicsek model with nematic alignment rule. Figure is taken from Ref. [50].

1.4.2 Beyond the Vicsek model

The pioneering work of Vicsek *et al.* [36] demonstrated nonequilibrium phase transitions for systems with self-propelled point particles. This work led to numerous analytical [38–44] as well as computational [31, 37, 45–52] studies for systems of self-propelled particles. Here, we review some of the subsequent literature that focused on polar *point* particles. Later in Sec. 1.4.3, we review the models that use *rodlike* self-propelled particles.

Shortly after the introduction of the Vicsek model (VM), a phenomenological continuum model was proposed [38] that could reproduce similar behavior as the original VM. The model consisted of a density field $\rho(\mathbf{r}, t)$ and a polarization field $\mathbf{p}(\mathbf{r}, t)$, and was constructed only based on symmetry arguments. It was found that the model results in true long-range order, similar to that observed in the VM. Moreover, it was shown that the continuum model describes a large universality class of systems that, in two dimensions, includes the VM.

It was also shown that the original VM also results in elongated, laterally moving density inhomogeneities (density waves) [53]; see Fig. 1.11(a). Moreover, variants of the VM were proposed, for example by the introduction of cohesion via a short-range attractive interaction between the particles [54]. It was shown that cohesion results in asymmetric motile flocks, where the flocks break near the onset of long-range collective motion [37]. Another variation of the VM is the case where the polar particles interact via a nematic alignment rule, that is, where particles orient parallel or antiparallel depending on the angle between their orientations. It was shown that this system—which resembles the interaction of rodlike self-propelled particles (rSPPs)—forms nematic bands, in which the particles move along the band in both directions [50]; see Fig. 1.11(b). Recently, the different spatial structures arising from the VM have been derived using a unifying dynamical-system framework [55].

1.4.3 Rodlike microswimmers

Many realizations of self-propelled particles have elongated shapes. Examples include sperm cells [16], platinum-gold nanorods [11], and various motile bacteria such as *Myxococcus xanthus* [56] and *Escherichia coli* [57]. As we discussed in Sec. 1.4.2, the nature of the interaction between self-propelled particles has a drastic effect on the their collective behavior. Contrary to Vicsek-like models for self-propelled particles, where the interaction between particles is imposed explicitly, models with rodlike particles consider interactions that result from physical mechanisms, e.g. steric and/or hydrodynamic interactions between the rods. These models are therefore applicable to a narrower class of SPP systems, but with more specificity.

Inspired by the collective motion of gliding bacteria, a two-dimensional model of self-propelled rods that interact via excluded volume interaction was studied [32]. It was shown using computer simulations that self propulsion can induce cluster formation, which is otherwise absent for rod-shaped objects. This result implies that the aggregation of elongated motile bacteria can be explained, at least partly, by the simple physical mechanism of contact forces between colliding bacteria, as opposed to other mechanisms such as chemical signaling.

Self-propulsion also enhances the tendency of rodlike swimmers to form nematic order, as found in a model of cytoskeletal filaments in motility assays [58]. In a system of hard rods that interact via repulsive interactions and Langevin dynamics, it was found that increasing the surface density of both filaments and motor proteins enhances the formation of a nematic phase for the filaments, as compared to the case of purely passive rods with no motor activity [59]. This finding was later confirmed by a modified Smoluchowski equation for self-propelled rods in two dimensions, in which the collisions between rodlike objects were considered [60]. Solution of the modified Smoluchowski equation revealed that self-propulsion decreases the critical density for the isotropic-nematic transitions, and that boundary effects are strongly enhanced in confined self-propelled systems.

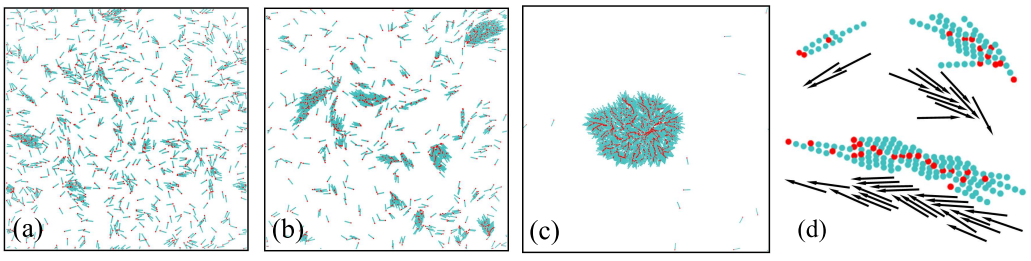

Figure 1.12: Snapshot of self-propelled rod systems. (a) Isotropic phase for low densities and high noise. (b) Motile clusters for intermediate densities and noise. (c) Giant jammed cluster for high densities and low noise. (d) Close-up of some clusters, showing the internal structure. Figure is taken from Ref. [34].

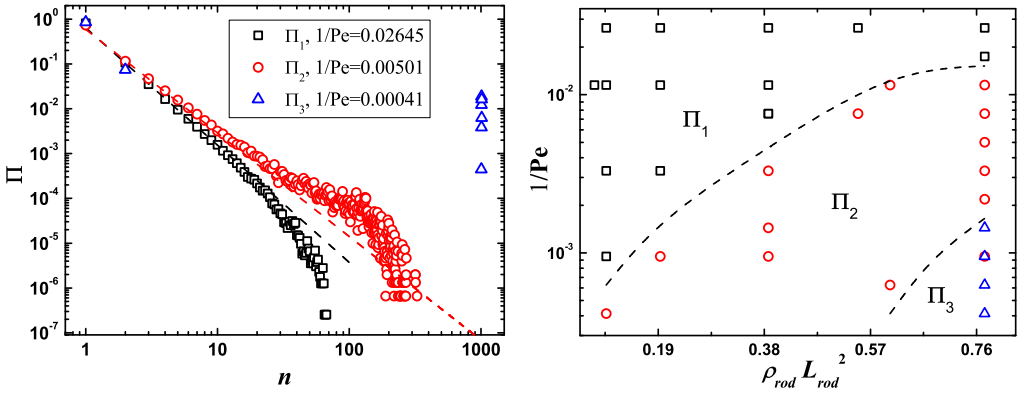

Figure 1.13: (left) Cluster size distributions for the systems shown in the snapshots of Fig. 1.12. Π_1: Fig. 1.12(a); Π_2: Fig. 1.12(b); Π_3: Fig. 1.12(c). (right) Dynamical phase diagram for the systems with varying density ρ_{rod} and noise 1/Pe, corresponding to the different types of cluster size distributions. The dashed lines are guides to the eye. Figure is taken from Ref. [34].

The effect of hydrodynamic fluctuations on the collective behavior of self-propelled rods was investigated using a slender hard-rod model in three dimensions, where the rods propel themselves by exerting a tangential shear on the surrounding fluid over a fraction of their body [61]. It was shown by hydrodynamic simulations that nematic suspensions of hard rods in 3D are unstable at long wavelengths as a result of hydrodynamic fluctuations, which is consistent with analytical calculations [39]. Nevertheless, rods were observed to locally form nematic order. This short-range ordering affects the average rod swimming speed: for puller (pusher) rods, where the stress actuation is applied near the head (tail) of the rod, the average swimming speed is decreased (increased).

Cluster formation in self-propelled hard rods were studied using Brownian dynamics simulations in two dimensions [34]. The rods are affected by noise, while they propel themselves forward using an intrinsic propulsion force, and interact segment-wise via a truncated Lennard-Jones potential. By analyzing cluster size distributions, three distinct phases in suspensions of rSPPs were observed: an isotropic phase at low densities and high noise, where the rods are homogeneously distributed and randomly oriented [Fig. 1.12(a)], a giant immobile cluster at high densities and low noise, where most rods are jammed in the single cluster [Fig. 1.12(c)], and "living clusters" at intermediate densities and noise, where large polar clusters form that move in different directions [Fig. 1.12(b)]. A phase diagram of the system is shown in Fig. 1.13.

The effect of aspect ratio and density was studied in simulations of self-propelled hard rods without noise that interact segment-wise via a shifted Yukawa potential [62]; see the phase diagram in Fig. 1.14(a). At low densities and aspect ratios, an isotropic phase is observed. At very high densities, a jammed phase,

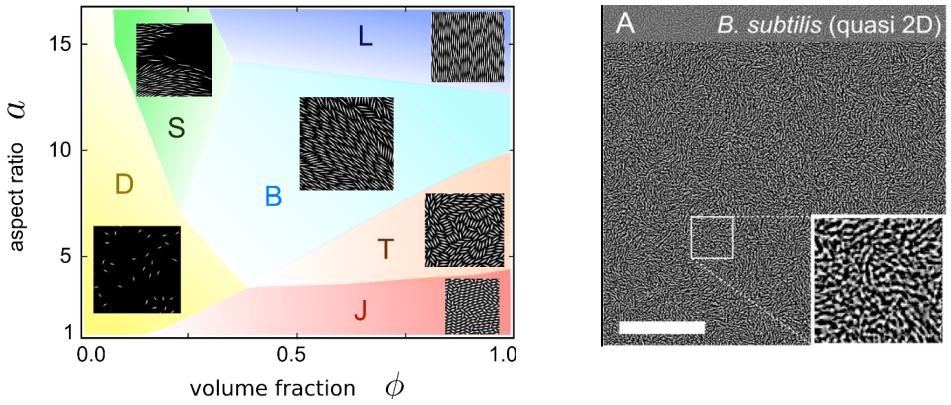

(a) (b)

Figure 1.14: (a) Dynamical phase diagram for self-propelled hard rods with varying volume fraction ϕ and aspect ratio a: dilute state (D), jamming (J), swarming (S), bionematic phase (B), turbulence (T), and laning (L). (b) A homogeneous bacterial suspension at high concentration in quasi two dimensions. Figures are adapted from Ref. [62].

a turbulent phase, and a laning phase with increasing rod aspect ratios between $1 \lesssim a \lesssim 15$ are observed, respectively. At intermediate densities and aspect ratio $a \approx 10$, a bionematic phase appears, while at higher aspect ratios $a \gtrsim 14$, a direct transition from swarming (dynamic cluster formation) phase to the laning phase with increasing density is found.

Recently, a bidisperse system has been studied that consists of a mixture of rods with and without motility [63]. It was found that the difference in collision frequencies between active and passive rods leads to segregated cluster formation. A laning phase is also found at high densities, where streams of active rods move between bands of passive rods, until the lanes break down due to splay fluctuations.

1.5 Outline of this thesis

In this thesis, we focus on rodlike microswimmer systems in quasi-two dimensions. We perform computer simulations in which the rods move on a substrate or near a wall, while having a finite probability to move to the bulk to cross each other [35]. In chapter 2, we introduce the penetrable rod model that we have developed and used throughout this thesis. In chapter 3, we first study the properties of *passive* penetrable rods using Brownian dynamics and Monte-Carlo simulations. Then in chapter 4, we present results on the cluster formation for *monodisperse* (single-component) active rod systems. We study the collective behavior by characterizing densities, cluster size distributions, and orientation

autocorrelations, and we demonstrate how the cluster formation depends on the density, propulsion force, and the energy barrier for rod crossing. Finally in chapter 5, we extend our study to bidisperse systems that are composed of rods with two different lengths [64]. We show that short and long rods segregate depending on their length and densities. We summarize and conclude our main results in chapter 6, followed by an outlook for future studies in chapter 7.

Simulation snapshots of the system which display disordered states, motile clusters, lanes, etc. are shown in Fig. 1.15. More snapshots and movies can be found in the Supplemental Material of Refs. [35] and [64].

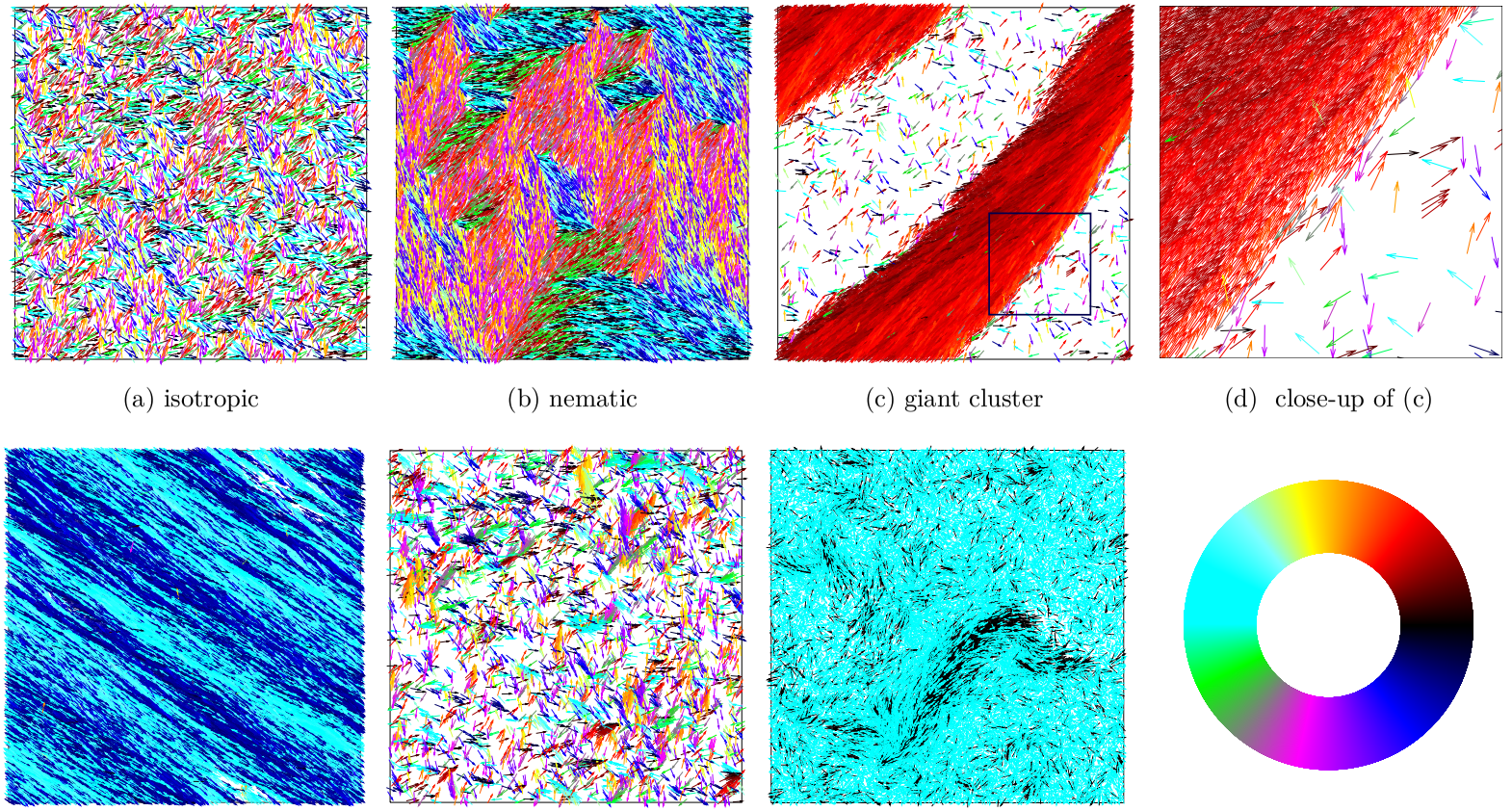

(a) isotropic (b) nematic (c) giant cluster (d) close-up of (c)

(e) laning (f) cluster breakup (g) segregation (h) color coding for rod orientation

Figure 1.15: Snapshots of self-propelled rod systems simulated using Brownian dynamics simulations. (a)–(f) Each rod is colored based on its orientation, according to (h). (a) Isotropic state at low scaled density $\rho\, L_{\mathrm{rod}}^2 = 5.1$ and zero Péclet number $\mathrm{Pe} = 0$, (b) nematic state at high $\rho\, L_{\mathrm{rod}}^2 = 10.2$ and $\mathrm{Pe} = 0$, (c) giant cluster at medium $\mathrm{Pe} = 25$ and $\rho\, L_{\mathrm{rod}}^2 = 10.2$, (d) close-up of the boundary of a giant cluster, (e) laning phase at high $\rho\, L_{\mathrm{rod}}^2 = 25.5$ and $\mathrm{Pe} = 75$ (f) cluster break-up at high $\mathrm{Pe} = 100$ and $\rho\, L_{\mathrm{rod}}^2 = 5.1$, (g) partial segregation of short (blue) and long (black) rods, (h) color coding for rod orientation. For movies, see the Supplemental Material of Refs. [35] and [64].

Chapter 2

The penetrable rod model

2.1 Motivation

The collective behavior of microswimmers has gained considerable attention in the recent years, partly because the computational resources needed for these studies have become available. Examples of such microswimmers span from biological cells and bacteria, to human-made nano-robots.

A model system for studying the collective behavior of microswimmers are motility assays, where for example actin filaments move on a substrate crafted with heavy meromyosin (HMM) motors [22]. The filaments are approximately 10μm long, move with average speed $v_0 \sim 5\mu\text{ms}^{-1}$, and the filament density is about 20 filaments per square micrometer. In such motility assays, a rich phenomenology of collective behavior has been observed. This includes the formation of filament clusters, swirls, and large-scale laterally-moving density inhomogeneities (density waves). The directional persistence of the motile clusters increases with increasing filament density.

For *Myxococcus xanthus* bacteria [20, 30], gliding colonies (moving clusters) that move on agar plates have been observed [20]. The bacteria have an average length of 3.6μm, an aspect ratio of about 9, and an average speed of $0.05\mu\text{ms}^{-1}$. The transition to cluster formation happens at packing fraction of around 17 %, with a scale-free (power-law) decay in the cluster size distribution, with an exponent of $\beta = -1.88 \pm 0.07$ [1].

Motility assays and gliding bacteria are essentially two-dimensional systems, but with a finite probability for the swimmers to cross each other [23, 65]. Because the swimmers are not tightly bound to the surface, one of them might be slightly and temporarily pushed away from the surface when two swimmers collide. In Ref. [23], microtubules have been found to cross each other with a probability of 40 % if they approach perpendicularly. Two-dimensional models with

[1] The reported value in Ref. [20] is $\gamma_0 = 0.88 \pm 0.07$, which connects to our exponent via $\beta = -\gamma_0 - 1$; see Sec. 4.4

impenetrable swimmers thus do not adequately describe these systems, while full three-dimensional calculations are computationally expensive. In Ref. [22], a cellular automaton model with an imposed alignment rule that allows two filaments to occupy the same site has been used to simulate actin motility assays.

In this chapter, we propose a model for self-propelled rods (SPRs) in two dimensions that interact with a physical interaction potential. We discretize each rod by a number of beads to calculate rod-rod interactions. In contrast to previous models with strict excluded-volume interactions [32, 32, 34, 58, 62, 63], our capped interaction potential allows rods to cross. Our simulations thus combine the computational efficiency of two-dimensional simulations with a possibility to mimic an escape to the third dimension when two rods collide. Simulation snapshots of the system which display disordered states, motile clusters, lanes, etc. are shown in Fig. 1.15, and movies can be found in the Supplemental Materials of Refs. [35] and [64].

2.2 Basics of Brownian dynamics simulations

Here we briefly review Brownian motion and Brownian dynamics simulations. The details of the simulation for the particular case of self-propelled rods are explained in Sec. 2.3.

In biological systems and suspensions, the motion of particles are always affected by the interaction with surrounding molecules. The random motion of the particles in solution, known as Brownian motion, is due to collisions of the solute particles with the fast-moving molecules of the gas or liquid solvent. From a fundamental point of view, the Brownian motion can be understood by considering the motion of all particles of both solute and solvent. However, since we are mostly interested in the motion of the solute rather than the solvent particles, we employ Brownian dynamics.

The Brownian dynamics (BD) simulation is a mesoscopic approach to model particles that are influenced by thermal/environmental noise. In Brownian dynamics simulations, the fluid molecules are not explicitly considered. Rather, the effect of the fluid is modeled by friction forces and stochastic forces that are applied to the particles. This approach is only valid if the characteristic time scale for the particles of interest is much larger than that of fluid molecules. In biological systems and in solutions of colloids and polymers, this is often the case. Therefore, the very fast dynamics of fluid molecules is coarse grained so that the study of the much slower dynamics for the rest of the system becomes possible for much larger time scales.

The motion of the particles in BD simulations is given by the Langevin equation [66]. For the simplest case of a one-dimensional system with coordinate $x(t)$,

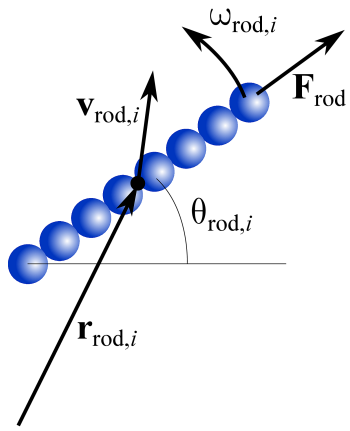

Figure 2.1: Schematic representation of the model of a self-propelled rod and coordinates used in two dimensions. The rod is discretized into n_b beads to calculate the rod-rod interaction.

the Langevin equation is

$$\gamma \frac{dx}{dt} = -\frac{d\Phi}{dx} + \xi(t)\,, \tag{2.1}$$

where γ is the friction coefficient, $\Phi = \Phi(x)$ is an external potential, and $\xi(t)$ is a stochastic force acting on the particle at time t. The exact time-dependence of $\xi(t)$ is not known. However, we assume that $\xi(t)$ is drawn from a Gaussian distribution

$$P(\xi) \propto \exp(-\frac{1}{2\sigma^2}\,\xi^2)\,, \tag{2.2}$$

with average $\langle \xi \rangle = 0$ and spread

$$\sigma = \langle \xi^2 \rangle^{1/2} = (2\gamma k_{\mathrm{B}} T)^{1/2}\,. \tag{2.3}$$

It can be shown that the Gaussian distribution for the stochastic force leads to the same dynamics as predicted by e.g. the Smoluchowski equation [66]. The value for σ in Eq. (2.3) is chosen such that that the fluctuation-dissipation theorem is fulfilled. In conclusion, Eq. (2.1) provides a suitable framework for modeling systems of particles that are affected by noise and inter-particle interactions.

2.3 The forces

Our systems of self-propelled rods consist of N_{rod} rods in a two-dimensional box of size $L_x \times L_y$ with periodic boundary conditions; see Fig. 1.15. In our simulations,

the rods are characterized by their center-of-mass positions $\mathbf{r}_{\mathrm{rod},i}$, their orientation angles $\theta_{\mathrm{rod},i}$ with respect to the x axis, their center-of-mass velocities $\mathbf{v}_{\mathrm{rod},i}$, and their angular velocities $\omega_{\mathrm{rod},i}$; see Fig. 2.1.

Our penetrable rods in the Brownian dynamics simulations are affected by three types of forces, which will be explained in the following sections: the intrinsic propulsion force, the forces arising from thermal/environmental noise, and the steric interaction force between rods. To calculate the forces on each rod, we decompose the rod velocity into parallel and perpendicular components with respect to its axis, $\mathbf{v}_{\mathrm{rod},i} = \mathbf{v}_{\mathrm{rod},i,\parallel} + \mathbf{v}_{\mathrm{rod},i,\perp}$. In each simulation step, the velocities are calculated using

$$\mathbf{v}_{\mathrm{rod},i,\parallel}(t) = \frac{1}{\gamma_\parallel}\left(\sum_{j\neq i}^{N_{\mathrm{rod}}} \mathbf{F}_{ij,\parallel} + \xi_\parallel \mathbf{e}_\parallel + F_{\mathrm{rod}}\mathbf{e}_\parallel\right), \tag{2.4}$$

$$\mathbf{v}_{\mathrm{rod},i,\perp}(t) = \frac{1}{\gamma_\perp}\left(\sum_{j\neq i}^{N_{\mathrm{rod}}} \mathbf{F}_{ij,\perp} + \xi_\perp \mathbf{e}_\perp\right), \tag{2.5}$$

and

$$\omega_{\mathrm{rod},i}(t) = \frac{1}{\gamma_r}\left(\sum_{j\neq i}^{N_{\mathrm{rod}}} M_{ij} + \xi_r\right), \tag{2.6}$$

where $\mathbf{e}_\parallel$ and $\mathbf{e}_\perp$ are unit vectors parallel and perpendicular to the rod axis, respectively. F_{rod} is the propulsion force for each rod, as explained in Sec. 2.3.1. The friction coefficients and the noise terms are denoted by γ and ξ, respectively, as explained in Sec. 2.3.2. Finally, $\mathbf{F}_{ij}$ and M_{ij} are the force and torque due to the interaction with other rods, as explained Sec. 2.3.3.

2.3.1 Propulsion force

Self-propelled systems utilize different mechanisms for the generation of the swimming force. In motility assays with protein filaments, the propulsion force comes from the activity of molecular motors that bind to the filaments and push them forward (e.g. myosin in case of actin filaments [22] and dynein in case of microtubules [23]). In bacterial suspensions, the propulsion comes from the specific biological apparatus that is responsible for motility. For example, in sperm cells it comes from the hydrodynamic interaction between the wave-like motion of the sperm flagella and the surrounding fluid [67]. In *E. coli* bacteria, the propulsion comes from the rotating motion of spiral-shaped flagella [9]. In Myxobacteria, the cells propel themselves by crawling on the substrate, utilizing the active polymerization and depolymerization of their membrane filaments [68].

In our model, however, we do not focus on the exact mechanism that generates the propulsion force. Rather, we are interested in a generic model that can

be applied to a broad range of rod-like self-propelled systems. Therefore, we model the propulsion mechanism by a constant force F_{rod} that is applied to each rod, at every simulation time-step; see Eq. (2.4). This force is always added to the interaction forces due to other rods and the forces that are coming from thermal/environmental noise. Overall, these three types of forces determine the motion of the rod. We assign an inherent polarity to each rod, so that the propulsion force F_{rod} is always applied to one end (the "head") of the rod.

2.3.2 Friction and noise

We assume that the rods swim in an overdamped medium, so that the Reynolds number Re is very small. This assumption holds e.g. for biological microswimmers, where the Reynolds number is of the order of $\mathrm{Re} \approx 10^{-5}$. In such low Reynolds numbers, inertia plays a negligible role, and thus the velocity of a particle is proportional to the force acting on it, via $v = F/\gamma$, with γ being the friction coefficient.

For rods, the friction coefficients are different for different directions, due to the asymmetrical shape. The coefficients are given by $\gamma_{\parallel} = \gamma_0 L_{\mathrm{rod}}$, $\gamma_{\perp} = 2\gamma_{\parallel}$, and $\gamma_r = \gamma_{\parallel} L_{\mathrm{rod}}^2/6$, in parallel, perpendicular, and rotational directions respectively [66]. Here, L_{rod} is the rod length and γ_0 is a proportionality constant.

We model the noise by random forces that we apply to the rod at each time-step of the simulation. The components of the random forces are $\xi_{\parallel}$, $\xi_{\perp}$, and ξ_r for the forces in parallel and perpendicular direction and for the torque, respectively. In biological and synthetic self-propelled systems, the noise mostly arises from the environment, for example, from the density fluctuations of signaling molecules for chemotactic swimmers or from motor activity. However, we assume in our generic model that the noise has characteristics similar to a thermal noise with effective temperature T. Therefore, we draw the random forces from Gaussian distributions with variances $\sigma_{\mathrm{rod}}^2 L_{\mathrm{rod}}$, $2\sigma_{\mathrm{rod}}^2 L_{\mathrm{rod}}$, and $\sigma_{\mathrm{rod}}^2 L_{\mathrm{rod}}^3/12$, respectively. To maintain the fluctuation-dissipation theorem in three dimensions, we calculate the variances using $\sigma_{\mathrm{rod}}^2 = 2k_{\mathrm{B}}T/\gamma_0 \Delta t$, where Δt is the time step of our simulations. Note that in the case of non-thermal noise, the noise is not proportional to $k_{\mathrm{B}}T$ and also the coupling between translational and rotational noise may be different.

2.3.3 Rod-rod interaction force

The terms $\mathbf{F}_{ij}$ and M_{ij} in Eqs. (2.4)–(2.6) are the forces and the torque that is exerted from rod j to rod i. To calculate energy, force, and torque due to rod-rod interactions, we discretize each rod into n_b beads, separated from each other by a distance of L_{rod}/n_b; see Fig. 2.1. Beads from different rods interact via a potential $\Phi(r)$, where r is the distance between the centers of the two beads. The overall interaction of two rods is the sum over the interactions of all their constituent

beads,

$$\Phi^{\text{tot}} = \sum_{i=1}^{n_b} \sum_{j=1}^{n_b} \Phi(r_{ij})\,. \tag{2.7}$$

The distance between the beads L_{rod}/n_b determines the smoothness of the potential profile along the rod axis. To model the steric interaction between rods, $\Phi(r)$ should be a repulsive potential. Different choices for the potential $\Phi(r)$ lead to different collective behavior for self-propelled rods. We will discuss the effect of different interaction potentials in Secs. 2.4 and 2.5.

Hydrodynamic interactions between the rods are largely screened because of the nearby wall and the high rod density [57, 69–72], and hence are neglected in our simulations.

2.4 Soft vs hard repulsive interactions

The nature and the strength of the interaction potential between rods, Eq. (2.7) has an important effect on the collective behavior of self-propelled rods. Here we compare two different choices for the repulsive interaction between self-propelled rods. First, we examine the case where rods interact segment-wise via the repulsive part of the Lennard-Jones interaction potential. Second, we focus on the case where the interaction comes from a softer Yukawa potential. Figure 2.2 shows two snapshots of the simulation of self-propelled rods with Lennard-Jones and Yukawa potentials. Later in Sec. 2.5, we discuss the third interaction potential, the separation-shifted Lennard-Jones potential (SSLJ), that we employ in the remainder of this thesis.

2.4.1 Lennard-Jones potential

The truncated Lennard-Jones (LJ) potential [73] is

$$\Phi_{\text{LJ}}(r) = \begin{cases} 4\epsilon\left[\left(\frac{\sigma}{r}\right)^{12} - \left(\frac{\sigma}{r}\right)^{6}\right] + \epsilon, & r < 2^{1/6}\sigma \\ 0, & r \geq 2^{1/6}\sigma \end{cases}, \tag{2.8}$$

which is also known as WCA potential [74] in its truncated form. Here σ is the length scale for the interaction range, and ϵ is an energy scale characterizing the height (and depth, in the case of the original LJ) of the potential. A representative plot of the Lennard-Jones potential is shown in Fig. 2.3. This potential is typically used for modeling short range repulsions. Due to its steep slope at small distances, it is also used as an approximation for hard-sphere interactions, since implementing the latter is difficult in computer models due to its discontinuous nature. In our simulation, we use $n_b = 11$, $\sigma = 2^{-7/6} L_{\text{rod}}/n_b$, and $\epsilon = 1.21\, k_{\text{B}}T$, where L_{rod} and $k_{\text{B}}T$ are units of length and energy, respectively.

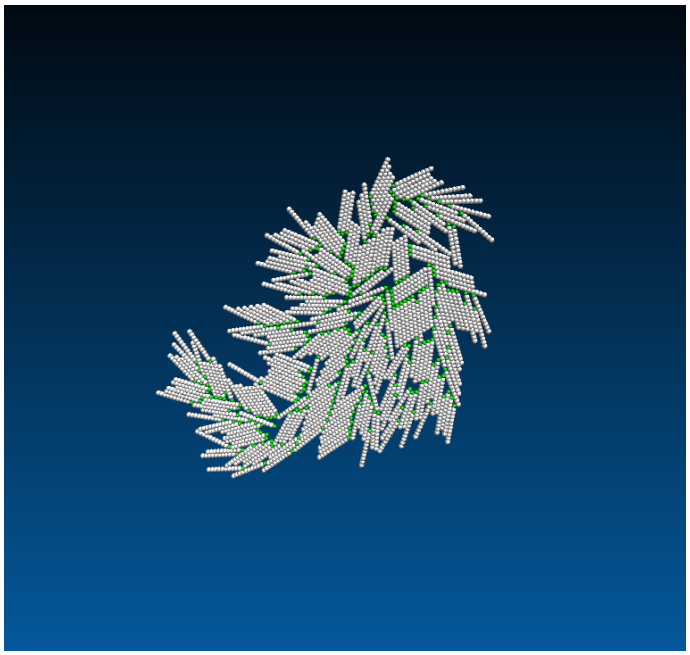

(a) Lennard-Jones potential

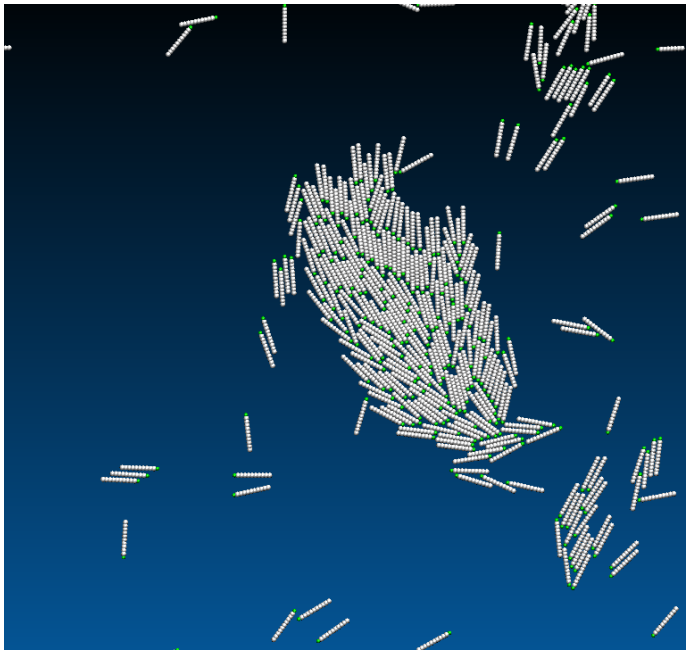

(b) Yukawa potential

Figure 2.2: Cluster formation in soft vs hard interaction potentials. Cluster of rods that interact segment-wise via (a) the Lennard-Jones potential [Eq. (2.8)], (b) the Yukawa potential [Eq. (2.9)].

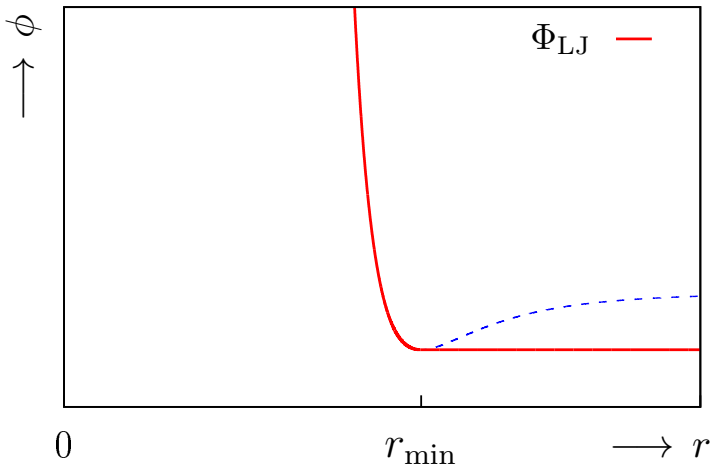

Figure 2.3: The Lennard-Jones potential, Eq. (2.8).

A snapshot of the simulation of self-propelled rods that interact with the Lennard-Jones potential is shown in Fig. 2.2(a). It shows a giant jammed cluster of rods, where no other rods have remained outside the cluster. This phase for self-propelled rods has been previously reported in Ref. [34]. The formation of this jammed cluster is due to the very non-smooth potential along the borders of the rods. When two rods collide, the tip of the colliding rod is trapped between the two beads from the other rod. As a result, the colliding rod cannot slide along the other rod to move forward.

2.4.2 Yukawa potential

The truncated Yukawa potential is

$$\Phi_{\mathrm{Yuk}}(r) = \begin{cases} A\frac{e^{-Br}}{r} - \Phi_0, & r < r_{\mathrm{min}} \\ 0, & r \geq r_{\mathrm{min}} \end{cases}, \tag{2.9}$$

where the constant A characterizes the strength and $1/B$ characterizes the range of the potential. The potential is shifted by a constant $\Phi_0 = Ae^{-Br_{\mathrm{min}}}/r_{\mathrm{min}}$ to avoid a discontinuity at $r = r_{\mathrm{min}}$. A representative plot of the Yukawa potential is shown in Fig. 2.4. We use $n_b = 11$, $A = 2.0 \times 10^6\, L_{\mathrm{rod}} k_{\mathrm{B}} T$, $B = 1.5\, L_{\mathrm{rod}}$, and $r_{\mathrm{min}} = 0.18 L_{\mathrm{rod}}$ in our simulation.

A snapshot of the simulation of self-propelled rods that interact with the Yukawa potential is shown in Fig. 2.2(b). It shows a giant cluster composed of many rods. However, the cluster has a clear polarity, and not all rods in the system are trapped in the cluster. The cluster is dynamic, and rods constantly join/leave the cluster in the steady state. The observed difference between the

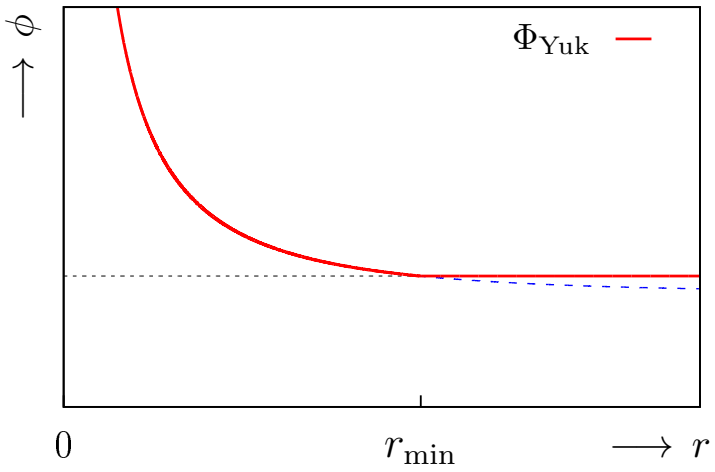

Figure 2.4: The Yukawa potential, Eq. (2.9).

clusters in Figs. 2.2(a) and 2.2(b) are due to the fact that the Yukawa potential is "softer," meaning that the potential of a bead grows more slowly as the distance to the bead is decreased, compared to the case for the Lennard-Jones potential. Therefore, two colliding rods do not interlock, and can more easily slide along each other and align.

2.5 The separation-shifted Lennard-Jones potential

Both the Lennard-Jones and the Yukawa potential (introduced in Secs. 2.4.1 and 2.4.2, respectively) model a form of steric interaction between rods. In both cases, the potential diverges at small distances between the beads [Eqs. (2.8) and (2.9)] which leads to an infinite repulsive force if the rods cross each other. Therefore, none of these potentials allows crossing events. As stated in Sec. 2.1, one of our motivations for modeling self-propelled rods is to study the behavior of systems such as motility assays and gliding bacteria on substrates. We would like to have crossing events in our two-dimensional simulations as a means to simulate the experimental events where one rod-like swimmer is temporarily pushed to the bulk to pass over the other swimmer; see Sec. 2.7. To model crossing events, we need an interaction potential that does not diverge at $r \approx 0$, yet still has a repulsive nature. To this end, we use a separation-shifted Lennard-Jones (SSLJ) potential [75].

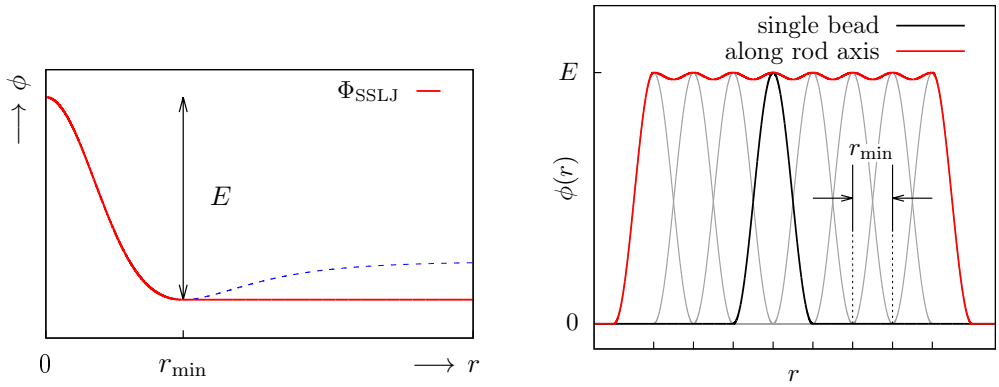

Figure 2.5: Left: plot of the SSLJ potential, Eq. (2.10). Right: potential profile of a rod, with SSLJ potential for its bead, along its long axis. Tics on the horizontal axis show the position of beads, separated from each other by r_{min}. In our simulations, we use $n_b = 18$.

Using the SSLJ potential, beads from different rods interact via

$$\Phi_{\mathrm{SSLJ}}(r) = \begin{cases} 4\epsilon\left[(\alpha^2 + r^2)^{-6} - (\alpha^2 + r^2)^{-3}\right] + \Phi_0, & r < r_{\mathrm{min}} \\ 0, & r \geq r_{\mathrm{min}}\,, \end{cases} \tag{2.10}$$

where r is the distance between two beads and ϵ gives the interaction energy. The potential is shifted by Φ_0 to avoid a discontinuity at $r = r_{\mathrm{min}}$. The parameter α characterizes the capping of the potential. For $\alpha \neq 0$, Φ does not diverge at $r = 0$, hence allowing bead-bead overlap; for $\alpha = 0$, $\Phi(r)$ becomes the truncated Lennard-Jones potential, Eq. (2.8). A representative plot of the SSLJ potential is shown in Fig. 2.5, together with the potential profile of a rod along its long axis.

$E = \Phi(0) - \Phi(r_{\mathrm{min}})$ is the energy for two beads that completely overlap and is used as independent parameter in our simulations. Setting E to any value will dictate $\epsilon = \alpha^{12}E/(\alpha^{12} - 4\alpha^6 + 4)$. The constant $\alpha = (2^{1/3} - r_{\mathrm{min}}^2)^{1/2}$ is calculated by forcing $\Phi(r)$ to be zero at $r = r_{\mathrm{min}}$. Considering the weak repulsion between rods, we define $r = r_{\mathrm{min}}/2$ as the effective radius for each bead, which results in the effective rod thickness r_{min} and the rod aspect ratio $L_{\mathrm{rod}}/r_{\mathrm{min}}$. The number of beads n_b used for discretization is chosen such that the rod has a relatively smooth potential profile, so that no interlocking occurs when rods slide along each other; see Fig. 2.5 (right). This means that the potential of each bead considerably overlaps with that of its neighboring beads.

2.6 Simulation parameters

We present the main results of the simulations using our model in Chapter 4. The numerical parameters used in the simulations are as follows. We study systems with approximately 10 000 rods at scaled number densities ranging from $\rho\, L_{\mathrm{rod}}^2 = 2.5$ to 10, where the number density of rods is defined as $\rho = N_{\mathrm{rod}}/L_x L_y$. We measure lengths in units of rod length L_{rod}, energies in units of $k_{\mathrm{B}}T$, and times in units of the orientational diffusion time for a single rod, $\tau_0 = 1/D_r = \gamma_0 L_{\mathrm{rod}}^3/6\, k_{\mathrm{B}}T$. The system size is $L_x = L_y = 36\, L_{\mathrm{rod}}$, the cutoff $r_{\mathrm{min}} = L_{\mathrm{rod}}/n_b = 0.056\, L_{\mathrm{rod}}$, the number of beads used for each rod $n_b = 18$, the rod aspect ratio $L_{\mathrm{rod}}/r_{\mathrm{min}} = 18$, the time interval $\Delta t = 1.65 \times 10^{-4}\, \tau_0$, and unless mentioned otherwise, $E = 1.5\, k_{\mathrm{B}}T$.

There are three different energy scales in our system; the thermal energy $k_{\mathrm{B}}T$, the propulsion strength $F_{\mathrm{rod}} L_{\mathrm{rod}}$, and the energy barrier E. Therefore, there are two dimensionless ratios that characterize the importance of the different contributions: the Péclet number, defined as

$$\mathrm{Pe} = \frac{L_{\mathrm{rod}} v_0}{D_{\parallel}} = \frac{L_{\mathrm{rod}} F_{\mathrm{rod}}}{k_{\mathrm{B}}T}\,, \tag{2.11}$$

which is the ratio of propulsion strength to noise,[2] and the *penetrability* coefficient, Q, defined as

$$Q = \frac{L_{\mathrm{rod}} F_{\mathrm{rod}}}{E}\,, \tag{2.12}$$

which is the ratio of propulsion strength to energy barrier. $D_{\parallel} = k_{\mathrm{B}}T/\gamma_{\parallel}$ is the diffusion coefficient parallel to the rod orientation.

We simulate rods with Péclet (Pe) numbers in the range $0 \leq \mathrm{Pe} < 200$ and penetrabilities in the range $0 \leq Q < 200$. We change Pe by changing F_{rod} for fixed σ_{rod}^2 and Δt, i.e., for fixed temperature. We change Q by changing both F_{rod} and E.

2.7 Crossing probability for rod-rod collisions

With the introduction of the SSLJ potential in Sec. 2.5, it is interesting to know if our two dimensional simulations using the SSLJ potential can reproduce results that are consistent with experimental data from filament assays [22,23]. One can directly measure if the rod-like swimmers cross each other in the experiments and compare the probability of crossing events $P(\phi)$ to the simulations as a function of the angle ϕ by which two rods collide each other.

To find the probability of crossing events $P(\phi)$, we performed simulations for two rods that initially touch each other in a tip-center arrangement with crossing

[2] The Péclet number can be alternatively defined as $\mathrm{Pe}_r = v_0/D_r L_{\mathrm{rod}}$ with the rotational diffusion constant D_r. In such case, $\mathrm{Pe} = 6\,\mathrm{Pe}_r$.

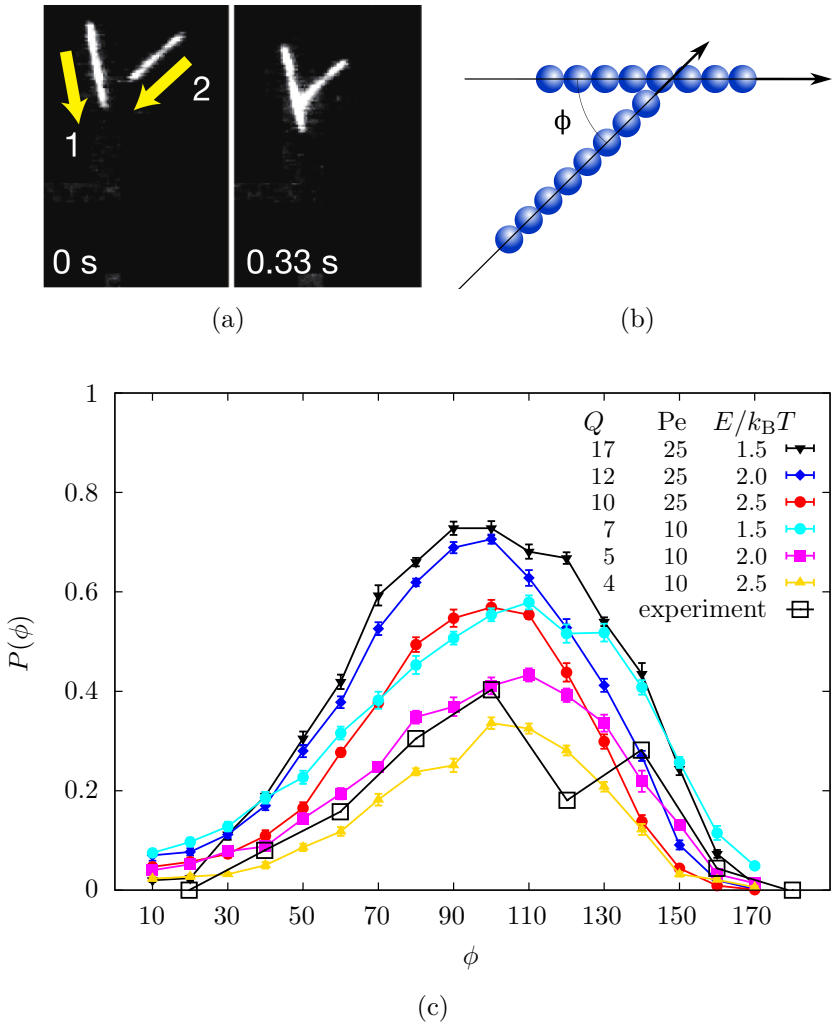

Figure 2.6: Crossing probability for two rods as a function of their crossing angle ϕ (as defined in the schematic). For each angle, 1000 simulations have been performed. The simulations are divided into 10 groups and the error bars are calculated as the standard deviation of the mean (σ_m) for these groups. Figure (a) as well as the experimental data are taken from Ref. [23].

angle ϕ; see Fig. 2.6. We measure $P(\phi)$ for several penetrabilities and Péclet numbers using the SSLJ interaction potential, Eq. (2.10). We count a crossing event when two rods intersect significantly, i.e., such that the intersection point is at least $0.2L_{\mathrm{rod}}$ away from the ends of each rod. We thus do not count events when one rod only "touches" the other rod, which frequently happens due to the weak repulsion between the rods.

As shown in Fig. 2.6, $P(\phi)$ is low near $\phi \simeq 0°$ and $\phi \simeq 180°$ and has a peak near $\phi \simeq 90°$. There is a small asymmetry in the peak with an enhancement for directions $\phi > 90°$, which may be attributed to the increased relative velocity between two rods for $\phi > 90°$ and the fact that the rods are not perfectly smooth. Comparison between $P(\phi)$ for different penetrabilities shows that an increased Q generally increases the probability for rod crossing. In addition, for small Pe, noise also plays an important role to enhance rod crossing. For example, the curves for $Q = 10$ and $Q = 7$ in Fig. 2.6 have approximately the same height, which could be explained by the fact that the effect of noise is higher for the case $Q = 7$ that has a smaller Pe.

The results are qualitatively similar to the crossing probability measured in experiments with microtubules propelled on surfaces. In Fig. 3(d) in Ref. [23], the maximum crossing probability for two microtubules in a motility assay is 40 % and corresponds to $Q = 5$ and $\mathrm{Pe} = 10$ in our simulations. However, the same crossing probability may be achieved by reducing Q and increasing Pe at the same time.

Chapter 3

Isotropic-nematic transition for passive suspension

Before studying the collective behavior of active (swimming) rods that are propelled by converting a form of energy to mechanical work, it is worthwhile to study the behavior of rods in an equilibrium phase, i.e., in the state where self-propulsion is absent. Such passive rod systems are influenced only by thermal noise and rod-rod repulsive interactions, as described in Sections 2.3.2 and 2.3.3.

Suspensions of passive rods exhibit different degrees of positional and orientational order, namely isotropic, nematic, columnar, smectic, and crystalline. At low and intermediate densities, transition from an isotropic phase to a nematic phase occurs. While in the isotropic phase rods are randomly oriented in all directions, the nematic phase is an anisotropic fluid in which rods are oriented in loose parallel lines.

In this chapter, we perform Brownian dynamics and Monte-Carlo simulations to study the isotropic-nematic transition of rods. As we shall see in the remainder of this chapter, this transition happens with increasing density of rods. However, in our penetrable rod model not only the density of rods controls the transition, but also the energy barrier for rod crossing plays an important role. Therefore, we systematically study the effect of *both* the density of rods and the energy barrier by performing extensive Monte-Carlo simulations. At the end of this chapter, we generalize the Onsager theory—which analytically predicts the isotropic-nematic transition for *impenetrable* rods [59]—to the case of penetrable rods. We show very good agreement between the generalized theory and our Monte Carlo simulations.

3.1 Background

It was reported by Zocher (1925) [76] that solutions of rod-like particles phase separate into coexisting isotropic and anisotropic phases when the density of the

particles is higher than a threshold value. Onsager (1949) [59] explained this phenomenon, arguing that the alignment of rod-like particles is a result of the competition between orientational entropy and the positional entropy associated with the excluded volume interaction: At low densities, entropy is maximized by random orientation of rods. However, alignment of rods becomes more favorable at high densities, since the rods gain more free space (positional entropy), which is otherwise blocked by the excluded volume interaction. Oster (1950) subsequently observed the isotropic-nematic transition of rod-like tobacco mosaic viruses [77] and found it to be in qualitative agreement with the Onsager theory. Since then, numerous experimental studies have confirmed the transition from the isotropic to the nematic state [78–86].

Since suspensions of passive rods are in thermodynamic equilibrium, the behavior of such systems can be studied using standard techniques in statistical mechanics. These techniques span a wide range of theoretical as well as numerical methods, including different methods for minimization of the free energy, and Monte-Carlo simulations [87–92].

Onsager theory [59] assumes that the rods are infinitesimally thin, i.e., the aspect ratio of the rods L/d is much larger than 1, where L is the rod length and d is the rod diameter. In this regime, the critical density for isotropic-nematic transition has been found to be $\rho_c L_{\mathrm{rod}}^3 = 4$ in three spatial dimensions [93]. For finite aspect ratios, one finds a higher critical density, as described for example in Ref. [88].

In two dimensions, it has been calculated that the isotropic-nematic transition of long needles occurs at a critical density of [93]

$$\rho_c = \frac{3\pi}{2L^2}\,. \tag{3.1}$$

It should be stressed that these results in 2D and 3D are calculated for the case of long rods with strict excluded volume interactions, i.e., for the case where the rods cannot cross each other. In our penetrable rod model, this corresponds to the regime of long rod length L_{rod} (and consequently large number of beads n_b) and infinite energy barrier $E \to \infty$. For systems with a finite energy barrier given by Eq. (2.10), not only the density of rods but also the energy barrier E affects the isotropic-nematic transition. As E becomes smaller, the tendency for rods to align becomes weaker because overlaps occur more frequently. As a result, the isotropic-nematic transition shifts to higher densities. For $E = 0$, the rods do not interact mutually and thus are in the isotropic phase for all densities.

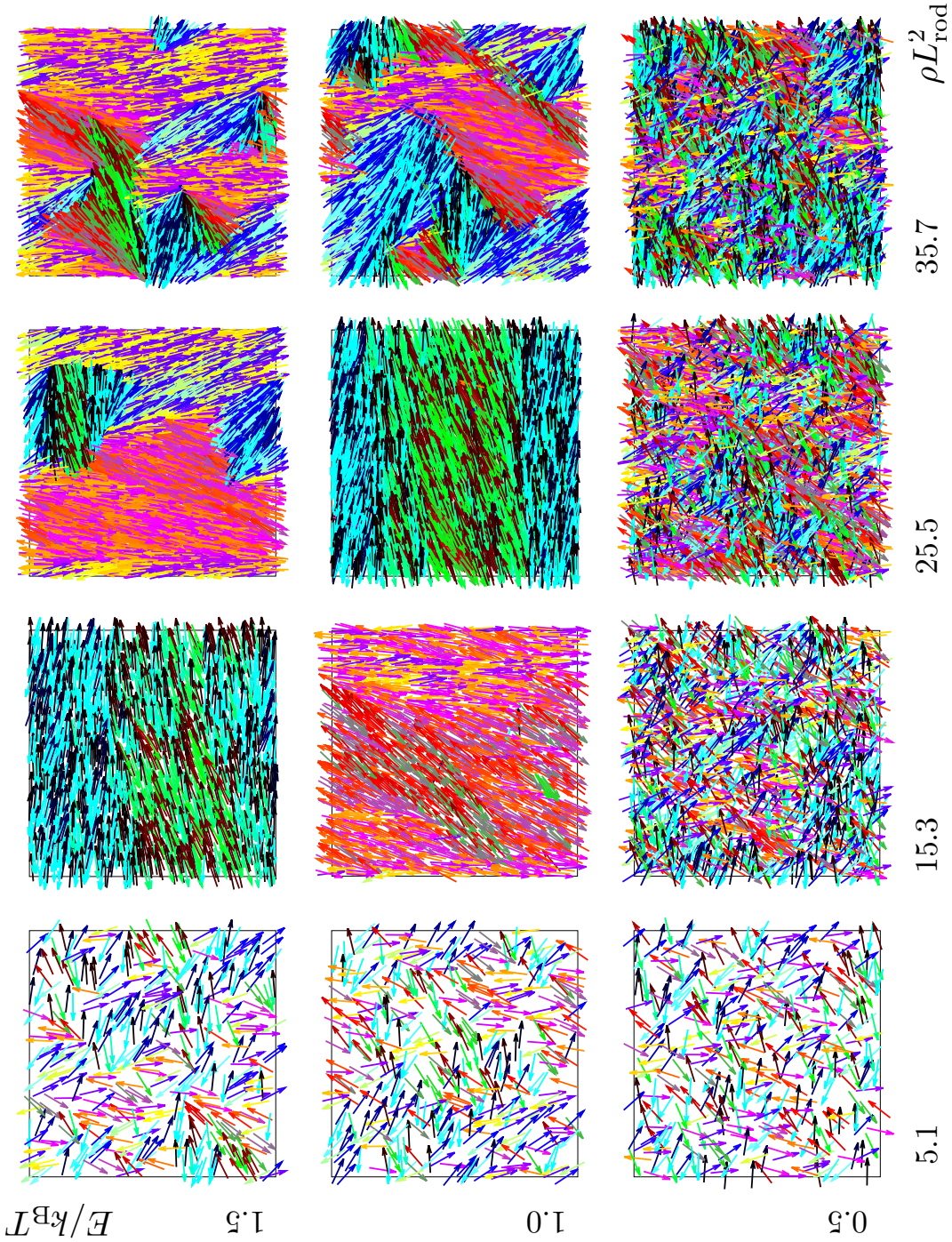

Figure 3.1: Snapshots of Brownian dynamics simulations of passive rods in two dimensions, for various scaled densities ρL^2_{rod} and energy barriers E. Bottom-left: isotropic phase. Top-right: interlocked metastable nematic domains; see Sec. 3.2

3.2 Brownian dynamics simulation of passive rods

Although we perform the systematic study of passive rods using Monte-Carlo simulations, we have performed a limited number of simulations using Brownian dynamics for passive rods. Figure 3.1 shows snapshots of such systems with various scaled densities ρ and energy barriers E, and a small system size of $9L_{\mathrm{rod}}$. Starting from random position and orientation for all rods, we observe an isotropic phase at low ρ and E. For high densities and energy barriers, we observe interlocked regions with high nematic order. The nematic domains in such systems are metastable and do not coalesce or disappear in the time scale of our simulation. However, since such simulations require a long time to reach true equilibrium, we do not pursue this method in the remainder of this chapter.

3.3 The Monte-Carlo method

Here we briefly explain the Monte-Carlo method as it is used in our simulations. For a more comprehensive review on Monte-Carlo method, the reader can refer to standard books on computational physics, e.g. Ref. [94].

3.3.1 Basics of Monte-Carlo simulations

We use Metropolis–Hastings algorithm [95,96], which is one of the several classes of Monte-Carlo (MC) simulations. The Metropolis–Hastings algorithm is based on probing the phase space and minimization of the free energy. Unlike molecular dynamics (MD) or Brownian dynamics (BD) simulations, MC simulations do not track the position of the particles over time. Instead, in each step of the MC algorithm, we propose a new state for the system by committing a random change in its current configuration (details will be explained shortly). The difference in the total energy of the system upon moving to the new configuration is used to decide whether we accept or reject the new state.

Let us denote the energy of the system in the current state and in the proposed state by E and E', respectively. We accept the new proposed state with the probability

$$P_{E\to E'} = \begin{cases} 1, & E' < E \\ \exp[-(E' - E')/k_{\mathrm{B}}T], & E' \geq E\,, \end{cases} \tag{3.2}$$

where T is the temperature of the system and k_{B} is the Boltzmann constant. This means that we always accept new states if their associated energy is lower than the energy of the current state. Otherwise, we accept the new states only with a probability that is smaller for low temperatures and higher for high temperatures. If the new configuration is accepted, we proceed to the next Monte-Carlo step

by proposing the next random configuration based on the newly accepted one. Otherwise, we dismiss the proposed state and try with a new random state. Successive application of the Monte-Carlo steps results in an energy distribution consistent with the canonical ensemble for a system with temperature T.

The validity of the MC method depends on whether the ergodic hypothesis is met, i.e., whether the generated configurations span the entire phase space accessible to the system. This requires a proper choice of parameters for generating random configurations. Fulfilling the ergodic hypothesis is essential, because we would like that the MC simulation gives rise to an ensemble average after a sufficient number of MC steps. Otherwise, the system might spend most of the time in a local energy minimum, being unable to sufficiently probe the rest of the phase space.

3.3.2 Generating random configurations

In each step of our simulation, we generate a new configuration by randomly changing the position and the orientation of a randomly selected rod. We change the position of the rod parallel and perpendicular to the rod axis by a random number which is drawn from a normal (Gaussian) distribution with spread $\sigma_{\parallel}$ and $\sigma_{\perp}$, respectively. We also change the orientation of the rod by an angle, which is drawn from a normal distribution with spread σ_{θ}.

Taking very small values for displacements of the rod in each step causes successive configurations of the system to be strongly correlated, and leads to high computational costs. However, selecting too large displacements would prevent rods to fine-tune their equilibrium position, and therefore leads to a fast-evolving system that requires a very long time to reach an equilibrium state. We find the following values for the displacements to be suitable for our Monte-Carlo simulations in parallel, perpendicular, and angular coordinates, respectively: $\sigma_{\parallel}/L_{\mathrm{rod}} = 0.056$, $\sigma_{\perp}/L_{\mathrm{rod}} = 0.0056$, and $\sigma_{\theta}/2\pi = 0.01$.[1]

3.3.3 Parallelization techniques

To boost efficiency of the simulation, we use parallelization in the following way: We divide the simulation box into smaller cells, with linear dimension of $L_{\mathrm{rod}} + r_{\mathrm{min}}$. In the course of the simulation, the calculation of each cell is taken over by one CPU core. The energies are calculated based on the interaction of the rod in each cell with the rods in all surrounding 8 cells. We simultaneously displace one rod in each cell and calculate the acception/rejection criterion independently for that cell. In this way, we can perform n_{cell} steps simultaneously, where n_{cell}

[1] Note that the σ_{θ} value mentioned here is only applicable to simulations with continuous rod orientations, as shall be explained in Sections. 3.4.2 and 3.5. For discrete angular states discussed in Sec. 3.4.1, we choose larger σ_{θ} values that allow for the first few neighboring orientations.

is the number of cells. However, there can be a case where two displaced rods from neighboring cells interact. In this case, the calculation of energies might be wrong depending whether one or both of the displacements are accepted. To prevent this scenario, we only parallelize cells with the same checkboard color, i.e. we displaced rods in all white (black) cells at a time. Therefore, we end up doing $n_{\text{cell}}/2$ steps in parallel. There is still the very improbable possibility that the rods from two diagonally-connected cells interact, and cause a similar problem. We neglect this possibility.

3.4 Isotropic initialization of rods

In the Monte-Carlo simulation of penetrable rods, there are two possibilities regarding the initialization of the system. Whether we start from a perfectly nematic state and wait until the low density systems relax to isotropic phase, or we start from an isotropic phase, and wait until the high density systems develop nematic order. We present results from both approaches in this and the following section.

Starting from a random isotropic configuration, we find that the system is stuck in that phase, and never develops nematic domains. This is because the alignment of rods that is needed for nematic order requires high synchronization between rod orientations. This is particularly crucial for the rods in our systems with relatively large aspect ratio of $a = 18$, where a very small change in the orientation of two neighboring parallel rods would change the interaction energy from zero to several E's. Therefore, we think the inability to reach nematic order starting from random orientation of rods is because the rods cannot collectively adjust their orientations to the very tiny orientation range of their neighbors, required for energy minimization.

3.4.1 Discrete angular states

To solve the aforementioned problem, we guide the system to "find" the right orientations by discretizing the available orientations for each rod. We run Monte-Carlo simulations where the angular degree of freedom for rods is limited to a finite number of angles, n_s, see Fig. 3.2. In this way, there is no need to fine-tune the orientations, since the orientations for different rods are either exactly equal, or differ significantly. While the rods' positions are randomly initialized over the continuous values of x and y, the orientations are initialized randomly only between the available angular states.

Figure 3.3 shows snapshots of high-density systems with different numbers of states n_s from 10 to 160, and a very high energy barrier $E = 250\,k_{\text{B}}T$. As can be seen in the snapshots, only the systems with lower number of angular state $n_s = 10$ and $n_s = 20$ have formed nematic domains, while systems with $n_s \geq 30$

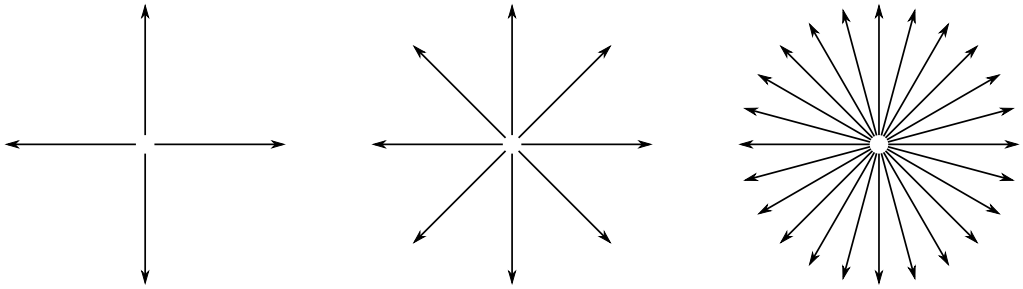

(a) $n_s = 4$ (b) $n_s = 8$ (c) $n_s = 24$

Figure 3.2: In Monte-Carlo simulations with a finite number of angular states n_s, rods can only take a limited number of orientation angles. Examples for $n_s = 4$, $n_s = 8$, and $n_s = 24$ are shown here.

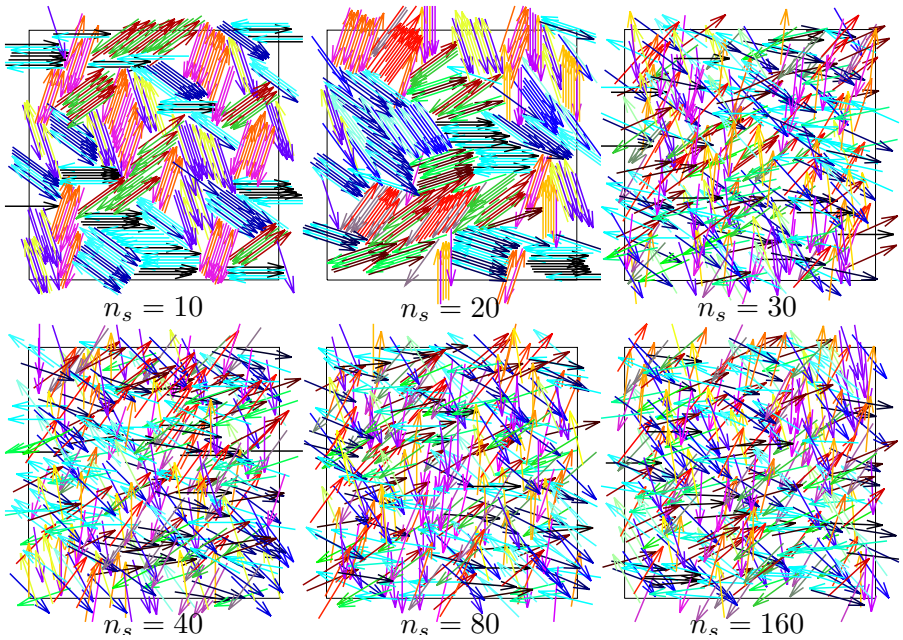

Figure 3.3: Snapshots of Monte-Carlo simulations for different (high) number of angular states n_s, initialized from random configuration. Density is $\rho L^2 = 18$ and energy barrier is $E = 250\, k_\mathrm{B}T$.

remain isotropic.

We also studied the effect of different distribution of random numbers used for displacements of rods. Figure 3.4 shows snapshots for systems with different number of states $n_s = 4, 6, 12, 24$ and two random number generators (RNGs): uniform and Gaussian. All systems have relatively high energy barrier $E = 7.5\, k_{\mathrm{B}}T$. We observe the same trend with increasing n_s. The change in RNG does not significantly change the results. However, we observe some small nematic domains for $n_s = 12$ in the system with uniform RNG, while the corresponding system with Gaussian RNG is more isotropic.

Since we observe nematic domains mostly for $n_s \leq 20$, we focus on the cases where $n_s = 10$ and $n_s = 20$, and we run extensive Monte-Carlo simulation to systematically study the effect of rod density ρ and crossing energy barrier E on the isotropic-nematic transition. Figures 3.5 and 3.6 show snapshots of systems with different densities and energy barriers for the case of $n_s = 10$ and $n_s = 20$, respectively. In both cases, the nematic domain formation is observed in the top-right of the snapshot matrix, i.e. for high densities and energy barriers. We also observe that the nematic domain formation is more pronounced for $n_s = 10$ than for $n_s = 20$. This is also consistent with the behavior of the systems presented in Figs. 3.3 and 3.4.

3.4.2 Effect of the external field

Since the nematic order observed in Sec. 3.4.1 depends on our choice for the number of angular states n_s, we try to find other techniques to reach nematic order that do not introduce a new free parameter.

One possibility is to introduce an external field E^{ext} that pushes all rods to align in a prescribed direction. We expect that with such a field, the critical density ρ^*_{ext} for the isotropic-nematic transition shifts to lower values. By changing the strength of the external field E^{ext}, we measure the dependence of ρ^*_{ext} on E^{ext}, and extrapolate to the case where $E^{\mathrm{ext}} = 0$. In this way, we can characterize the isotropic-nematic transition without introducing any new parameter.

To this end, we studied the response of the system to an external field that aligns the rods along the x (horizontal) direction. We define the total energy of a rod in the presence of the external field to be

$$E_i^{\mathrm{ext}} = E_i - E^{\mathrm{ext}} \cos(2\,\theta_i)\,, \tag{3.3}$$

where E_i^{ext} is the total energy, E_i is the energy only due to the interactions with other rods, E^{ext} is the strength of the external field, and θ is the orientation of the rod. Compared to the case with no external field, Eq. 3.3 assigns a lower energy to rods that are parallel or antiparallel to the x axis, and a higher energy to rods that are perpendicular to the x axis. Therefore, the external field favors configurations of rods in horizontal directions.

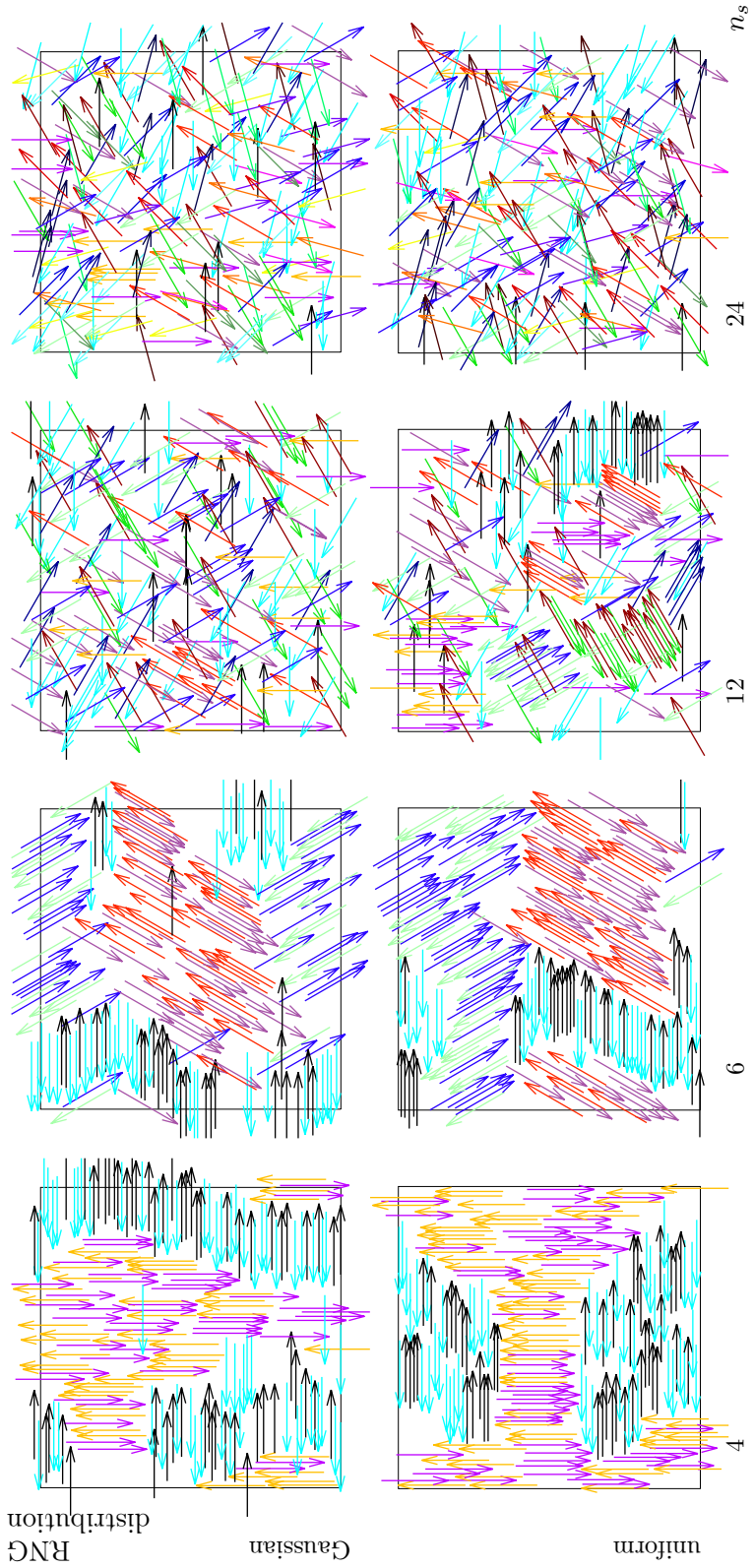

Figure 3.4: Snapshots of Monte-Carlo simulations for different number of angular states n_s, and different distributions for Monte-Carlo step lengths. Density is $\rho L^2 = 10.2$ and energy barrier $E = 7.5 k_\mathrm{B} T$.

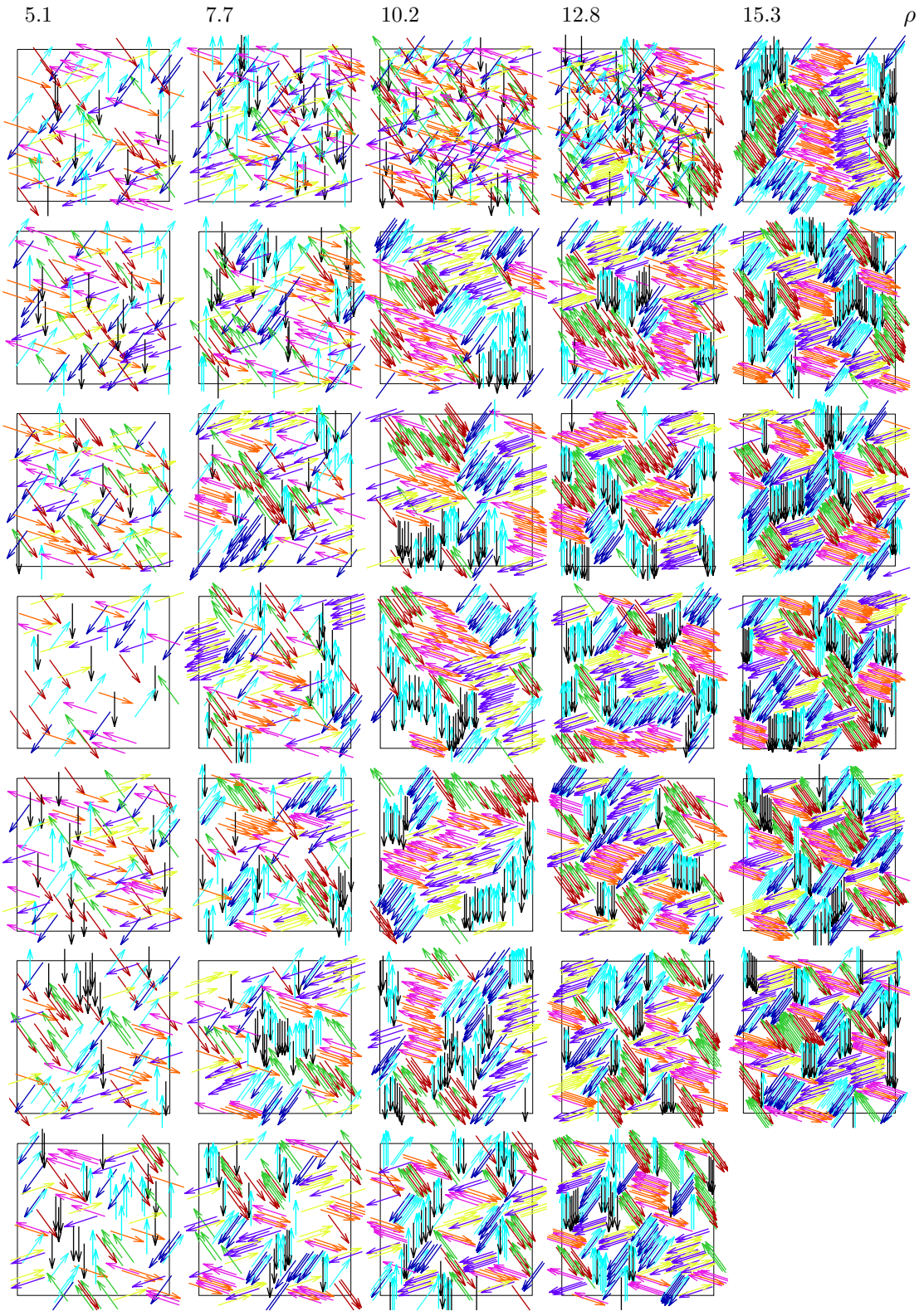

Figure 3.5: Snapshots of Monte-Carlo simulations with angular states $n_s = 10$ for various scaled densities ρ and energy barriers E; see Sec. 3.4.1.

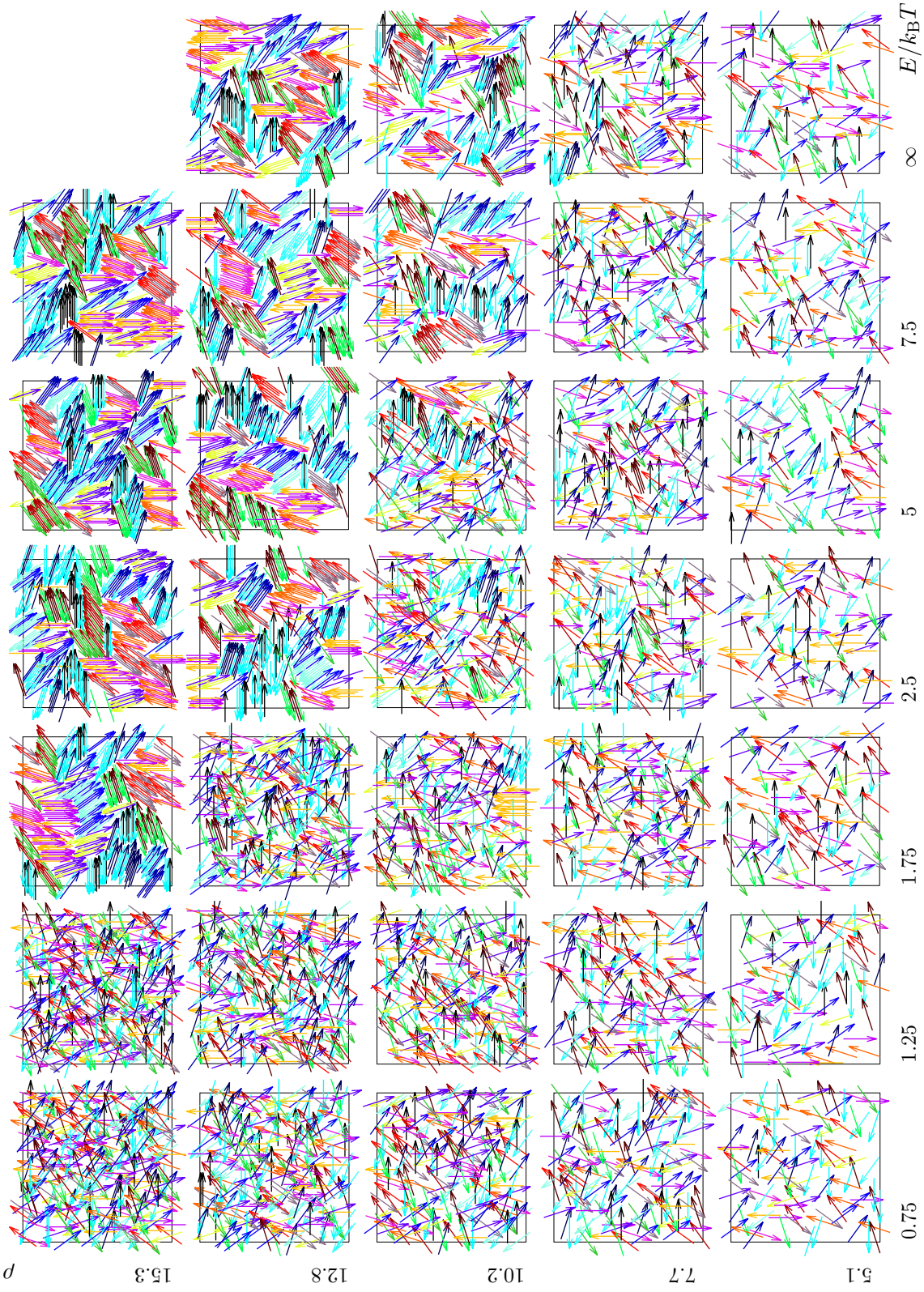

Figure 3.6: Snapshots of Monte-Carlo simulations with angular states $n_s = 20$ for various scaled densities ρ and energy barriers E; see Sec. 3.4.1.

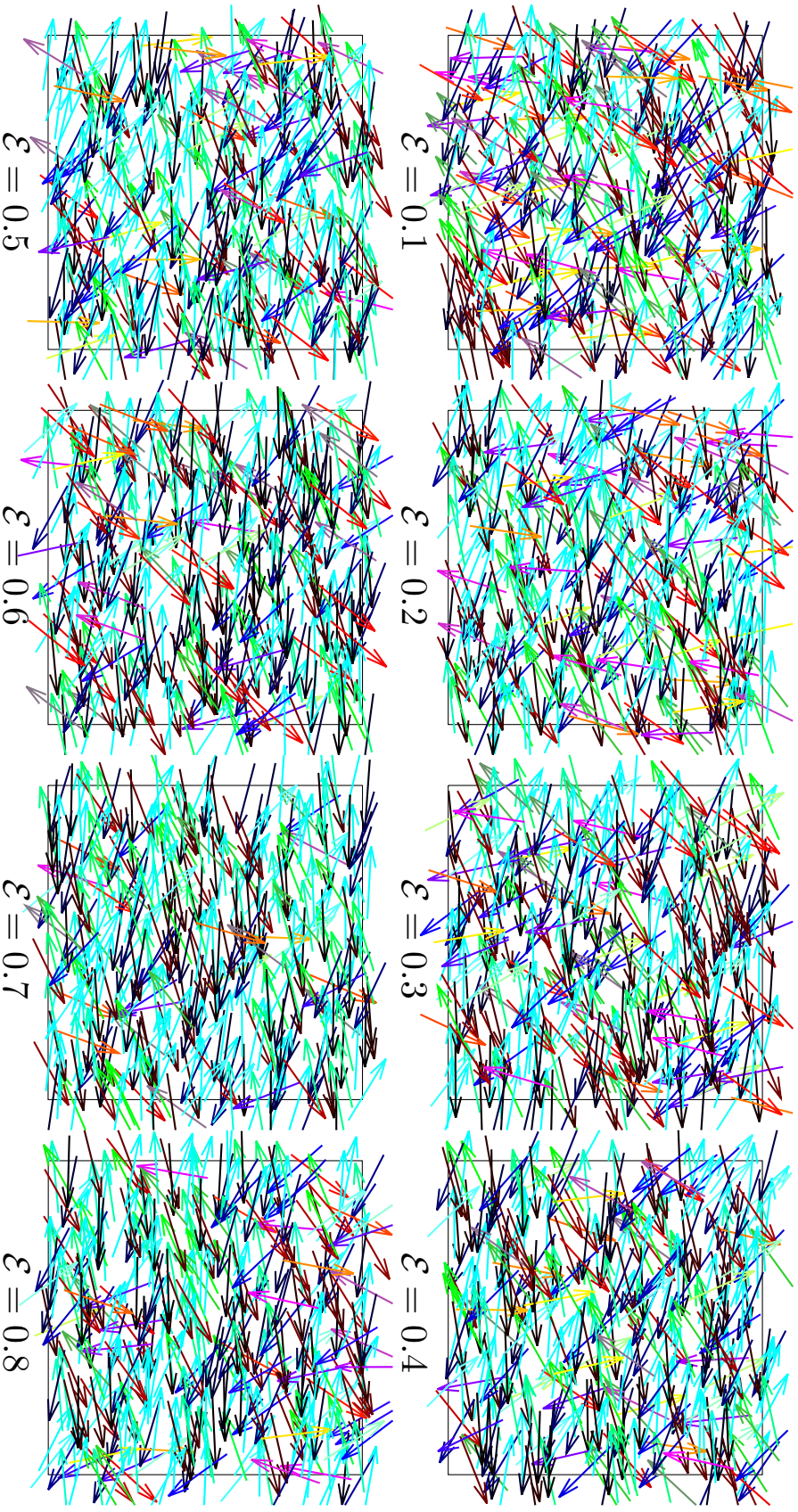

Figure 3.7: Snapshots of Monte-Carlo simulations for different strengths of the external field $\mathcal{E}$. Density is $\rho L^2 = 18$, number of angular states $n_s = \infty$ (continuous) and energy barrier $E = 7.5 k_\mathrm{B} T$; see Sec. 3.4.2.

We characterize the strength of the external field by the dimensionless parameter

$$\mathcal{E} = E^{\text{ext}}/n_b E\,, \tag{3.4}$$

where n_b is the number of beads in the rod and E is the energy of a bead that completely overlaps with another bead [Eq. (2.10)]. $\mathcal{E} = 1$ corresponds to the energy of a rod that completely overlaps with all the beads of another rod. Since we have added the external field, we no longer discretize the available angular states for the rods; thus the orientations of the rods can take any value in the continuous range of $[0, 2\,\pi)$.

Snapshots of the systems for different strength of the external field $\mathcal{E}$ are shown in Fig. 3.7. By visual inspection, we can see that the nematic order slightly increases with increasing external field. However, even with strong fields $\mathcal{E} = 0.8$ that we tried in our simulations, we do not observe regions with high nematic order, as we observed with discretized rod orientations in Sec. 3.4.1. The observed nematic order is therefore too weak for performing the extrapolation towards $\mathcal{E} \to 0$.

3.5 Nematic initialization of rods

In Sec. 3.4 we discussed the isotropic-nematic behavior of rods starting from isotropic configurations. In this section, we study the behavior of passive rods starting from a perfectly nematic state. We expect that for systems with high density and energy barrier, the nematic order is preserved in the Monte-Carlo simulations. However, we expect that for systems with low-density and low-energy-barrier, the initial nematic order is lost and isotropic behavior emerges.

Unlike the simulations in Sec. 3.4.1, we do not discretize the angular states of rods, and we allow all rod orientations in our Monte-Carlo simulations. We initialize all rods to point in $\pm y$ (vertical) direction. We systematically study the state of the system for several values of ρ and E. In Fig. 3.8 several snapshots of such systems are shown. We observe nematic state at the top-right of the snapshot matrix, i.e. for high ρ and high E, as expected. A closer look at snapshots with highest ρ and E reveals that the nematic state in such systems have fewer defects, while the nematic regions in the intermediate ρ and E regime have regions with slightly different orientations (colored in light/dark blue). In the bottom-left of the snapshot matrix, hardly any nematic region is visible, as indicated by the fine patchy coloring scheme of the snapshots.

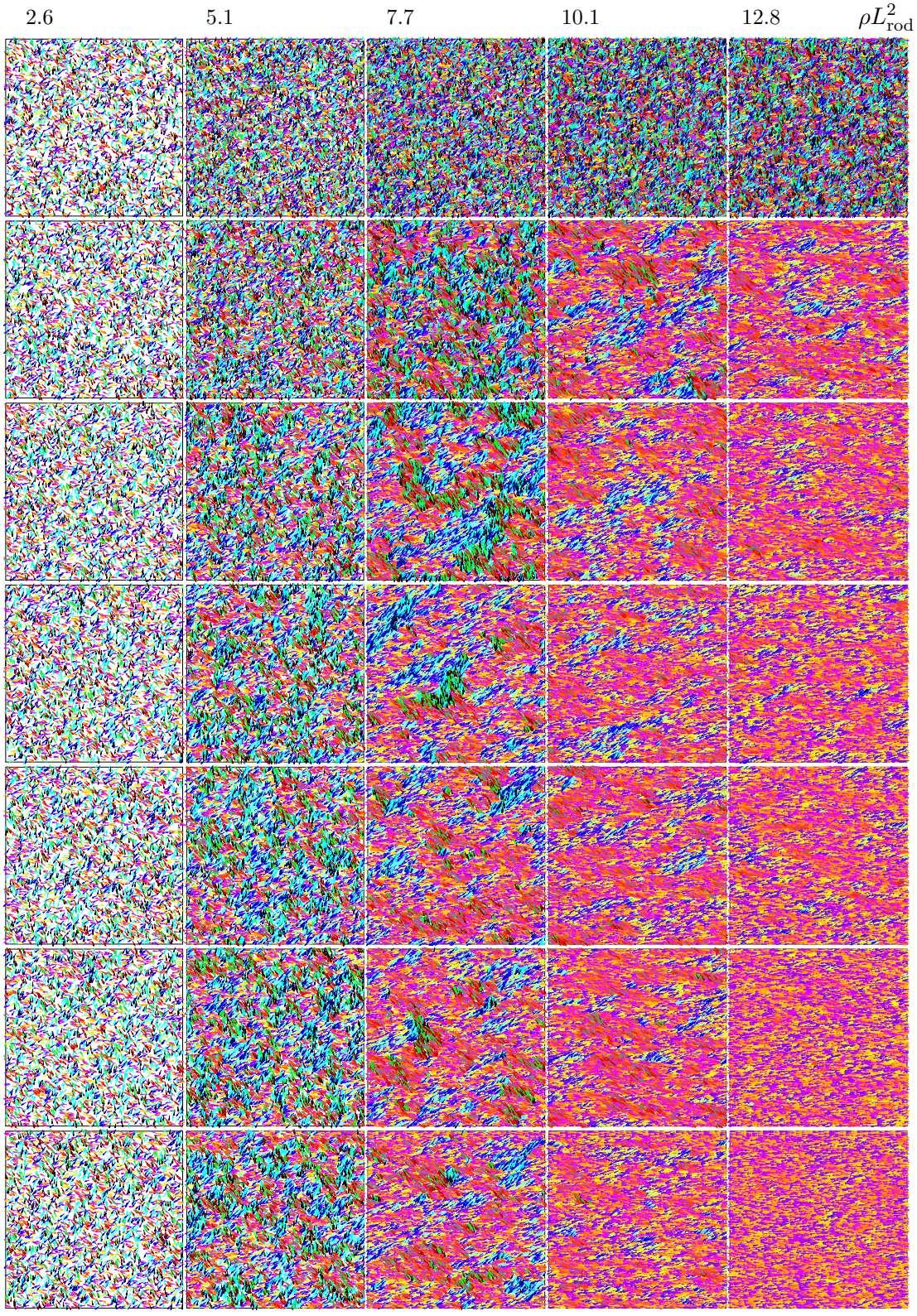

Figure 3.8: Snapshots of Monte-Carlo simulations with continuous angles, initialized in perfect nematic state, for various scaled densities ρL_{rod}^2 and energy barriers E; see Sec. 3.5 and the phase diagram in Fig 3.10.

3.5.1 Isotropic-nematic phase diagram

We characterize the nematic order in the passive rod systems using the nematic order parameter [58], defined as

$$S = \left\langle \sum_{i \neq j}^{N} \frac{1}{N(N-1)} \cos[2(\theta_i - \theta_j)] \right\rangle . \tag{3.5}$$

We divide the simulation box into smaller cells with side length $4.5\,L_{\mathrm{rod}}$, and calculate S for each cell. The order parameter defined via Eq. (3.5) does not discriminate between parallel and antiparallel configurations; see Fig. 3.9. Isotropic systems with many rods have $S = 0$, while perfectly nematic systems have $S = 1$.

Figure 3.10 shows a phase diagram of the system with varying density and energy barrier. According to analytical theory [93], for $E = \infty$ and $L_{\mathrm{rod}}/r_{\mathrm{min}} \gg 1$ the transition from the isotropic to the nematic state occurs at $\rho_c\, L_{\mathrm{rod}}^2 = 3\pi/2$, as indicated by the black arrow in Fig. 3.10. We have calculated the transition density for finite energy barriers,

$$\rho_c\, L_{\mathrm{rod}}^2 = \frac{3\pi}{2} \frac{1}{[1 - \exp(-E/k_{\mathrm{B}}T)]} , \tag{3.6}$$

by generalizing Onsager's approach for finite energy barriers, as described in Sec. 3.6. We find very good agreement between the analytical theory shown by the red line in Fig. 3.10 and our Monte Carlo simulations. The phase diagram is also consistent with our Brownian dynamics simulations for $\mathrm{Pe} = 0$ and $E = 1.5\,k_{\mathrm{B}}T$; see snapshots in Figs. 1.15(a) and 1.15(b).

The nematic order parameter is plotted in Fig. 3.11 for various cuts through the phase diagram in Fig. 3.10. It has been suggested that the isotropic-nematic transition of rods is continuous in two dimensions [93]. We have chosen a threshold value for the isotropic-nematic phase transition, $S_t = 0.11$, such that for an infinite interaction energy the value predicted by the Onsager theory is recovered. Our threshold value is similar to the threshold value $S = 0.2$ that has been chosen in Ref. [58].

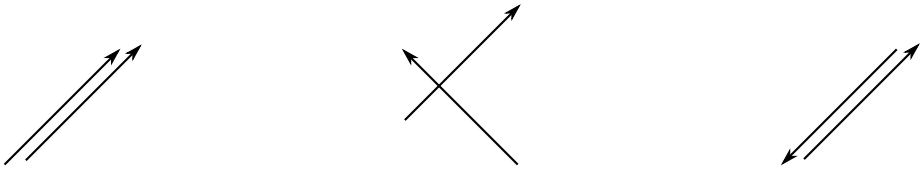

(a) parallel; $S = +1$ (b) perpendicular; $S = -1$ (c) antiparallel; $S = +1$

Figure 3.9: The nematic order parameter, Eq. (3.5), for two rods in different configurations: (a) parallel, (b) perpendicular, and (c) antiparallel.

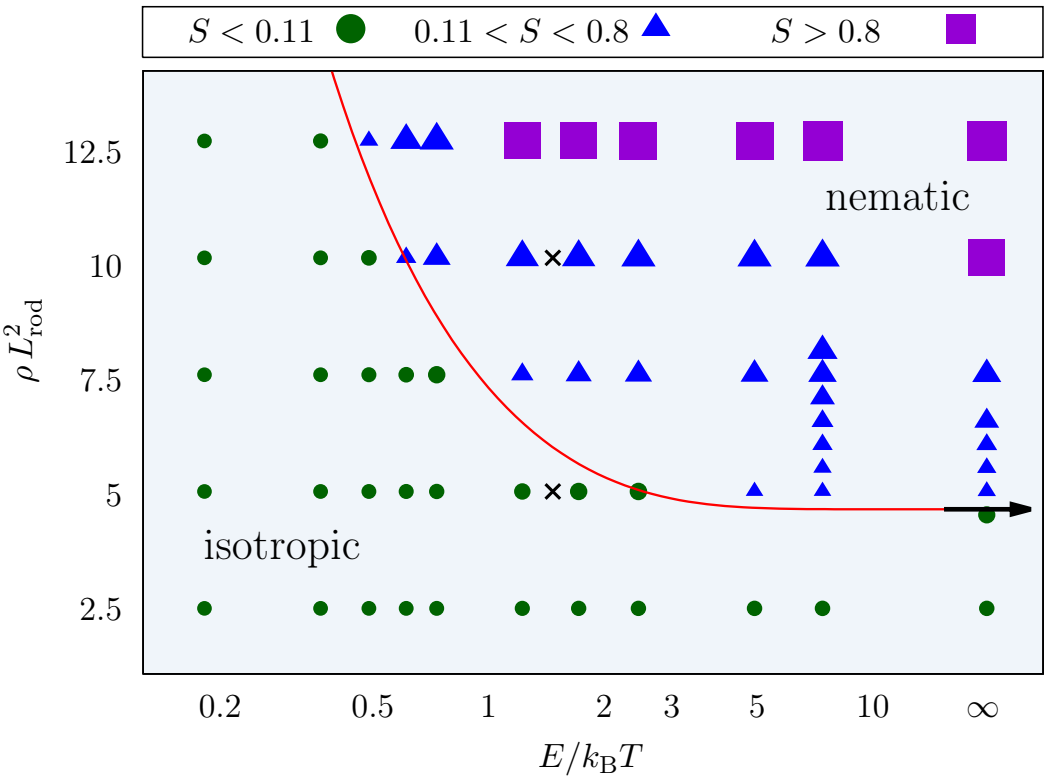

Figure 3.10: Phase diagram for passive rod systems with different densities (ρ) and energy barriers (E). In addition to color/symbol coding, the size of each triangle is proportional to the nematic order parameter S [Eq. (3.5)]. Bottom left: isotropic phase with $S < 0.11$; top right: nematic phase with $S > 0.8$; middle: nematic phase with $0.11 < S < 0.8$. The black arrow indicates Onsager's isotropic-nematic transition density, $\rho_c\, L_{\mathrm{rod}}^2 = 3\pi/2$. The red line is given by Eq. (3.6). Crosses ($\times$) mark the parameters that have been used for the Brownian dynamics simulations in Figs. 1.15(b) and 1.15(a).

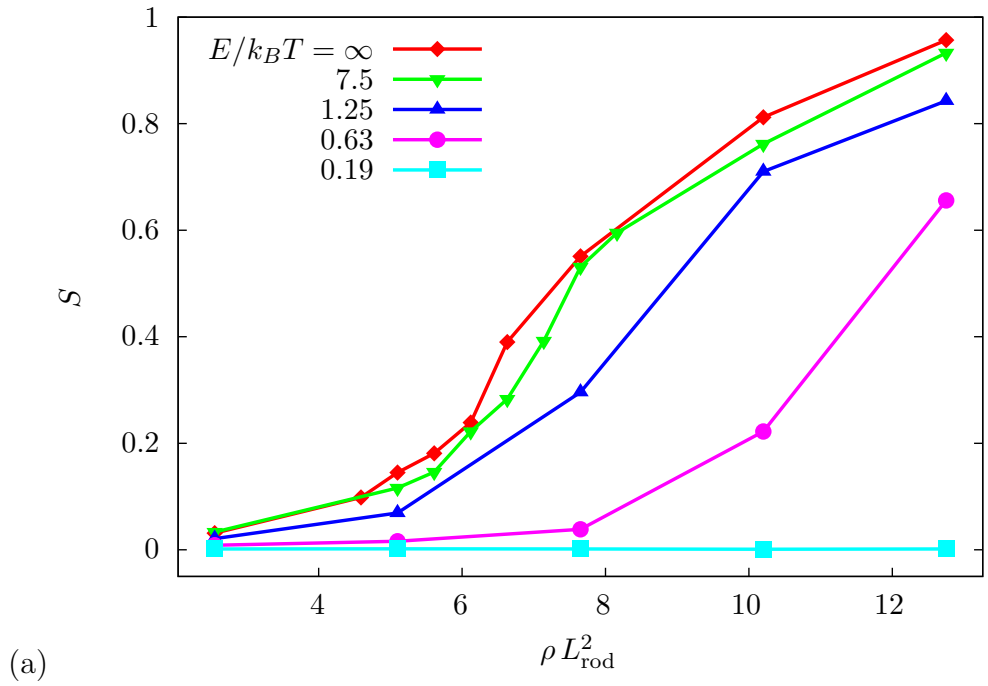

(a)

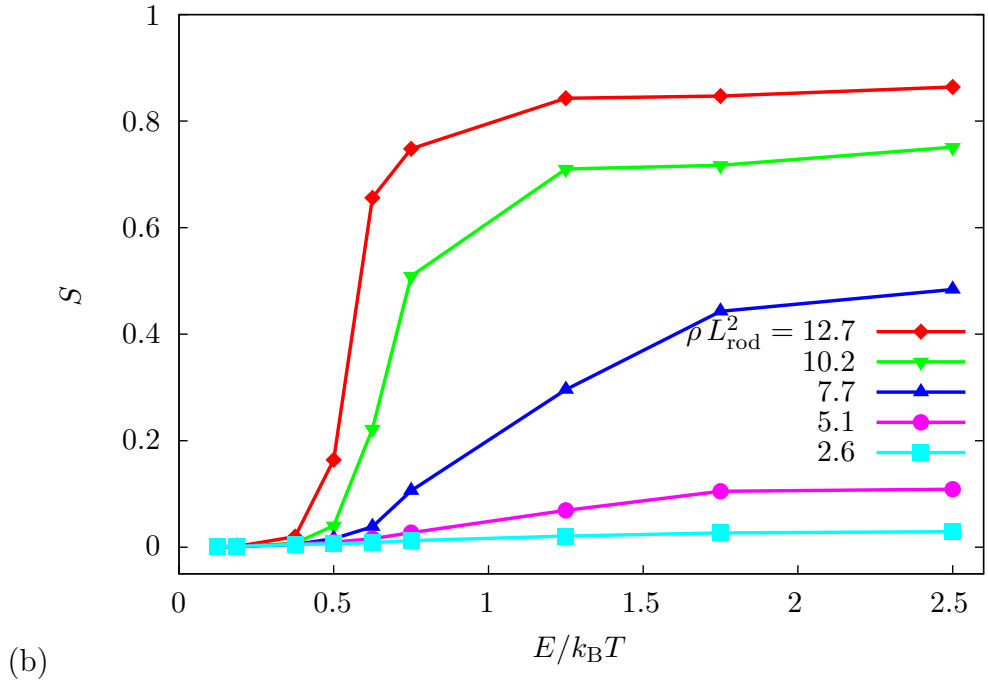

(b)

Figure 3.11: Nematic order parameter S, used to determine the phase transition for passive rods, as a function of (a) the rod density ρ for several energy barriers E and (b) the energy barrier E for several rod densities ρ.

3.6 Generalized Onsager theory

For finite energy barrier E, we generalize the approach presented in Ref. [93] based on bifurcation theory to obtain the critical density for the isotropic-nematic transition. The distribution function for the rod orientation is given by $f(\theta)$, which satisfies

$$\ln[2\pi f(\theta)] = C + \lambda \int_{\theta=0}^{2\pi} F(\theta,\theta') f(\theta') \mathrm{d}\theta' \,, \tag{3.7}$$

where the constant C is determined by the normalization of $f(\theta)$,

$$\int_{\theta=0}^{2\pi} f(\theta) \mathrm{d}\theta = 1 \,. \tag{3.8}$$

We define $h(\theta)$ as

$$h(\theta) = 2\pi f(\theta) - 1 \,, \tag{3.9}$$

such that $h(\theta) = 0$ corresponds to an isotropic distribution. Using Eqs. (3.7)–(3.9), we can write

$$h(\theta) = -1 + \frac{\exp(\lambda \int F(\theta,\theta') h(\theta') \mathrm{d}\theta'/2\pi)}{(1/2\pi) \int \exp(\lambda \int F(\theta,\theta') h(\theta') \mathrm{d}\theta'/2\pi) \mathrm{d}\theta} \,. \tag{3.10}$$

We assume that the interaction energy of two rods is either 0 or E, depending on whether they cross each other. This approximation is justified if the rods are very thin and the complete overlap of two rods—which is energetically very unfavorable—is excluded. In the regime where $L_{\mathrm{rod}} \gg r_{\mathrm{min}}$, the parameter λ and the kernel F are given by

$$\lambda = \frac{1}{4} \rho \pi L_{\mathrm{rod}}^2 \,, \tag{3.11}$$

$$\begin{aligned} (1/2\pi) F(\theta,\theta') &= (-2/\pi^2) \sin(\theta) \\ &\quad \times [1 - \exp(-E/k_{\mathrm{B}}T)] \,. \end{aligned} \tag{3.12}$$

Substituting Eqs. (3.11) and (3.12) in Eq. (3.10) gives

$$h(\theta) = -1 + \frac{\exp[-\rho K h(\theta)]}{(1/\pi) \int_0^{\pi} \exp[-\rho K h(\theta)] \mathrm{d}\theta} \,, \tag{3.13}$$

where the operator K is defined as

$$\begin{aligned} K h(\theta) &= (L_{\mathrm{rod}}^2/\pi)[1 - \exp(-E/k_{\mathrm{B}}T)] \\ &\quad \times \int_0^{\pi} \sin(\theta') h(\theta - \theta') \mathrm{d}\theta' \,. \end{aligned} \tag{3.14}$$

For $h(\theta)$ to have bifurcation point in ρ,

$$w(\theta) = -\rho K w(\theta) \tag{3.15}$$

has to have an eigenfunction with two maxima at $w(0) = w(\pi)$ and no further maxima. The corresponding eigenvalue determines the density at which bifurcation occurs. The desired eigenfunction is $\cos 2\theta$ with the eigenvalue $-3/2$; thus the bifurcation density that corresponds to the isotropic-nematic transition is

$$\rho_c = \frac{3\pi}{2L_{\mathrm{rod}}^2} \frac{1}{[1 - \exp(-E/k_{\mathrm{B}}T)]} \,. \tag{3.16}$$

Chapter 4

Cluster formation for active rod suspensions

A homogeneous system of self-propelled particles with no clusters has important qualitative differences from an aggregated system with clusters. For example, a clustered system has different rheological properties than a homogeneous system [97–99]. In the case of biological microswimmers, cluster formation can have profound effects on nutrition availability and defense mechanisms. Therefore, studying cluster formation is important both for biological and synthetic microswimmer systems. In this chapter, we present the results for the cluster formation of monodisperse (one-component) self-propelled rods. We use Brownian dynamics simulations with the rod model that was introduced in Chapter 2. We will study the more complex case of bidisperse (two-component) self-propelled rods in Chapter 5.

The chapter is organized as follows. First, we present an overview of all observed phases in Sec. 4.1. In Sec. 4.2, we characterize cluster formation by studying the rod densities, and we introduce a characteristic gas density for rods. In Sec. 4.3, we discuss the minimum density required for cluster formation. In Sec. 4.4, we measure the cluster size distribution for different systems. Finally, in Sec. 4.5, we study cluster dynamics using autocorrelation functions for rod orientations.

4.1 Phase diagram

We have performed simulations with large numbers of rods to characterize the collective behavior of self-propelled rod systems. After initiating the rods with random positions and orientations in the two-dimensional (2D) plane, the rods move by their propulsion force and are affected by interactions with other rods and thermal noise. Some snapshots of the simulations are shown in Figs. 1.15, 4.1 and 4.2. More snapshots and movies can be found in the Supplemental Material

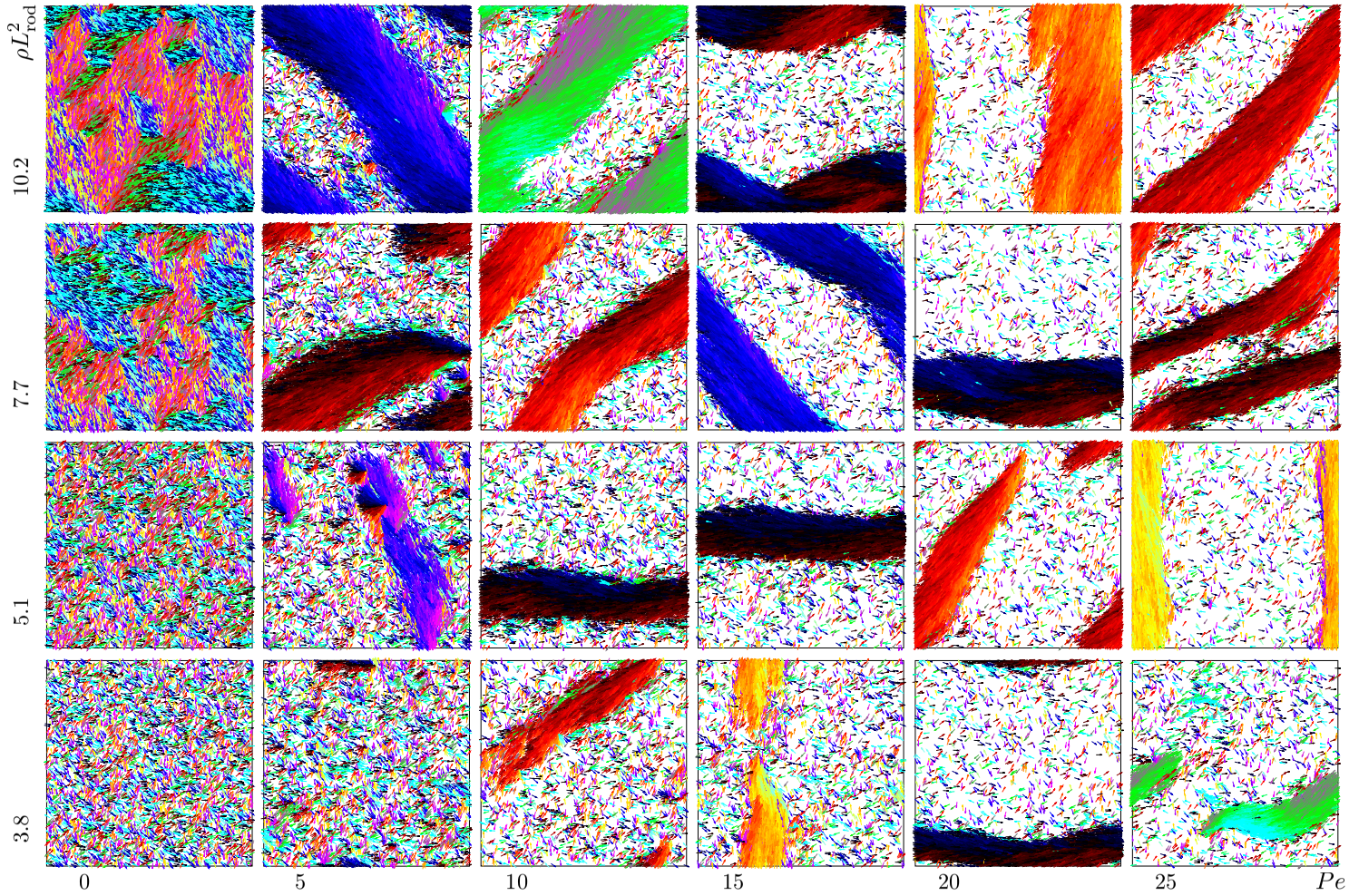

Figure 4.1: Formation of giant clusters: Snapshots of self-propelled rod systems with various densities ($3.8 \leq \rho L_{\rm rod}^2 \leq 10.2$) and low/intermediate Péclet numbers ($0 \leq \mathrm{Pe} \leq 25$). At $\mathrm{Pe} = 0$ (no activity) isotropic and nematic phases are observed (top-left and bottom-left, respectively). For the rest of systems, giant clusters form. Note the density of the dilute region, the gas density, decreases with increasing Pe, while it remains relatively constant for different densities (and the same Pe), in accordance with our prediction in Eq. (4.4). See also Fig. 4.5 for a quantitative comparison.

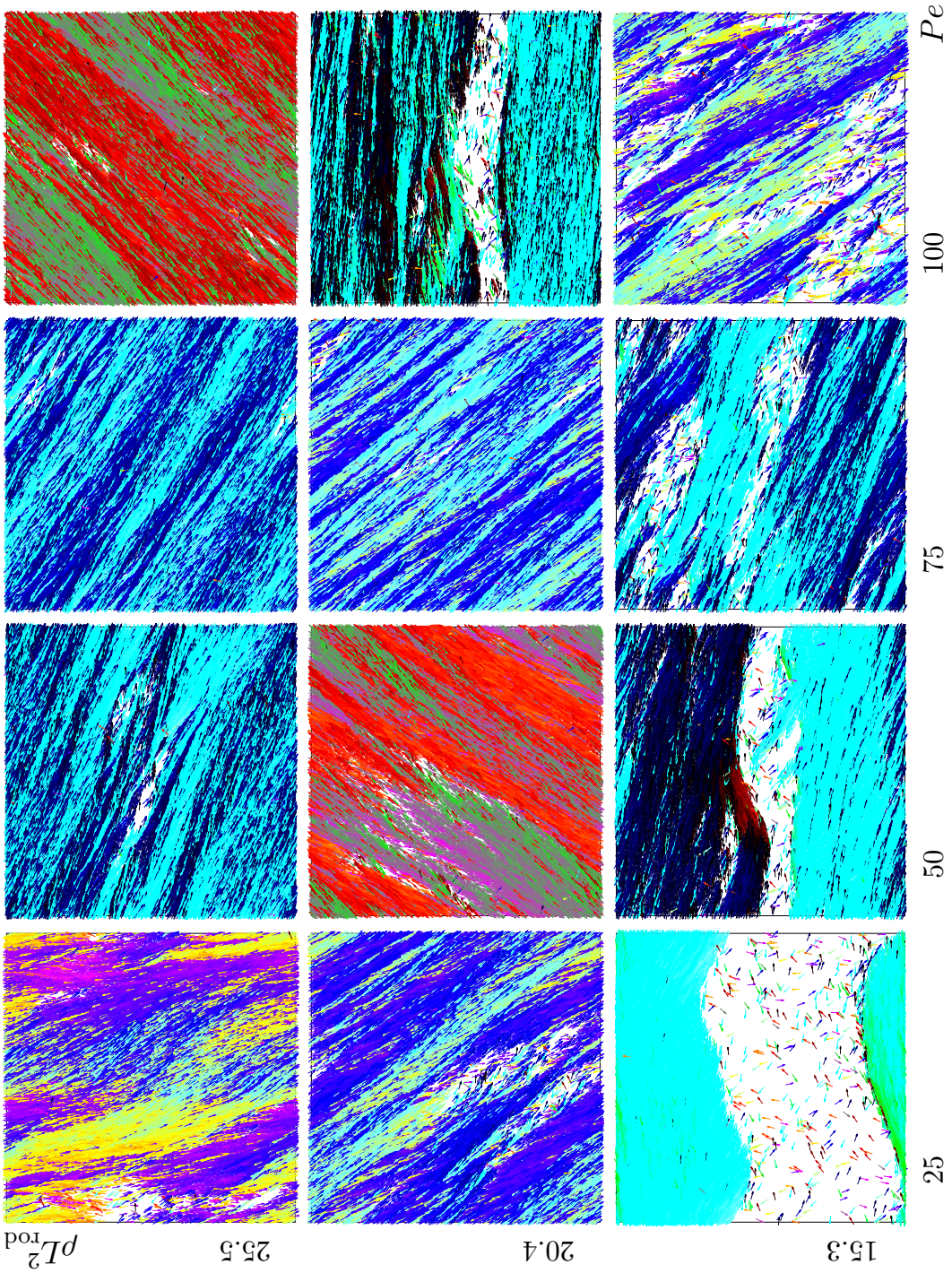

Figure 4.2: Formation of lanes at very high densities: Snapshots of self-propelled rod systems with high densities ($15.3 \leq \rho L_{\mathrm{rod}}^2 \leq 25.5$) and high Péclet numbers ($25 \leq \mathrm{Pe} \leq 100$). The streams of rods with different colors move in opposite directions.

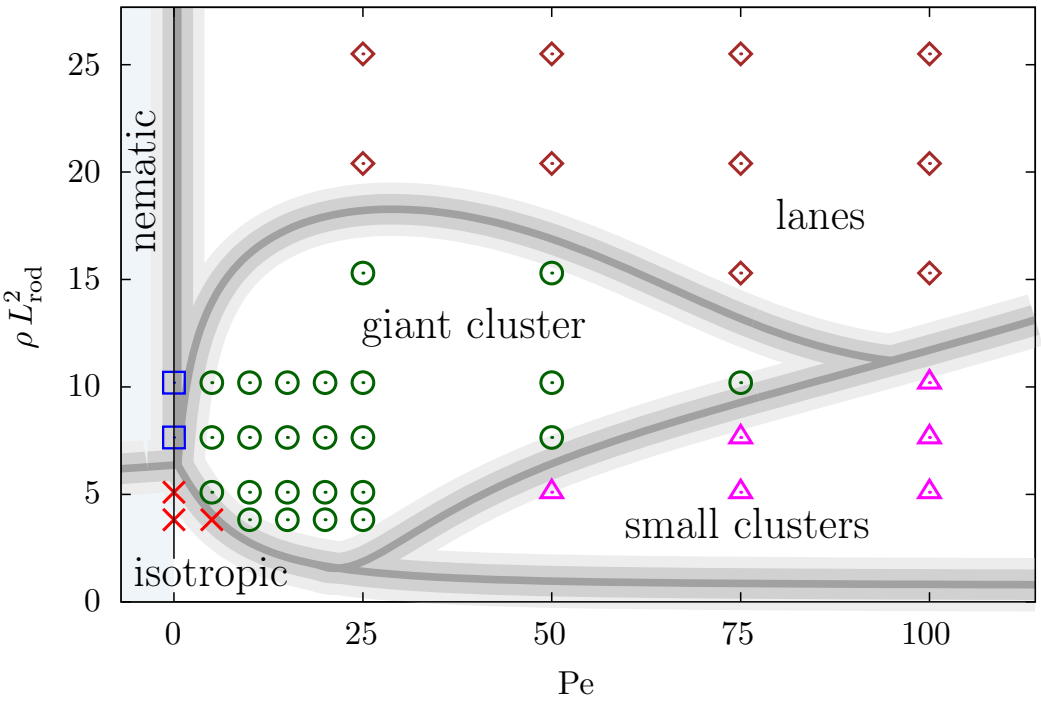

Figure 4.3: Phase diagram for self-propelled rods with different densities (ρ) and Péclet numbers (Pe). The energy barrier is $E = 1.5\,k_{\mathrm{B}}T$ and the rod aspect ratio is 18. Bottom-left: isotropic phase at low ρ and Pe; top-left: nematic phase at high ρ and Pe $= 0$; top-right: laning phase at very high ρ; bottom-right: cluster-breakup phase at high Pe, i.e., high penetrability coefficients Q; center: giant cluster phase at intermediate ρ and Pe. The gray lines are guides to the eye. Note that the region Pe < 0 has no physical meaning and that the nematic state is found for passive rods with Pe $= 0$.

of Ref. [35]. A phase diagram of self-propelled rods with varying density and Péclet number is shown in Fig. 4.3.

For Péclet numbers [Eq. (2.11)] in the range $1 \leq \mathrm{Pe} \lesssim 80$, we find giant clusters that span the entire simulation box and form as a result of the alignment interaction due to the rod-rod repulsion, as explained qualitatively in Refs. [50, 100]; see the snapshots in the top right of Fig. 4.1. At the cluster perimeter, the clusters steadily lose rods due to the rotational diffusion and at the same time acquire new rods that collide and align. The clusters are polar and almost all rods within a giant cluster move in the same direction. However, we expect that the system is essentially in an isotropic phase, and that for a sufficiently large system size the clusters can randomly change direction. The polar order of our giant clusters which span the simulation box is due to symmetry-breaking collisions because of the roughness of the rods. In the early stage of the formation of giant clusters, some of the eventually polar clusters are composed of streams of rods that move in opposite directions.

Upon further increase of Pe the clusters start to break; see Fig. 4.6. Smaller clusters are observed until they become as small as about five rods per cluster for $\mathrm{Pe} \gtrsim 100$. For very high densities, $15.1 \leq \rho\, L_{\mathrm{rod}}^2 \leq 25.5$, when the dense region spans the entire simulation box, we find a laning phase that is composed of streams of rods that move in opposite directions; see Fig. 4.2. The laning phase is nematic, similar to the nematic lanes that have been observed for the Vicsek model in simulations [50] and analytical calculations [101].

Our phase diagram in Fig. 4.3 may be compared with the phase diagram in Ref. [62] for self-propelled rods without noise that interact segment-wise via a Yukawa potential [Fig. 1.14(a)]. Since our model incorporates noise and has a capped repulsive interaction potential, we can only compare both models in the medium Pe regime, where the noise does not dominate ($\mathrm{Pe} \gg 1$) and where the rods are not completely penetrable ($\mathrm{Pe} \lesssim 75$). For aspect ratio 18 used in our simulation, we see qualitatively similar behavior with increasing density, namely the transition from the isotropic phase to the swarming (clustering) phase and then to the laning phase.

A comparison of our phase diagram in Fig. 4.3 with that of Ref. [34] (Fig. 1.13) shows that we do not observe jammed giant clusters as reported in Ref. [34], because we employ a smoother potential profile along the rod; see Fig. 2.5.

4.2 Rod densities

We measure densities of rods in cells of side length $2\,L_{\mathrm{rod}}$ and construct a distribution of monomer densities for each system; see Fig. 4.4. For a homogeneous system of rods, the distribution has a single narrow peak at the average density of the system, ρ_i. This can be seen for example in the histograms for $\mathrm{Pe} = 0$ that correspond to the systems where no cluster formation is observed; see the left

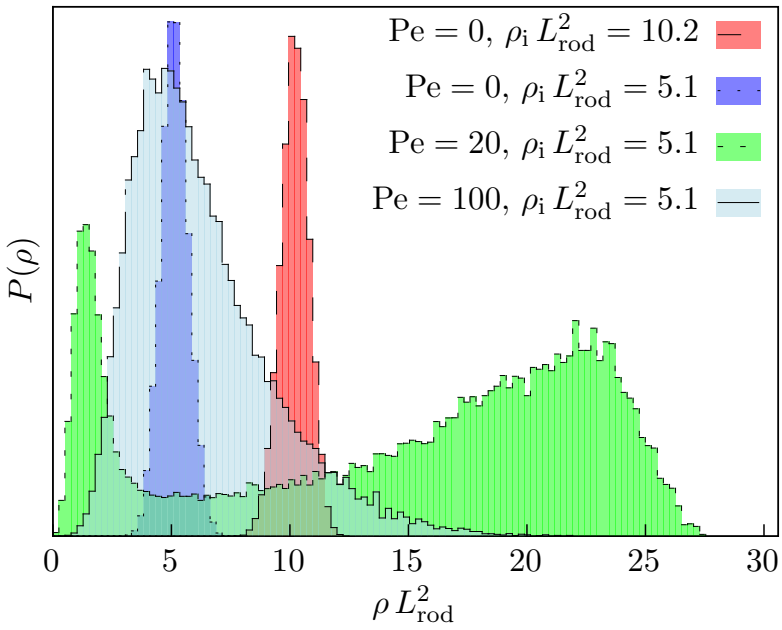

Figure 4.4: Density distributions for the systems shown in snapshots of Fig. 1.15. ρ_i is the average density. The distributions are not normalized and only the position of peaks can be compared.

column in Fig. 4.1. For systems with self-propelled rods, the density distribution can change from a unimodal to a more complicated distribution that shows phase separation between dilute and dense regions of rods. For Pe = 20 the distribution has a large peak at low density and a very broad peak at higher densities.

4.2.1 Gas density

The density distribution for the system with Pe = 20 in Fig. 4.4 shows that it consists of a high-density cluster in a "gas" of rods. The density of this cluster-free gas corresponds to the position of the first peak in the density distribution. In the following, we denote the density of this region as ρ_{gas}.

We define ρ_{gas} as the position of the first local maximum in the density distribution, which is at least as high as 80% of the absolute maximum. In Fig. 4.5(a), ρ_{gas} is plotted as a function of Pe for several values of ρ_i and E. We find $\rho_{gas} \sim \mathrm{Pe}^{-1}$ for small Pe and an increase of ρ_{gas} with increasing Pe for high Pe. The gas density is to a large extent independent of the average rod density of the entire system; see Fig. 4.5(a). This behavior is analogous to the *vapor density* for liquid-gas phase coexistence in conventional liquids, where the density of the gas phase only depends on the temperature and is independent of the volume of the liquid phase.

The dependence of ρ_{gas} on Pe and ρ in the low Pe range can be quantita-

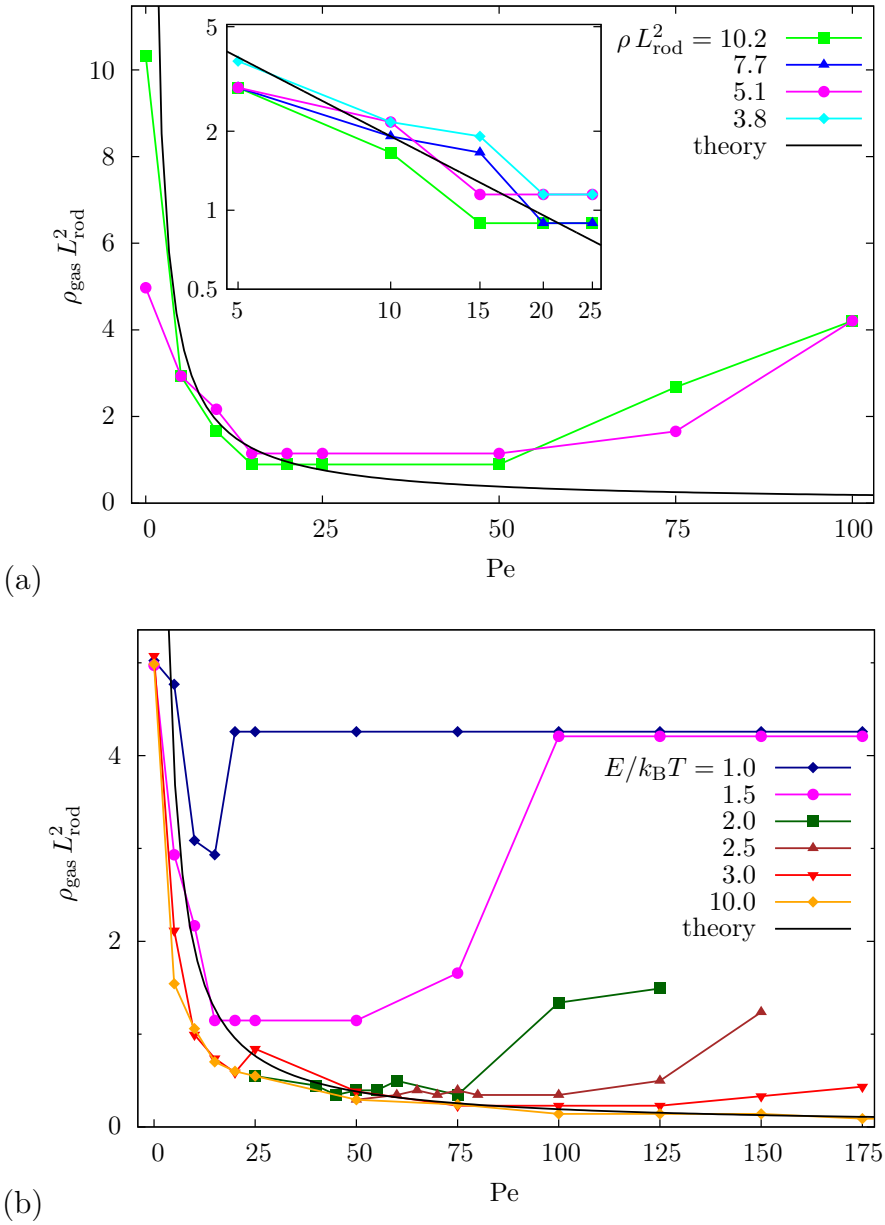

Figure 4.5: Gas density as a function of the Péclet number for different average rod densities and energy barriers compared with $\rho^*_{\rm gas}$ in Eq. (4.4). (a) Gas densities for $E = 1.5\, k_B T$ and several rod densities. Inset: double-logarithmic plot of $\rho_{\rm gas}$ for $5 < {\rm Pe} < 25$. (b) Gas densities for average rod density $\rho\, L^2_{\rm rod} = 5.1$ and several energy barriers. The errors are given by the peak width for the density histograms, $\rho\, L^2_{\rm rod} \simeq 0.5$.

tively explained by a rate equation [45]. In the stationary state, the rate of rods joining a cluster equals the rate of rods leaving a cluster. Assuming an isotropic distribution of rods in the gas, the number of rods joining the cluster from an infinitesimally small box of side length $\mathrm{d}x$ and $\mathrm{d}y$ is $\mathrm{d}^3N = \rho\,\mathrm{d}x\,\mathrm{d}y\,\mathrm{d}t(1-\cos\theta)/2$, where $\theta = \cos^{-1}(\mathrm{d}x/(v\mathrm{d}t))$ is the half angle of a cone inside which rods reach the wall in a given time $\mathrm{d}t$, and x is the distance to the cluster "wall." Integrating d^3N over x from 0 to $v\mathrm{d}t$ gives the attachment rate

$$J_{\mathrm{att}} = \frac{\mathrm{d}^2N}{\mathrm{d}t\mathrm{d}y} = \frac{\rho v}{4} = \frac{\rho D_\parallel \mathrm{Pe}}{4L_{\mathrm{rod}}}\,, \tag{4.1}$$

where we have used the definition of Péclet number in Eq. (2.11).

The detachment rate J_{det} is determined by the rotational diffusion of the rods; the typical time a rod needs to diffuse by an angle α is

$$\tau = \frac{\alpha^2}{2D_r}\,. \tag{4.2}$$

Assuming that a complete detachment from the cluster requires $\alpha = \pi/2$ and that rods are placed regularly along the border of a cluster, the detachment rate is found to be

$$J_{\mathrm{det}} = \frac{1}{L_{\mathrm{rod}}\tau} = \frac{8D_r}{\pi^2 L_{\mathrm{rod}}}\,. \tag{4.3}$$

By equating J_{att} and J_{det}, we find a characteristic gas density ρ^*_{gas} as a function of Pe,

$$\rho^*_{\mathrm{gas}} = \frac{32}{\pi^2}\frac{D_r}{D_\parallel}\frac{1}{\mathrm{Pe}} = \frac{192}{\pi^2 L^2_{\mathrm{rod}}}\frac{1}{\mathrm{Pe}}\,, \tag{4.4}$$

where we have used $D_r/D_\parallel = \gamma_\parallel/\gamma_r = 6/L^2_{\mathrm{rod}}$. Note that the ρ^*_{gas} only depends on L_{rod} and Pe and is independent of the average system density ρ, which is consistent with the simulation results. This implies that the giant cluster grows until the gas density reaches ρ^*_{gas}.

Note that this estimate includes several approximations, in particular using free rotational diffusion for rods at the border of the cluster and assuming that complete detachment requires the rods to diffuse by $\alpha = \pi/2$. As shown in Fig. 4.5, the analytical estimate in Eq. (4.4) agrees well with the simulation results in the small-Pe range without any adjustable parameters.

4.2.2 Binding energy of rods to the cluster

The independence of the characteristic gas density ρ^*_{gas} from the average density of the system ρ is analogous to a vapor density for rods. Here we follow this analogy to obtain an effective binding energy gain E_b for rods that are part of the cluster [102]. We use an ideal-gas model in two dimensions to represent the rods in the gas phase. The activity and the anisotropy of the rods are intentionally

not taken into account explicitly and enter via the effective binding energy. The free energy for the rods in the gas is thus

$$\begin{aligned} F_{\text{gas}} &= N k_{\text{B}} T \ln\left(\frac{N\Delta}{A}\right) \\ &= N k_{\text{B}} T \ln\left(\rho^*_{\text{gas}} L_{\text{rod}} r_{\text{min}}\right) , \end{aligned} \tag{4.5}$$

where N is the number of rods in the gas, Δ is the area of each rod, and A is the area accessible for the rods in the gas.

In the cluster, each rod gains a binding energy E_b,

$$F_{\text{cluster}} = N E_b \, , \tag{4.6}$$

where N here is the number of rods in the cluster. In equilibrium, the chemical potential $\mu = \partial F / \partial N$ in the gas and in the cluster should be equal. This gives the effective binding energy per rod for the rods inside the giant cluster,

$$\begin{aligned} E_b &= k_{\text{B}} T \ln(\rho^*_{\text{gas}} L_{\text{rod}} r_{\text{min}}) \\ &= k_{\text{B}} T \left[\ln\left(192/\pi^2\right) - \ln(\text{Pe}\, L_{\text{rod}}/r_{\text{min}})\right] . \end{aligned} \tag{4.7}$$

The effective binding strength increases logarithmically with the product of Péclet number and the rod aspect ratio. For aspect ratio 18 and Pe $\approx$ 25 used in our simulations, we find effective binding energies of $E_b \approx -0.1\, k_{\text{B}} T$, which are comparable to binding energies for the gas-liquid critical point for colloidal systems [103].

4.2.3 Cluster breakup

For $E = 1.5 k_B T$, clusters break up when Pe $\gtrsim$ 80, which implies penetrability coefficients $Q \gtrsim 50$ [Eq. (2.12)]. We observe that in the regime of cluster break-up, individual rods and even small clusters can pass through each other; see Fig. 4.6. Moreover, the density distributions for such systems become unimodal, but with a larger spread compared to isotropic systems with low Péclet numbers; see the distribution with Pe = 100 in Fig. 4.4. In our simulations Pe is proportional to the propulsion force, and a high propulsion force thus facilitates crossing of rods. As a result, fewer rods aggregate in a large cluster and the rod density in the dilute region ρ_{gas} increases; see Figs. 4.6 and 4.5. Cluster break-up starts when the propulsion force, $F_{\text{rod}} = Q\, E / L_{\text{rod}}$, is comparable to the maximum force for bead-bead interaction, $F_{\text{int}} = \max(-\text{d}\phi/\text{d}r)$. Equating F_{int} to F_{rod} gives the critical value of the penetrability coefficient for cluster break-up,

$$Q^* = \frac{F_{\text{int}} L_{\text{rod}}}{E} = 28 \, , \tag{4.8}$$

where $F_{\text{int}} = -\text{d}\phi/\text{d}r|_{r=r_0}$ and $r_0 = 0.192$ is found by numerically solving the equation $\text{d}^2\phi(r)/\text{d}r^2 = 0$ for the potential in Eq. (2.10). In Fig. 4.8, Q^* is

Figure 4.6: Cluster breakup for different densities: Snapshots of self-propelled rod systems with intermediate/high densities ($5.1 \leq \rho L_{\mathrm{rod}}^2 \leq 10.2$) and high Péclet numbers ($25 \leq \mathrm{Pe} \leq 100$). Energy barrier is fixed at $E = 1.5\, k_{\mathrm{B}}T$. While for $\mathrm{Pe} = 25$ only one integrated cluster is observed, for higher Péclet numbers clusters start to break. Therefore the gas density ρ_{gas} increases with increasing Pe; compare Fig. 4.5(a).

Figure 4.7: Clustering window for different energy barriers: Snapshots of self-propelled rod systems with different Péclet numbers ($0 \leq \mathrm{Pe} \leq 150$) and energy barriers ($1.0 \leq E/kBT \leq 3.0$). The density is fixed at $\rho L_{\mathrm{rod}}^2 = 5.1$. The range of Pe for which cluster formation is observed (the "clustering window") is different for various E values; compare Figs. 4.5(b) and 4.8. For low energy barrier $E = 1.0\,k_{\mathrm{B}}T$ clusters only form in the narrow range of $10 \leq \mathrm{Pe} \leq 20$. For intermediate energy barrier $E = 1.5\,k_{\mathrm{B}}T$ clusters are visible for a larger range of $5 \leq \mathrm{Pe} \leq 75$. For $E = 3.0\,k_{\mathrm{B}}T$, large clusters remain in the system even until $\mathrm{Pe} = 175$. Please note that not all of the snapshots are shown here.

plotted for various energy barriers; see Fig. 4.7 for snapshots. Although the angular dependence for crossing of rods (Fig. 2.6) is neglected in the estimate in Eq. (4.8), we find reasonable agreement with the simulation results without any adjustable parameters. However, there is less agreement for small energy barriers, corresponding to small Pe. The deviations may be accounted for by the noise that for small Pe is comparable with the propulsion force (but that is not considered in the analytical estimate).

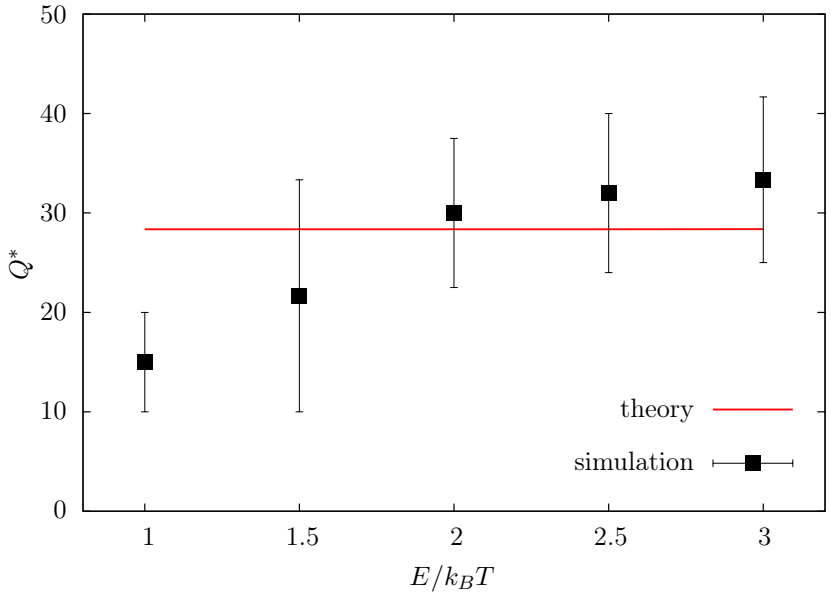

Figure 4.8: Critical penetrability coefficient Q^* at which clusters start to break vs the energy barrier E, compared with the analytical estimate given by Eq. (4.8). Average rod density is $\rho L_{\text{rod}}^2 = 5.1$. The points from the simulations are the Péclet numbers at which ρ_{gas} has a minimum for each energy barrier; compare Fig. 4.5.

4.3 Onset of cluster formation

In Sec. 4.2, we characterized clusters of self-propelled rods. We showed that the clusters do not form for passive systems with Pe = 0 and also for systems with very low densities $\rho L_{\text{rod}}^2 \lesssim 2$; see the left column and the bottom left of Fig. 4.1. Moreover, we showed in Sec. 4.2.3 that clusters break at very high Péclet numbers. In the rest of the systems, we do observe the formation of giant clusters. Here we investigate the minimum density required for cluster formation.

In the absence of any attractive interaction between rods, as in our model described in Chapter 2, the clusters emerge as the result of an interplay between three ingredients. First, the self-propulsion force drives the cluster formation. It

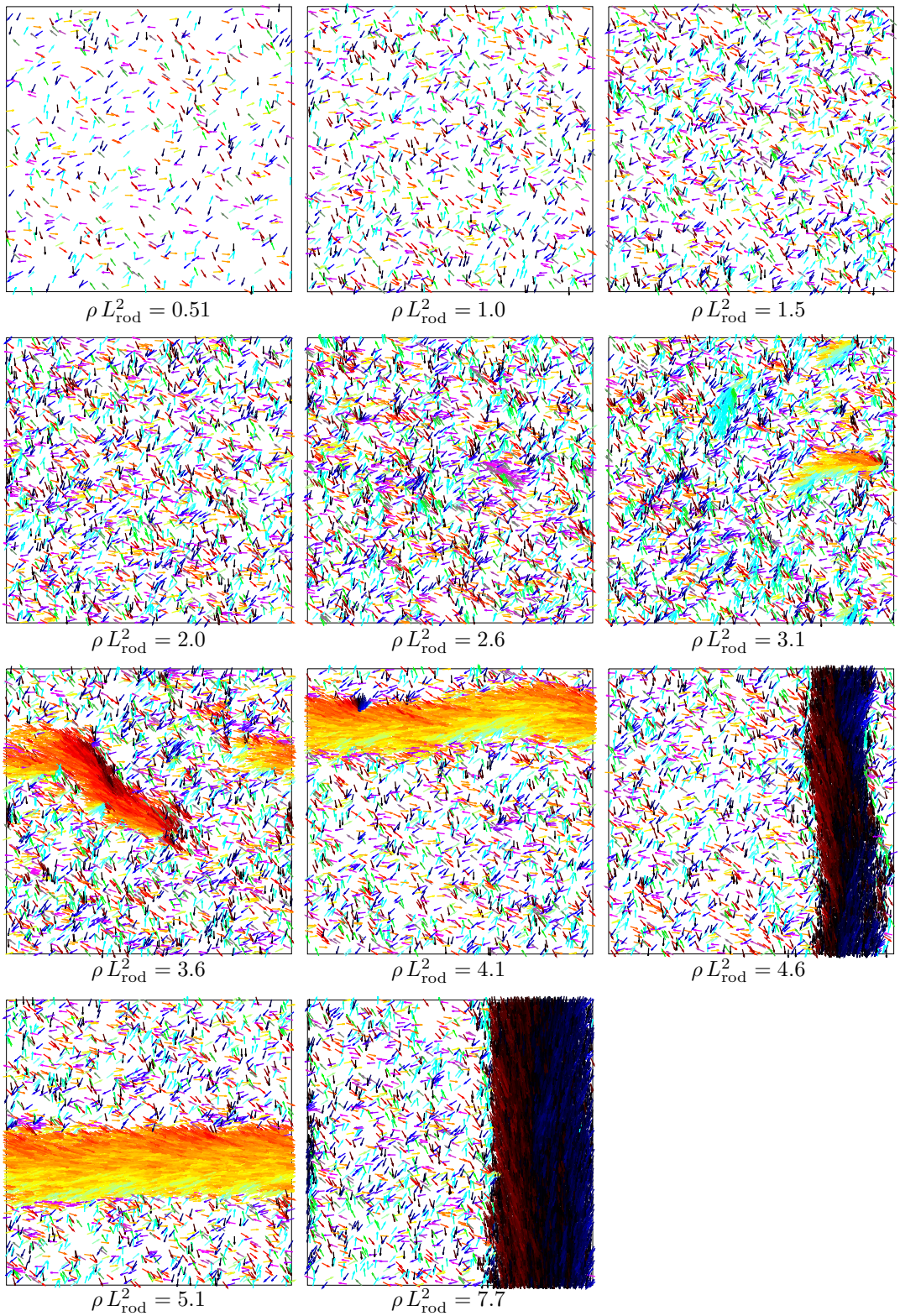

Figure 4.9: Onset of cluster formation with increasing density: Snapshots of self-propelled rod systems with energy barrier $E = 1.5\, k_{\mathrm{B}}T$ and Péclet number $\mathrm{Pe} = 10$ for different scaled densities $0.51 \leq \rho\, L_{\mathrm{rod}}^2 \leq 7.7$. Clusters appear for $\rho\, L_{\mathrm{rod}}^2 \geq 3.1$

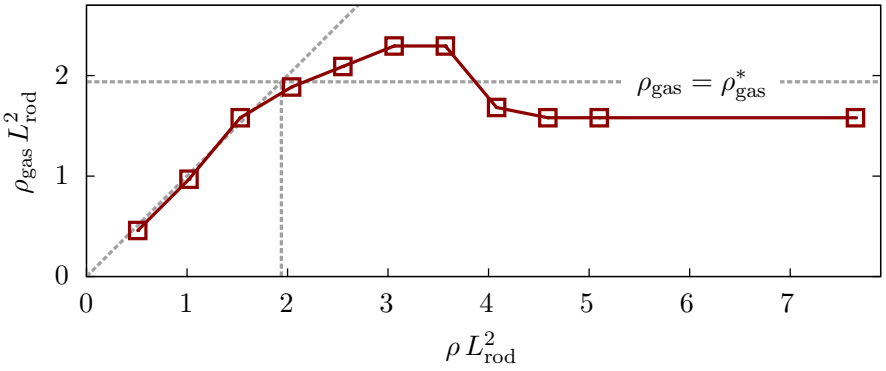

Figure 4.10: The gas density ρ_{gas} vs the average rod density ρ. The tilted dashed line represents $\rho_{\mathrm{gas}} = \rho$, while the horizontal dashed line is the characteristic gas density ρ^*_{gas} [Eq. (4.4)].

has been shown that the self-propulsion acts as an effective attractive interaction [35, 60, 102]. Second, in order to have a non-negligible steric interaction between rods, a finite value of energy barrier E is needed, as described in Sec. 2.5. Third, the clusters only form when the overall density of the system is higher than a threshold value, ρ_c.

Here, we propose that this threshold density for cluster formation is in fact the characteristic gas density ρ^*_{gas} that we obtained in Sec. 4.2.1 [Eq. (4.4)]. Fig. 4.9 shows snapshots of systems with various (low) rod densities. Péclet number and energy barrier are fixed at $\mathrm{Pe} = 10$ and $E = 1.5\, k_{\mathrm{B}}T$, respectively. The characteristic gas density for rods with $\mathrm{Pe} = 10$ is [Eq. (4.4)]

$$\rho^*_{\mathrm{gas}} L^2_{\mathrm{rod}} \,|_{(\mathrm{Pe}=10)} = 1.95\,. \tag{4.9}$$

From the snapshots of Fig. 4.9, we observe that large clusters do not form until $\rho_c\, L^2_{\mathrm{rod}} \approx 3.1$, which is considerably higher than $\rho^*_{\mathrm{gas}}\, L^2_{\mathrm{rod}}$. This "delayed clustering" can also be inferred from Fig. 4.10, where the gas density is presented for the systems shown in the snapshots of Fig. 4.9. We observe a steady linear increase of ρ_{gas} in the form of $\rho_{\mathrm{gas}} = \rho$ for low ρ, followed by an overshoot of ρ_{gas} in the range $2 \lesssim \rho\, L^2_{\mathrm{rod}} \lesssim 4$. At high average densities $\rho\, L^2_{\mathrm{rod}} \gtrsim 4$, the gas density reaches a steady value of $\rho_{\mathrm{gas}}\, L^2_{\mathrm{rod}} \approx 1.6$.

Figure 4.10 shows that in the intermediate density regimes, the gas density ρ_{gas} can be higher than the characteristic gas density ρ^*_{gas}. We attribute this overshoot in ρ_{gas} (and the corresponding delayed clustering visible in Fig. 4.9) to the lack of a nucleus for the cluster formation: We calculated the characteristic gas density in Eq. (4.4) with the assumption that there is a giant cluster in the system which acts as a wall for rods that collide to it. However, for a system with a density which is only slightly above ρ^*_{gas}, such a giant cluster cannot form

due to the fewer number of rods. Therefore, the small clusters that form in those systems easily evaporate due to the rotational diffusion of their constituent rods.

We propose that in the presence of a nucleus (in the form of a wall, obstacle, or a large cluster of a different rod species) the gas density of rods in Fig. 4.10 has no overshoot and it monotonously saturates to the characteristic gas density ρ^*_{gas}. This prediction has been indirectly confirmed in Sec. 5.3.4, where the clustering transition of short rods in Fig. 5.8 happens just where the density of short rods crosses their corresponding gas density ρ^*_{gas}.

A corresponding phenomenon in equilibrium systems is called homogeneous nucleation [104], where a liquid does not freeze due to the lack of a nucleus. For example, it is known that water can be supercooled down to 225 K (−48 °C) provided that it is pure and free of nucleation sites [105].

4.4 Cluster size distributions

We define two rods to be in the same cluster if the nearest distance between them is less than $2r_{\text{min}}$ and the difference in their orientation angles is less than $\pi/6$ [34]. In Fig. 4.11, snapshots of systems with various densities and Péclet numbers are shown, where the rods are color-coded both based on their orientation and also based on the size of the cluster that they are a member of.

In Fig. 4.12, sample cluster size distributions $\Pi(n)$ are presented. For small cluster size n, $\Pi(n)$ decreases with a power law, $\Pi(n) \propto n^{\beta}$ with $\beta < 0$; for large n, $\Pi(n)$ decreases exponentially [33, 34]. For systems with giant clusters, such as the system with $\text{Pe} = 25$, there is a gap in the distribution because they consist of one giant cluster ($n > 10\,000$) and small clusters ($n < 30$) that mostly form near the boundary of the giant cluster. In such systems, the exponent β is calculated only based on the distribution of small clusters.

The power-law exponent for the cluster size distribution first decreases with increasing Péclet number, has a minimum for $\text{Pe} \sim 25$, and then increases for increasing the values of Pe; see Fig. 4.13. We find the exponent to be in the range $-1.5 \geq \beta \geq -3.5$, which agrees with the range $-2 \geq \beta \geq -3.6$ found in Ref. [34] for rods with different aspect ratio and a different interaction potential than in our simulations. A recent experimental study found $\beta = -1.88 \pm 0.07$ for clusters of *M. xanthus* bacteria [20]. As shown in Fig. 4.14, the average size of the clusters, μ_N, increases with increasing Péclet number for $\text{Pe} \lesssim 25$ and decreases if Pe is further increased. The spread of the cluster size, σ_N, shows the same qualitative behavior but decays faster at high Pe values, which shows that the system becomes more homogeneous.

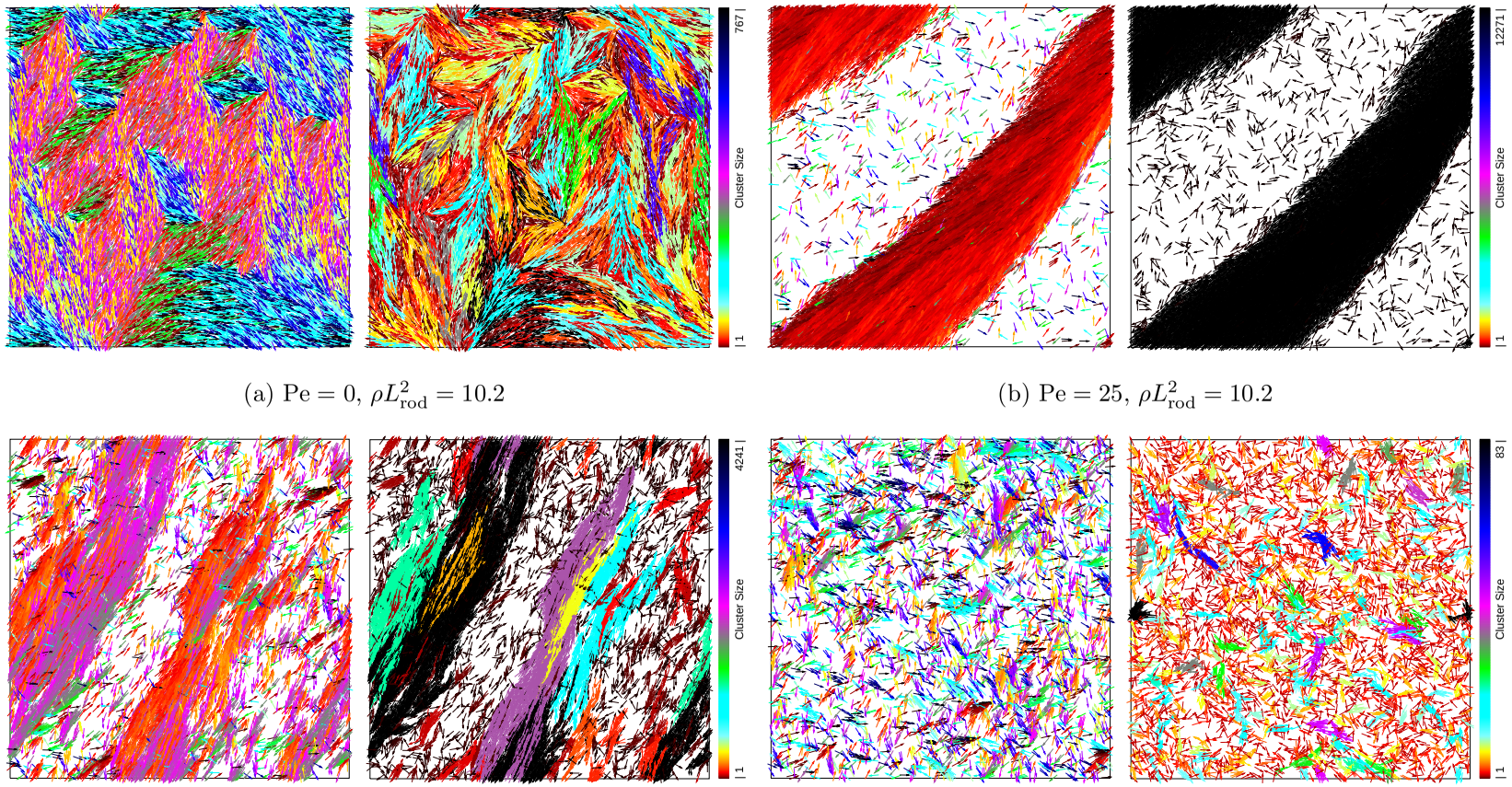

(a) Pe = 0, $\rho L_{\mathrm{rod}}^2 = 10.2$

(b) Pe = 25, $\rho L_{\mathrm{rod}}^2 = 10.2$

(c) Pe = 100, $\rho L_{\mathrm{rod}}^2 = 10.2$

(d) Pe = 100, $\rho L_{\mathrm{rod}}^2 = 5.1$

Figure 4.11: Snapshots of self-propelled rod systems with color coding based on (left) orientation and (right) cluster size. The numbers above the color bars denote the size of the largest cluster found in the system. (a) In a passive system with high density, clusters are detected due to the close packing of rods. (b) In a system with a giant cluster, almost all rods belong to the cluster. (c) At high Pe and high ρ, smaller clusters move in opposite directions. (d) At high Pe and low ρ, only very small clusters exist.

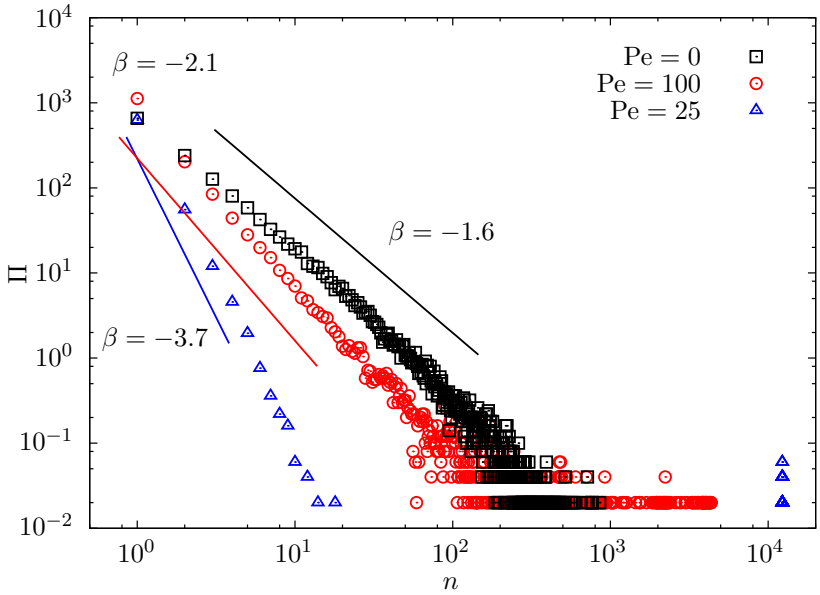

Figure 4.12: Cluster size distributions $\Pi(n)$ for systems shown in the snapshots of Fig. 1.15. Average rod density is $\rho\, L_{\mathrm{rod}}^2 = 10.2$. For small n, the distributions can be fit by a power law, $\Pi(n) \propto n^{\beta}$. The distributions have been averaged over 200 frames in the last 40 000 time steps.

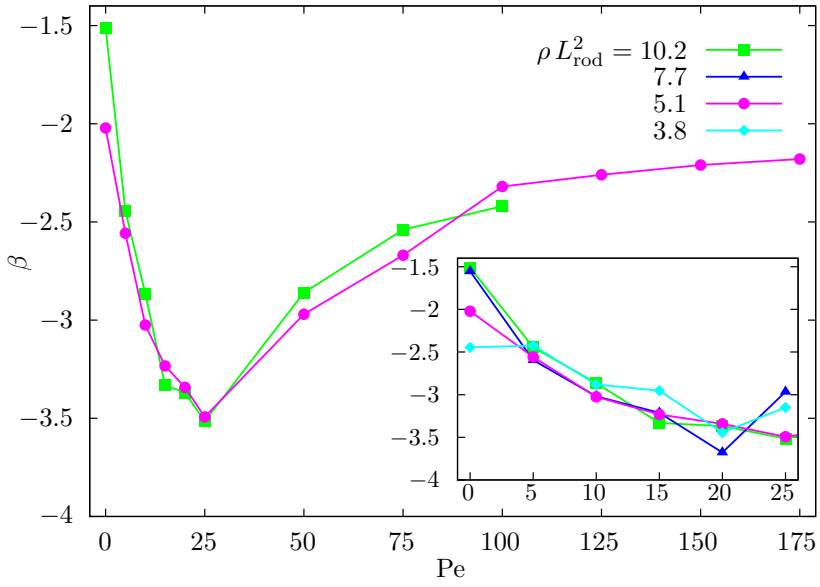

Figure 4.13: The exponent β of the power law for cluster size distributions as a function of Pe for systems with $E = 1.5\, k_{\mathrm{B}}T$ and several average rod densities ρ. The exponents have very weak dependence on ρ. Inset: magnified view for $0 < \mathrm{Pe} < 25$.

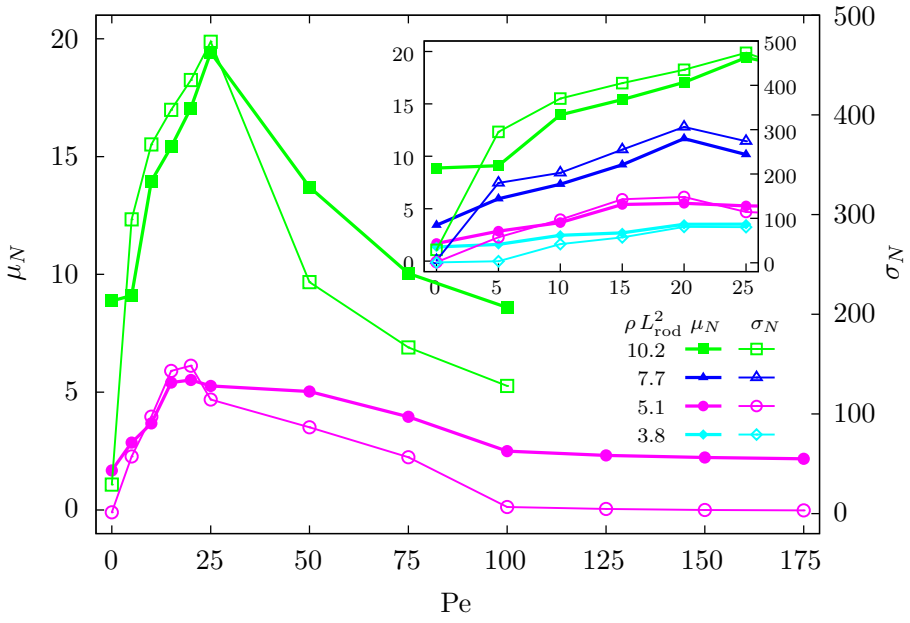

Figure 4.14: Cluster size average μ_N and spread σ_N as function of Pe for several average system densities. The number of rods in systems with $\rho\, L_{\mathrm{rod}}^2 = 10.2$ is 13107. Inset: magnified view for $0 \leq \mathrm{Pe} \leq 25$. The cluster sizes have been averaged over 200 frames in the last 40 000 time steps.

4.5 Polar autocorrelation functions

The clustering dynamics in the systems can be characterized by autocorrelation functions for the rod orientation

$$C(t) = \langle \mathbf{n}_i(t') \cdot \mathbf{n}_i(t'+t) \rangle \ , \tag{4.10}$$

for lag time t, where $\mathbf{n}_i(t')$ is the orientation vector of rod i at time t', and the average is over all rods and over all times t'. Figure 4.15(a) shows $C(t)$ for systems shown in Fig. 1.15. The autocorrelation function $C(t)$ can be fit using a shifted exponential function

$$A(t) = (1-a)e^{-t/\tau} + a \, , \tag{4.11}$$

where τ is the autocorrelation time and a is an autocorrelation base value. A finite value of a is the ratio of rods that do not lose their orientation for the time scale of the measurement. Rods that are inside clusters are less likely to lose their orientation, which corresponds to a high value of a, while free rods in the gas change orientation more frequently because of rotational diffusion. In Fig. 4.15(b), we compare a to the averaged fraction of rods X that are part of the largest cluster in the system for several densities and Péclet numbers. In general, we find good agreement between a and X[1].

The autocorrelation time τ, obtained from the fit with Eq. (4.11), is shown in Fig. 4.16. The autocorrelation time τ does not change substantially for different values of Pe and ρ, and is very similar to the autocorrelation time τ_0 for a single rod. Therefore, while the giant cluster moves persistently within simulation time, the rotational diffusion of a rod outside the cluster is only weakly affected by occasional collisions of other rods.

[1]The values of a and X do not agree for Pe = 0, where rods are either freely moving due to noise (isotropic regime) or stuck in nonmotile clusters (nematic regime). In the former case, there is hardly any orientation preservation ($a \ll 1$) and there is no large cluster ($X \ll 1$). In the latter case, rods hardly change their orientation ($a \sim 1$) but are distributed over small clusters ($X \ll 1$); see Fig. 4.11(a).

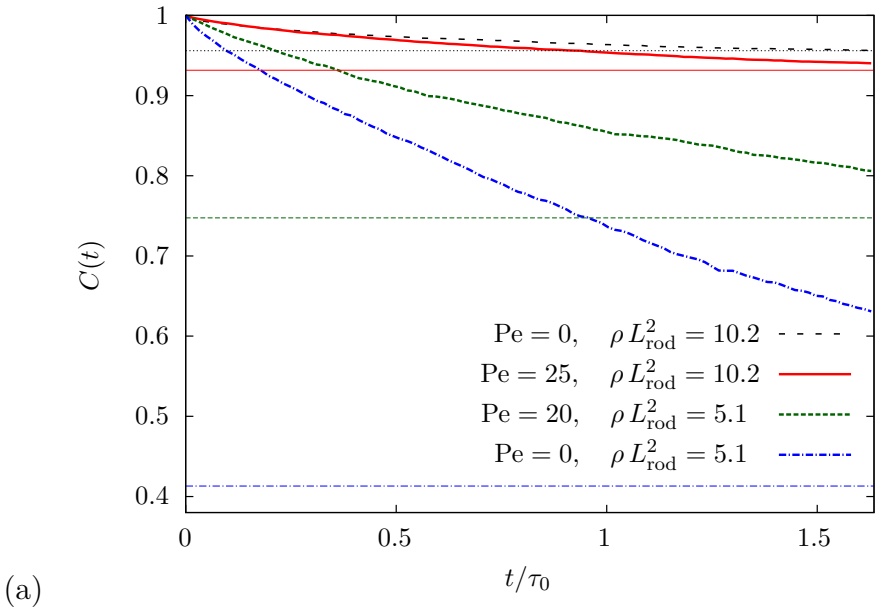

(a)

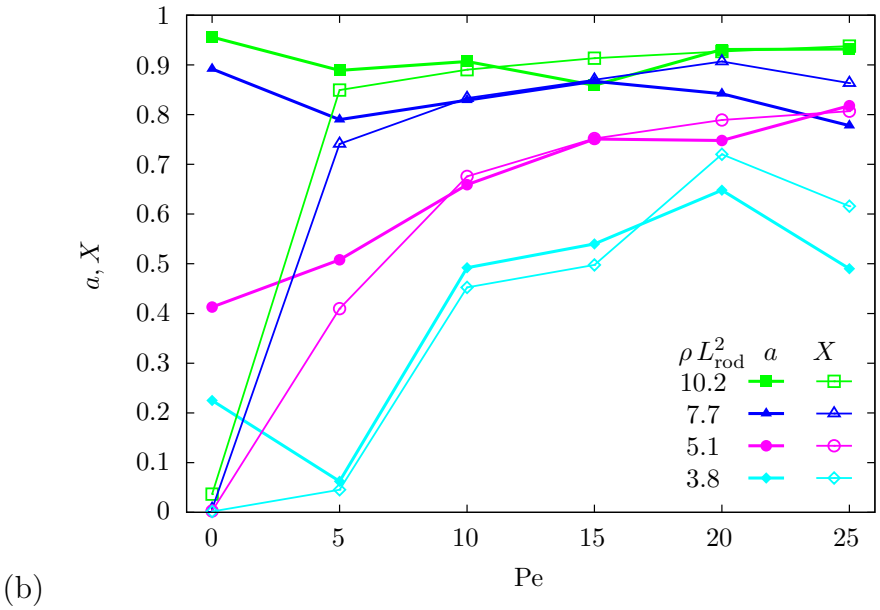

(b)

Figure 4.15: (a) Autocorrelation of rod orientation with lag time t for the systems shown in Fig. 1.15. Thick lines are simulation results; thin horizontal lines are autocorrelation base values, calculated by fitting the data with Eq. (4.11). (b) Comparison of the autocorrelation base value a and the fraction of rods in the largest cluster X. The observables have been calculated based on 200 frames in the last 40 000 time steps.

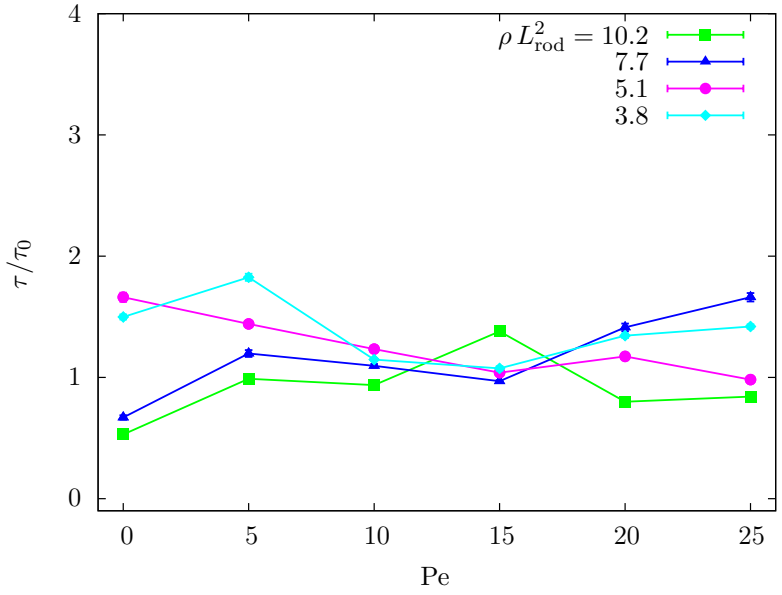

Figure 4.16: Autocorrelation time τ of the rod orientation as function of Pe for several average rod densities. $\tau_0 = 1/D_r$ is the time unit; see Chapter 2. The observables have been calculated based on 200 frames in the last 40 000 time steps.

Chapter 5

Polydisperse suspensions of active rods

We extend our investigations of the collective behavior in self-propelled rods by considering *bidisperse* suspensions that contain rods with two different lengths. By performing extensive Brownian dynamics simulations, we show that the density and the length of rods control the segregation and cluster formation of short and long rods.

We present background of the topic and explain the motivations to study bidisperse systems in Sec. 5.1, followed by a short review of the model in Sec. 5.2. In Sec. 5.3, we describe the different phases that we observe in our simulations, namely the isotropic phase, the induced clustering phase, the giant cluster phase, and the remixing phase. We analyze the simulation results in Sec. 5.4 by rod density distributions and by a segregation order parameter. We will show that the rod density distributions are qualitatively different for homogeneous, giant cluster, and remixed phases and show a unimodal, a bimodal, and a flat distribution, respectively. Using analytical arguments, we predict the formation of giant clusters with long rods and of giant clusters with long and short rods, as well as clustering of long rods induced by the presence of short rods.

5.1 Background and motivation

Self-propelled particles (SPPs) display an intriguing collective behavior, fundamentally different from passive particles, which has gained considerable attention in the recent years [29, 106]. In theoretical studies of self-propelled particles, two different types of interaction between particles can be employed: First, a Vicsek-like interaction, in which the collective behavior comes from an explicitly imposed interaction rule, i.e., alignment of neighboring particles. Second, a physical interaction, where the collective behavior results from a physical mechanism, e.g., short-ranged steric repulsion and/or long-ranged hydrodynamic interaction be-

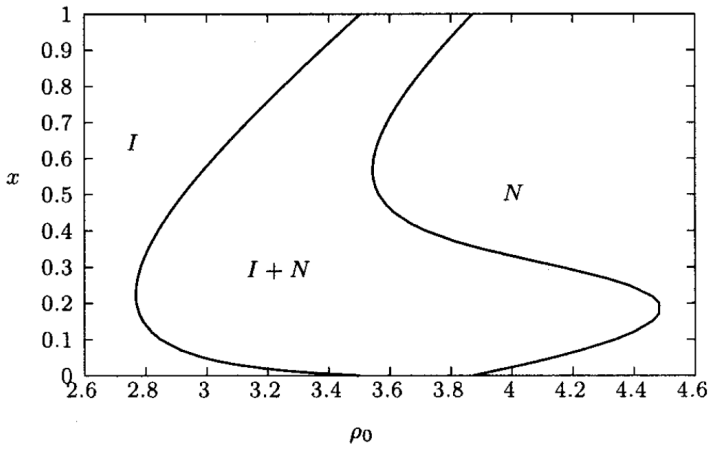

Figure 5.1: Phase diagram of a bidisperse system of passive rods. The length ratio between short and long rods is $q = 2.5$. x is the number fraction of the long rods, and ρ_0 is the dimensionless rod number density for both rod lengths. Lines show the limits of the I-N coexistence region, which are given by the isotropic (I) and the nematic (N) cloud curves. Figure is taken from Ref. [108].

tween the self-propelled particles. In the case of the physical interaction, both the nature of the interaction and the geometry of the particles (size, asymmetry, etc.) determine their collective behavior. In rodlike SPP systems (rSPPs), the alignment is due to the exchange of angular momentum between rods, and therefore, the collective behavior depends on the rod length. While the effect of rod length has been recently studied in monodisperse rSPPs without noise [62], little is known about clustering and segregation in rSPP systems with polydispersity, e.g., for systems that contain rods with different lengths. Polydisperse rSPP systems are found, for example, in mixtures of inherent (or mutated) polydisperse rodlike bacteria [20], or in motility assays of protein filaments [23, 107].

In passive systems, it is known that polydispersity has a number of effects. It has been shown theoretically [109, 110] and experimentally [78] that polydispersity broadens the coexistence region between isotropic and nematic states. A phase diagram of a passive bidisperse system of rods is presented in Fig. 5.1, which shows that the coexistence phase is narrower when the system consists of only the long or only the short rods, compared to the case of a mixed system. Furthermore, polydispersity causes fractionation, i.e., segregation of rods with different lengths in different phases of the coexistence [59]. Bidisperse (two-component) systems have been found to exhibit nematic-nematic (N-N) or isotropic-nematic-nematic (I-N-N) coexistence [79, 111, 112]. For the active case, to our knowledge geometrical polydispersity has not yet been studied so far. However, it is known that a mixture of active and passive rod-like particles (with the same length) segregates into clusters [63].

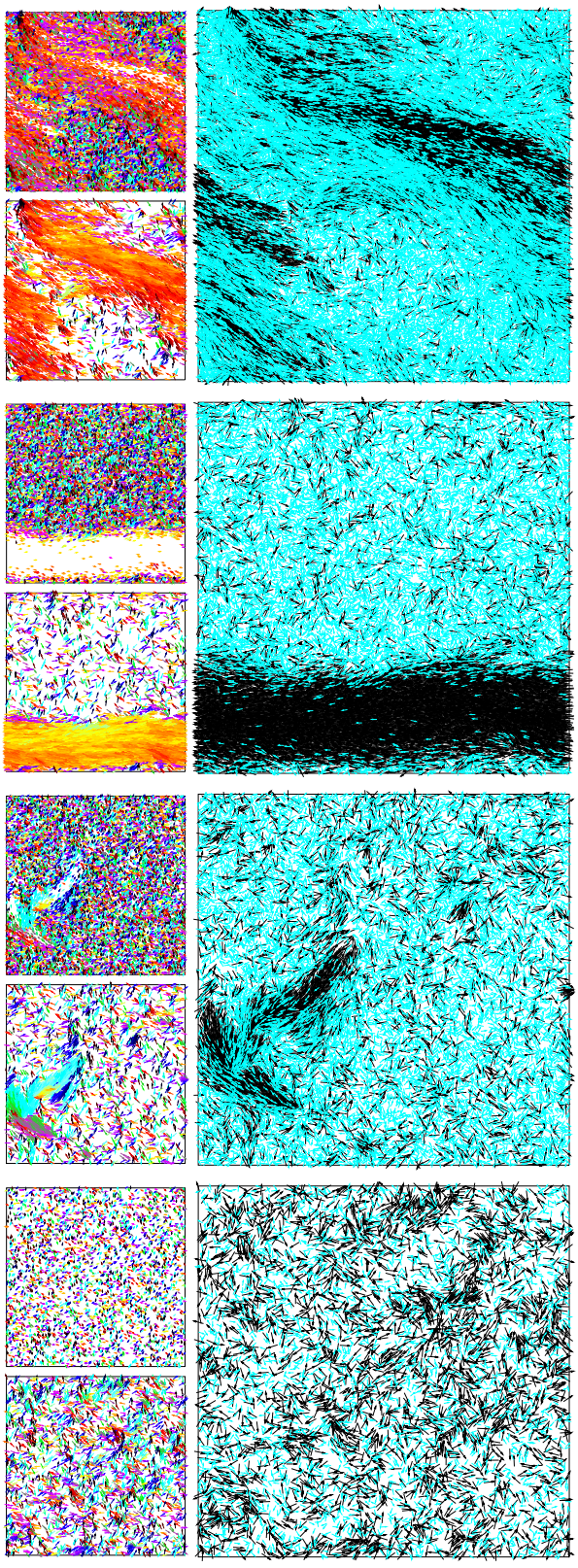

(a) $\rho_l L_l^2 = 2.6$, $\rho_s L_l^2 = 2.6$ (b) $\rho_l L_l^2 = 2.6$, $\rho_s L_l^2 = 7.7$ (c) $\rho_l L_l^2 = 5.1$, $\rho_s L_l^2 = 7.7$ (d) $\rho_l L_l^2 = 5.1$, $\rho_s L_l^2 = 15.3$

Figure 5.2: Snapshots of two-component active rod systems simulated using Brownian Dynamics with $L_s = L_l/2$. Rods in the larger squares are color-coded based on their length, long rods black and short rods light blue (gray). In the top small squares, only one type of rods are shown, long rods top left and short rods top right. Rods in the small squares are color-coded based on their orientation. (a) Isotropic phase for both rod types. (b) Giant clusters of long rods induced by the presence of short rods. (c) Giant clusters of long rods. (d) Remixed systems with aligned short and long rods.

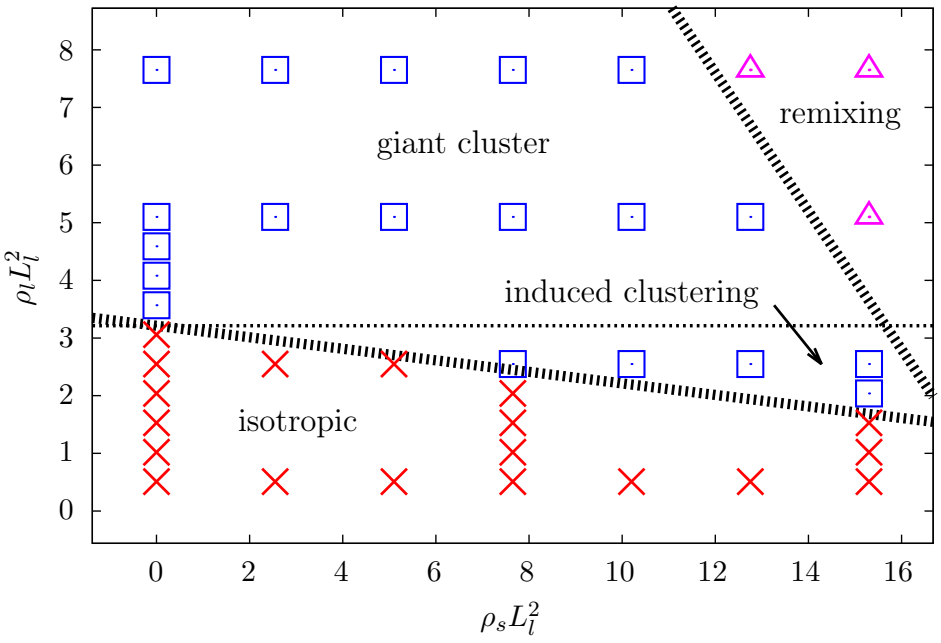

Figure 5.3: Phase diagram of two-component active rod systems for different densities of long (ρ_l) and short rods (ρ_s). Parameters are Péclet number Pe = 10, penetrability coefficient $Q = 0.37$, energy barrier $E = 1.5\,k_\mathrm{B}T$, and aspect ratios $a_l = 18$ for long and $a_s = 9$ for short rods. We observe an isotropic phase for both rod types (bottom left), a giant cluster of long rods in coexistence with a gas of short and long rods (top left), and a remixed phase where short rods penetrate into the cluster of long rods (top right). The thin dashed line indicates the long-rod density for which short rods induce the formation of a long-rod cluster. The phase boundary between the isotropic and the giant-cluster phase is given by Eq. (5.10). The phase boundary between the giant cluster and the remixed phase is a guide to the eye, where the slope is chosen to have a constant short-rod area fraction. For snapshots, see Fig. 5.2 and the Supplemental Material of Ref. [64].

In this chapter, we simulate bidisperse systems of rSPPs of long and short rods. The long rods have always the same length, while short rods of various lengths are considered. We find an isotropic phase, a giant cluster phase of the long rods only, and a remixed nematic phase; see Fig. 5.2. A phase diagram of the bidisperse system is shown in Fig. 5.3. More snapshots and movies can be found in the Supplemental Material of Ref. [64].

5.2 Model and simulation technique

We employ a penetrable rod model that was first introduced in Ref. [35], and also presented in Chapter 2. In addition to the position $\mathbf{r}$, orientation θ, velocity $\mathbf{v}$, and angular velocity ω, each rod is also characterized by its length L. We study bidisperse systems with rods of two different lengths, L_l and L_s. Because long and short rods have the same thickness, the aspect ratio is always proportional to the rod length L. We choose the propulsion force F_{rod} to be proportional to the rod length L. This choice is motivated by actin and microtubule motility assays, where the probability of the filament to be in proximity of a motor protein is proportional to its length; see also Sec. 7.4. Because the friction coefficient $\gamma_{\parallel,L}$ is also proportional to the rod length, the free-swimming velocity, $\mathbf{v}_{\mathrm{rod}} = F_{\mathrm{rod},L}/\gamma_{\parallel,L}\mathbf{e}_{\parallel}$, is independent of the rod length. Therefore, the dimensionless Péclet number

$$\mathrm{Pe} = \frac{v_{\mathrm{rod}}\, L}{D_{\parallel}} = \frac{\gamma_0 v_{\mathrm{rod}} L^2}{k_{\mathrm{B}}T}\,, \tag{5.1}$$

is different for short and long rods, where $D_{\parallel} = k_{\mathrm{B}}T/\gamma_{\parallel}$ is the diffusion coefficient parallel to the rod's axis. In our simulations, we use $\mathrm{Pe} = 10$ for long rods which implies $\mathrm{Pe} = 10 \times (L_s/L_l)^2$ for short rods. Our penetrable rods are also characterized by the dimensionless penetrability coefficient

$$Q = \frac{r_{\mathrm{min}} F_{\mathrm{rod}}}{E} \tag{5.2}$$

that we define as ratio of the propulsion force multiplied by the rod width and the energy barrier [1].

We measure lengths in units of the long rod length L_l. The size of the simulation box is $L_x \times L_y$, with $L_x = L_y = 36L_l$. The width of long and short rods is $r_{\mathrm{min}} = 0.056\, L_l$, so that our long rods have aspect ratio $a_l = 18$, whereas the aspect ratio of short rods varies between $2 \leq a_s \leq 16$. We define number densities of long/short rods as $\rho_{l,s} = N_{l,s}/L_xL_y$, where $N_{l,s}$ is the total number of long/short rods in the system, respectively. We study systems with density

[1] Note that Q here has a different definition from Q in Chapter 4. Here we use r_{min} instead of L as the length scale, so that Q becomes only proportional to F/E and not directly to L. The critical value $Q^* = 28$ that we obtained in Chapter 4 for cluster break-up of monodisperse rods corresponds to $Q^* = 28/18 = 1.6$ in the new definition.

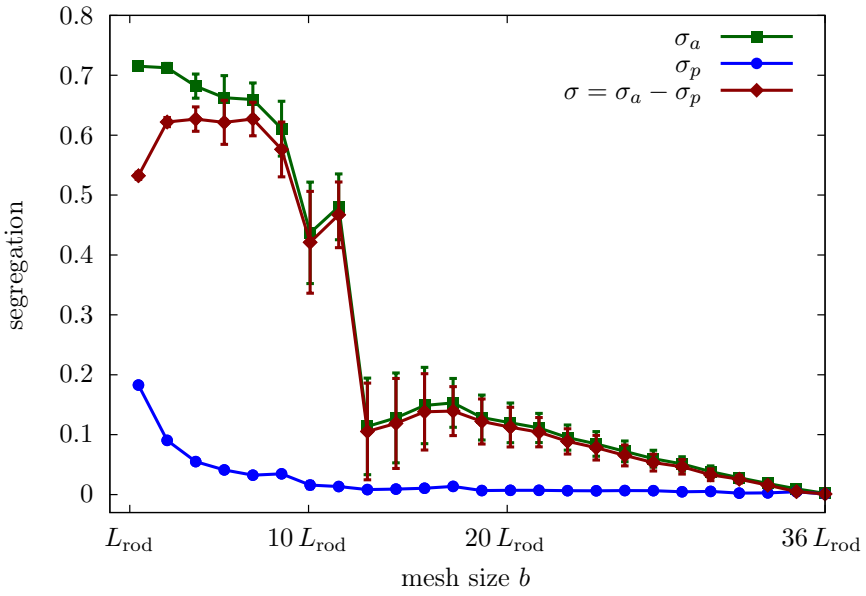

Figure 5.4: A sample segregation diagram, for the system shown in the snapshot of Fig. 5.2(c). The segregation order parameter σ is the maximum difference between the segregation of the active system σ_a and the segregation of an otherwise identical passive system σ_p; see Eq. (5.4).

of long rods in the range $2.6 < \rho_l L_l^2 < 7.6$ and that of short rods in the range $2.6 < \rho_s L_l^2 < 15.3$.

5.2.1 Segregation order parameter

We define the segregation order parameter as the following [63, 113]. We divide the simulation box into cells of side length b, and we define

$$\sigma(b) = \frac{1}{2\, f_a(1-f_a)} \sum_i \left(\frac{n_i}{n_{\rm tot}} \right) |f_i - f_a|, \tag{5.3}$$

where f_a is the average fraction of long rods in the system, n_i is the number of rods in the i-th cell, $n_{\rm tot}$ is the total number of rods in the system, and f_i is the fraction of long rods in the i-th cell. Complete segregation and no segregation correspond to $\sigma(b) = 1$ and $\sigma(b) = 0$, respectively. Note that $\sigma(b)$ strongly depends on the choice for the cell size b: for very small b, where the cell size is in the order of rod thickness, $\sigma(b)$ is very close to 1, and for very large b, where one cell covers the entire simulation box, $\sigma(b) = 0$. To define a segregation parameter which is independent of the cell size, we measure $\sigma(b)$ for various values of b for both the (active) system of interest, $\sigma_a(b)$, and a passive system with otherwise identical parameters, $\sigma_p(b)$; see Fig. 5.4. We measure the difference between $\sigma(b)$

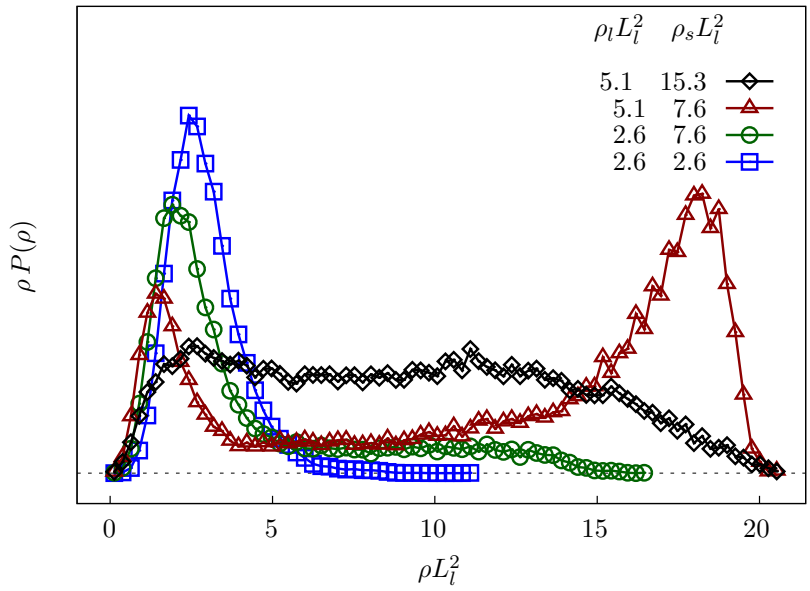

Figure 5.5: Density distributions of long rods for the systems shown in the snapshots of Fig. 5.2. For the system shown in Fig. 5.2(a), long rods have a normal distribution. For Fig. 5.2(b), the distribution has an extended tail towards higher densities. For Fig. 5.2(c), the distribution has two clear peaks, corresponding to the gas and the giant cluster. For Fig. 5.2(d), the distribution has a plateau that ranges from small to large densities.

for the active and the passive systems, $\sigma_{ap}(b) = \sigma_a(b) - \sigma_p(b)$, and report the maximum difference as the segregation order parameter of our systems, i.e.,

$$\sigma = \max\{\sigma_{ap}(b)\}. \tag{5.4}$$

5.3 Structure formation in bidisperse mixtures of rods

We first present simulations for bidisperse systems with $L_s = L_l/2$ and later for various short rod lengths. For fixed short rod length, we have systematically varied the densities of short and long rods. Figure. 5.2 shows typical simulation snapshots for the different phases. A phase diagram for the short and long rod densities is shown in Fig. 5.3. At low densities, $\rho_l L_l^2 = 5.1$ and $\rho_s L_l^2 = 7.6$, the system is in an isotropic and almost homogeneous phase for both short and long rods; see Fig. 5.2(a). Cluster formation is observed for higher rod densities; see Figs. 5.2(b)–5.2(d). More snapshots and movies can be found in the Supplemental Material [64].

In Fig. 5.5, typical density distributions for long rods are shown. We find

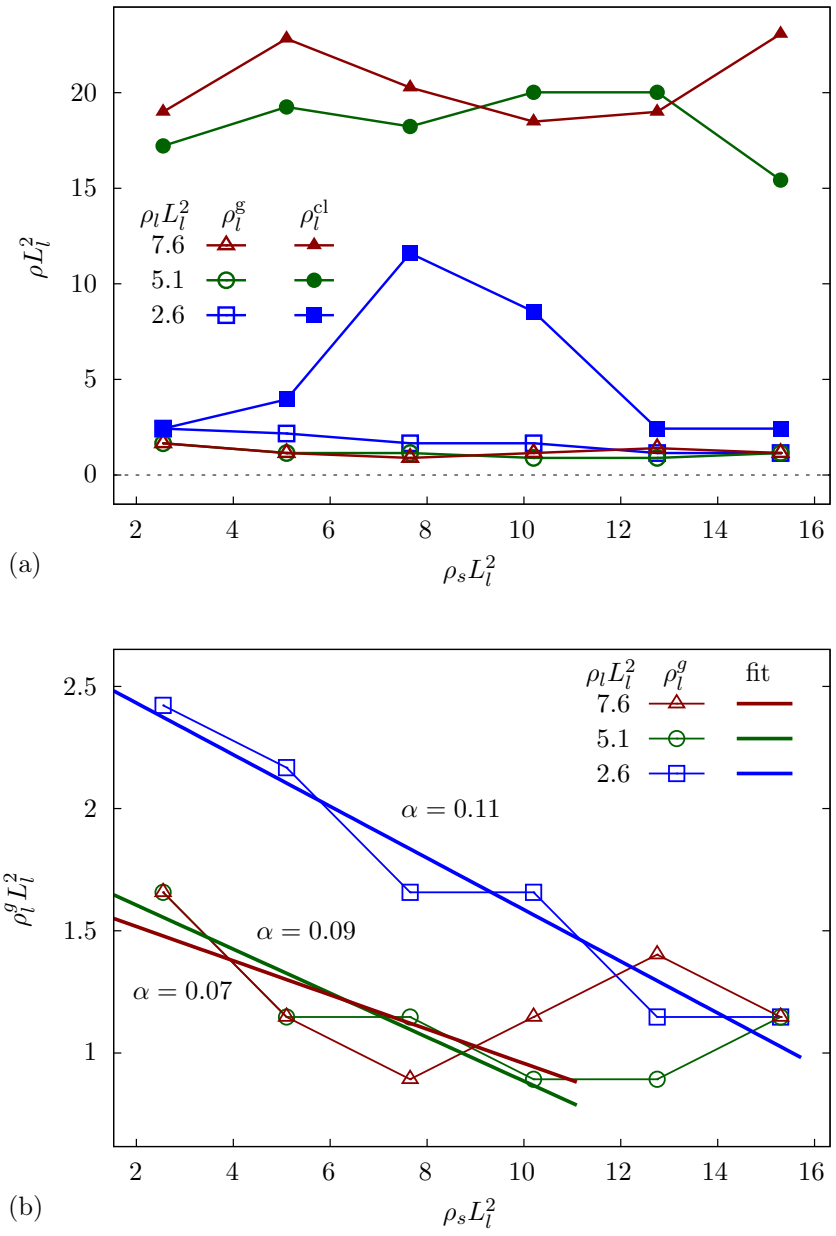

Figure 5.6: (a) Density of the peaks of lowest and highest density, ρ_l^1 and ρ_l^2,in the distribution of long rods, as a function of the average short rod density ρ_s, for various average long rod densities ρ_l. (b) Close-up of the density of the first peak ρ_l^1 (corresponding to the gas density), and a linear fit; see Eq. (5.10).

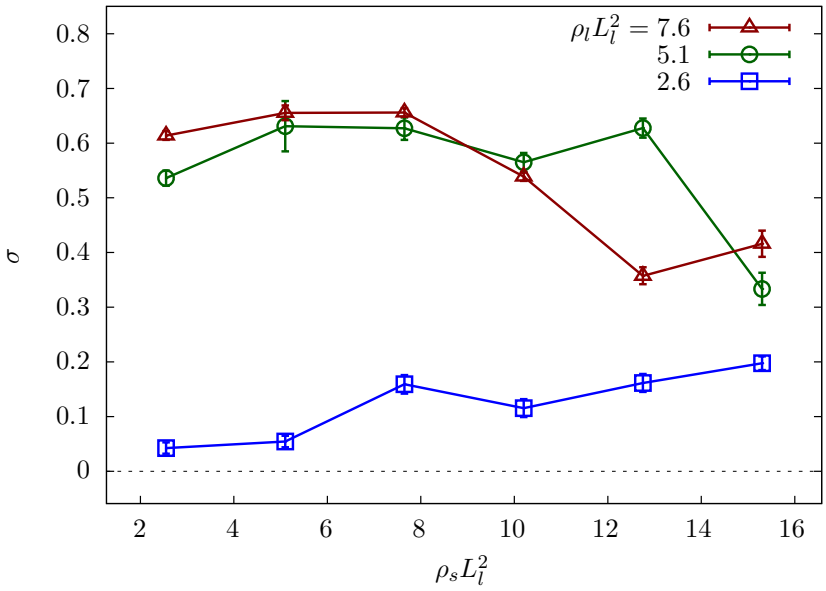

Figure 5.7: Segregation order parameter σ [Eq. (5.4)] for long and short rods as a function of short rod density ρ_s, for various average long rod densities ρ_l.

unimodal distributions for homogeneous systems as shown in Fig. 5.2(a), long tails for systems with induced clustering as shown in Fig. 5.2(b), bimodal distributions for segregated systems as shown in Fig. 5.2(c), and flat distributions for systems in the remixing phase as shown in Fig. 5.2(d). The peak densities are plotted in Fig. 5.6 [2] which shows that in general the density of the clusters, ρ_l^{cl}, does not change substantially with ρ_s and ρ_l.

An exception is the occurrence of "induced clustering" (as observed for $\rho_l L_l^2 = 2.6$) when the density of short rods is high enough to induce cluster formation for the long rods, but low enough such that the system is not in the remixed phase. The gas density of long rods ρ_l^g is plotted with higher resolution in Fig. 5.6(b). Excluding the points that are in the remixing phase, ρ_l^g decreases linearly with increasing short rod density.

We characterize the simulation data using the segregation order parameter σ used in Ref. [63]; see Sec. 5.2.1. As shown in Fig. 5.7, the segregation order parameter is small for $\rho_l L_l^2 = 2.6$ and high for $\rho_l L_l^2 = 5.1$ and $\rho_l L_l^2 = 7.6$. For $\rho_l L_l^2 = 2.6$, due to induced clustering σ increases with increasing short rod density. For $\rho_l L_l^2 = 5.1$ and $\rho_l L_l^2 = 7.6$, σ decreases at high short rod densities due to remixing.

In Fig. 5.8(a)–(c) simulation snapshots, density distributions,[3] peak positions,

[2] If the density distribution has more than two peaks, the positions of the highest and lowest density peaks are plotted.

[3] There is qualitative difference between cell density distributions $P(\rho)$ and rod density

and segregation order parameter are plotted for fixed volume fraction of all rods, fixed length of the long rods and various lengths of the short rods. Short and long rods form joint clusters above a threshold value for the short rod length. More snapshots and movies can be found in the Supplemental Material [64].

5.3.1 Induced clusters at low long-rod densities

For low densities of long rods and high densities of short rods, we observe the formation of a cluster that is composed almost exclusively of long rods. The cluster formation is induced by the presence of the short rods, because for the same ρ_l but lower ρ_s no such cluster is observed; compare Figs. 5.2(b) and 5.2(a). The density distribution of long rods shows an extended tail with a long plateau if an induced cluster is present [Fig. 5.5, green circles]. A high density peak is also visible at medium ρ_s in our peak analysis [Fig. 5.6(a), filled blue squares]. However, the high density peaks are not detected for higher ρ_s, though the long plateau exist. Because of remixing, the density of the peak position decreases again for increasing ρ_s. The "induced clustering" is also evident in the increase of the segregation order parameter shown in Fig. 5.7 (blue squares).

5.3.2 Giant clusters at high long-rod densities

For sufficiently high densities of long rods and not too high densities of short rods, we observe the formation of giant clusters similar to the clusters observed for monodisperse rod suspensions in Ref. [35]. In this region of the phase diagram, clusters are almost exclusively composed of long rods and coexist with a gas that is composed of both short and long rods; see e.g. the simulation snapshot in Fig. 5.2(c). The density distribution for the long rods shows a clear double-peak structure, where the low-density peak corresponds to the gas density and the high-density peak to the cluster density of the rods; see Fig. 5.5 (red rectangles). Long rods in the cluster are considerably denser than in the gas phase, and the density of the rods in the cluster does not substantially change for the entire range of short rod densities; see Fig. 5.6. As long as remixing does not occur, the gas density of long rods decreases linearly with increasing density of short rods. The segregation order parameter is high in the entire range of short rod densities; see Fig. 5.7.

5.3.3 Remixed rods at high short-rod densities

At high densities of short rods, $\rho_s L_l^2 > 12$, the short rods penetrate the giant clusters that are almost exclusively composed of long rods at low ρ_s. The short

distributions $\rho P(\rho)$; In this case, the former is unimodal, but the latter is bimodal. In Fig. 5.8 $P(\rho)$ is plotted, but in Fig. 5.5 $\rho P(\rho)$ is plotted.

rods that are part of the the giant cluster have the same orientation as the long rods. A simulation snapshot for such a remixed system is shown in Fig. 5.2(d). To ensure that remixing is independent of the initial distribution of rods, we have simulated this system both starting with an initially random distribution in space and orientation of all rods and also with initially phase-separated and perfectly parallel short and long rods.

In the remixed phase, the density distribution of the long rods is flat and spans the densities between the gas and the cluster density in the giant cluster phase; see Fig. 5.5 (black diamonds). Because of the lack of a clear peak in the density distribution, the gas density of the long rods does not follow any more the linear relationship that is observed for low ρ_s. The segregation order parameter shown in Fig. 5.7 that is about 0.6 for high ρ_l and low ρ_s drops to about 0.4 for remixed systems.

5.3.4 Length-dependent rod segregation in clusters

In Fig. 5.8, we show the dependence of the rod segregation σ on the length of the short rods L_s. We have simulated mixed rod systems with density $\rho_l L_l^2 = 5.1$ and aspect ratio $a_l = 18$ for the long rods, and various aspect ratios $2 \leq a_s \leq 16$ for the short rods. When we change a_s, we also change the density as $\rho_s \sim 9/a_s$ so that the total volume fraction is unchanged at the volume fraction of the system shown in the snapshot of Fig. 5.2(c). The simulation snapshots in Fig. 5.8(a)–(c) for $L_\mathrm{s} = 10$, $L_\mathrm{s} = 12$, and $L_\mathrm{s} = 14$ suggest that short rods penetrate the cluster when they are longer than a critical length. The density distributions for the short and long rods are shown below the simulation snapshots. The distributions are bimodal in all cases except for $L_\mathrm{s} = 12$. While for $L_\mathrm{s} = 10$ the larger peak for the short rod distribution corresponds to the gas density, the short-rod distribution is unimodal for $L_\mathrm{s} = 12$, and changes again for $L_\mathrm{s} = 14$ to a bimodal distribution where the larger peak corresponds to the cluster density.

The density of the short rods within the cluster of long rods increases, while the density of short rods in the surrounding of the cluster decreases with increasing short rod length; see Fig. 5.8(d). Fig. 5.8(e) shows an effective short-rod density and a theoretical gas density; the plot indicates the length at which the short rods penetrate the cluster of long rods. The segregation order parameter, shown in Fig. 5.8(f), decreases from $\sigma \approx 0.6$ to zero with increasing short rod length.

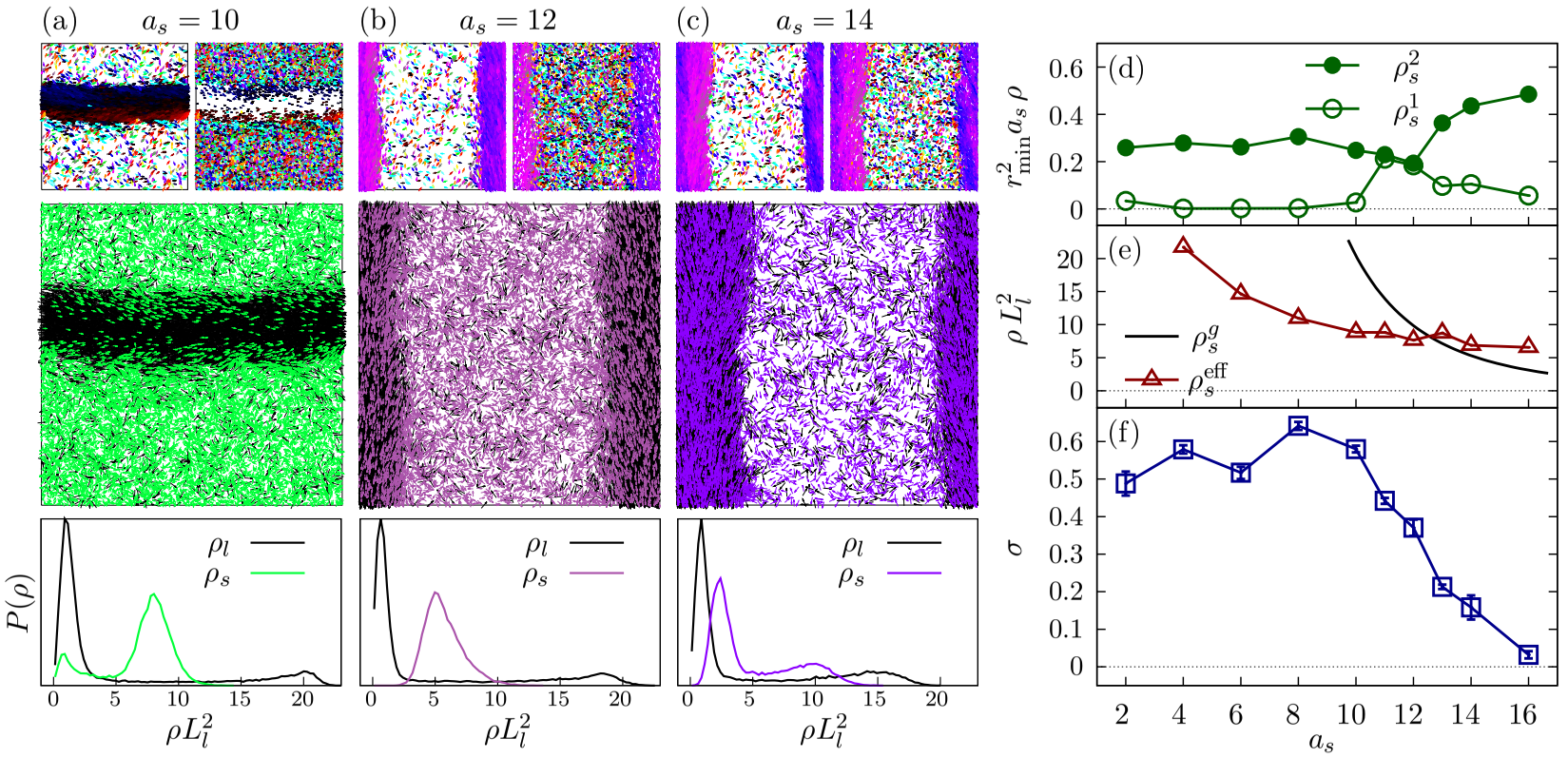

Figure 5.8: Simulation data and snapshots for two-component active rod systems with different short rod aspect ratios a_s. The aspect ratio of long rods is $a_l = 18$, and that of short rods varies in the range $2 \leq a_s \leq 16$. (a)–(c) Snapshots and density distributions of long and short rods for systems with $a_s = 10, 12$ and 14, respectively. For movies, see the Supplemental Material of Ref. [64]. The snapshots are plotted analogously to Fig. 5.2. The density distribution of short rods is unimodal for $a_s \approx 12$ and bimodal elsewhere; see (d). (d) Local volume fractions of the short rods, corresponding to the first ρ_s^1 and the last ρ_s^2 peak in the density distribution of short rods, as a function of a_s. The two peaks merge for $a_s \approx 12$, which indicates a phase transition. (e) Theoretical steady-state gas density for short rods ρ_s^g [Eq. (5.7)] and effective short rod density ρ_s^{eff} [Eq. (5.8)] as a function of a_s. We expect a clustering transition of short rods at the crossover of the two curves at $a_s \approx 12.5$. (f) Segregation order parameter σ [Eq. (5.4)] as function of the short rod aspect ratio a_s. See also Sec. 7.3.

5.4 Discussion

5.4.1 Rotational diffusion and cluster formation

In Sec. 4.2.1, we estimated the gas density of rods in equilibrium with a giant cluster for monodisperse rod suspensions. The argument is based on equating the rates for rods to attach to and detach from a giant cluster. While the rate of rods that attach to the cluster can be obtained from the rod density in the gas and their velocity, the rate of rods with length L that detach is proportional to the rod density at the cluster edge, $\rho_e = 1/L$, and the rod's rotational diffusion constant D_L^r. Using the Einstein relation $D_L^r = k_B T/\gamma_L^r$, the rotational diffusion constant is

$$D_L^r = \frac{6\, k_B T}{\gamma_0 L^3}\,. \tag{5.5}$$

As a result, the rotational diffusion D_s^r of short rods with length $L_s = L_l/2$ is related to that of long rods by

$$D_s^r = \left(\frac{L_l}{L_s}\right)^3 D_l^r = 8\, D_l^r\,. \tag{5.6}$$

Using the L-dependence of D^r [Eq. (5.5)] and Pe [Eq. (5.1)], we find that the density of a gas of rods that is in contact with a giant cluster is

$$\rho_L^g = \frac{192}{\pi^2 L^2}\frac{1}{\mathrm{Pe}} = \frac{192\, k_B T}{\pi^2\, \gamma_0 v_{\mathrm{rod}} L^4}\,; \tag{5.7}$$

see Sec. 4.2.1. We therefore hypothesize that rods form a giant cluster if the overall density of the rods in the system, ρ_L, is higher than the characteristic gas density, ρ_L^g, given by Eq. (5.7); see also Sec. 4.3. Long rods thus form clusters at considerably smaller densities than short rods. Temporarily formed cluster of rods below the characteristic gas density are unstable, because the flux of rods that join the cluster does not compensate the flux of rods that leave the cluster. We expect to find a homogeneous isotropic phase for $\rho_l < \rho_l^g$ and $\rho_s < \rho_s^g$, a segregated giant-cluster made of the long rods for $\rho_l > \rho_l^g$ and $\rho_s < \rho_s^g$, and a mixed giant-cluster made of both rods for $\rho_l > \rho_l^g$ and $\rho_s > \rho_s^g$.

The gas density of our long rods is $\rho_l^g L_l^2 = 1.95$ and that of short rods with $L_s = L_l/2$ is $\rho_s^g L_l^2 = 16\, \rho_l^g L_l^2 = 31.1$. We therefore expect to find the transition between the isotropic and the giant cluster phase for $\rho_l^g L_l^2 = 1.95$, but we observe the transition in the simulations only for a higher density, $\rho_l^{g,\mathrm{sim}} L_l^2 \approx 3.2$; see Fig. 4.10. This deviation is partially due to the approximative nature of the argument developed in this section, and partially due to our assumption that the gas is in coexistence with a giant cluster. Since we initialize our simulations with randomly distributed rods with random orientation, a nucleus is required for cluster formation. This is demonstrated in Fig. 5.3, where the gas density

for a simulation of long rods only is plotted as function of the overall density in the system. The measured gas density deviates from the overall density as expected at $\rho_l^g L_l^2 \approx 2$, but overshoots and drops to its steady-state density only for $\rho_l^g L_l^2 \approx 3.5$, in agreement with the occurrence of giant clusters in the phase diagram in Fig. 5.3.

We calculate the transition from giant clusters of long rods to mixed giant clusters for systems that correspond to the data in Fig. 5.8. Because part of the simulation box is filled with the long rods and is inaccessible to short rods, the effective density of short rods that determines the transition is larger than the overall density of short rods in the box $\rho_s = N_s/L_x L_y$. We assume homogeneous cluster and gas densities for the long rods. Using the conservation of the number of long rods $N_l = \rho_l^g A_l^g + \rho_l^c A_l^c$, and the decomposition of the total area $A = A_l^g + A_l^c$ in the area of the gas for the long rods A_l^g and the area of the cluster for the long rods A_l^c, the effective density is

$$\rho_s^{\text{eff}} = \frac{N_s}{A_l^g} = \frac{\rho_l^c - \rho_l^g}{\rho_l^c - \rho_l}\rho_s \,. \tag{5.8}$$

Here, ρ_l is the overall density of the long rods in the system, and the gas and the cluster density of the long rods, ρ_l^c, ρ_l^g, are extracted from the simulation data. The effective density is plotted in Fig. 5.8(e) together with the characteristic gas density calculated in Eq. (5.7). Indeed the short rods join the cluster of long rods when the effective gas density of short rods equals the theoretically estimated equilibrium gas density of short rods; see Fig. 5.8(c)[4].

Since the gas density also depends inversely on the Péclet number, another interesting test is to repeat the simulations that are shown in Fig. 5.8 with different Pe values, and check if the length of the short rods in which the mixing-demixing transition happens agrees with the corresponding analytical argument in Fig. 5.8(e). This case is discussed in Sec. 7.3.

5.4.2 Gas composition and induced clustering

For a gas of long rods in the presence of a giant cluster as shown in Fig. 5.2(c), the density of long rods in the gas ρ_l^g decreases with increasing density of short rods ρ_s^g, see Fig. 5.6(b). We assume that the presence of short rods decreases the rate for long rods to detach from the cluster and introduce an effective rate for long rods to detach from a giant cluster in the presence of the short rods, $J_l^{\text{det}}(\rho_l^g, \rho_s^g) = J_l^{\text{det}}(\rho_l^g, 0) - \alpha J_s^{\text{att}}(\rho_l^g, \rho_s^g)$, where $J_s^{\text{att}}(\rho_l^g, \rho_s^g)$ is the rate of short rods that attach to the cluster. A physical interpretation of this ansatz is that short rods constantly hit the boundary of the giant cluster and thus prevent long

[4]Note that the cluster of long rods forms a nucleus for the cluster of short rods, therefore clustering should occur directly without an overshoot in the short-rod density.

rods from detaching. For steady state, the effective detachment rate for long rods has to be equal to the attachment rate for long rods $J_l^{\mathrm{att}}(\rho_l^g, \rho_s^g)$,

$$J_l^{\mathrm{det}}(\rho_l^g, 0) - \alpha J_s^{\mathrm{att}}(\rho_l^g, \rho_s^g) = J_l^{\mathrm{att}}(\rho_l^g, \rho_s^g)\,. \tag{5.9}$$

We assume that the rates for the rods that attach to a giant cluster are independent of the presence of the other type of rods, $J_l^{\mathrm{att}}(\rho_l^g, \rho_s^g) = \rho_l^g v_l/4$ and $J_s^{\mathrm{att}}(\rho_l^g, \rho_s^g) = \rho_s^g v_s/4$. Using $J_l^{\mathrm{det}}(\rho_l^g, 0) = 8D_l^r/(\pi^2 L_l)$, we find for the characteristic gas density of the long rods

$$\rho_l^g(\rho_s) = \rho_l^g(0) - \alpha\rho_s\,, \tag{5.10}$$

which is valid for equal velocities of long and short rods, $v_{\mathrm{rod},l} = v_{\mathrm{rod},s}$, as used in our simulations. This generalizes Eq. (5.7) to mixtures of bidisperse self-propelled rods. We determine α phenomenologically from a fit of Eq. (5.10) to the gas density of long rods in systems with a giant cluster; see Fig. 5.6(b).

As discussed earlier, cluster formation is observed when the average rod density in the system is at least the characteristic gas density. This means that the cluster formation of long rods occurs for $\rho_l \geq \rho_l^g(\rho_s)$, where $\rho_l^g(\rho_s)$ is lowered according to Eq. (5.10) compared to $\rho_l^g(0)$ of a monodisperse system. Therefore, clustering in the bidisperse system is observed already for lower ρ_l than predicted for a monodisperse system. The presence of short rods therefore induces clustering of long rods, as described in section 5.3.1. Our prediction that is indicated by the bottom dashed line in Fig. 5.3 agrees well with the phases that we have observed in the simulations. Note that the α coefficient used to plot the thin dashed line in the phase diagram is not adjusted to match the induced clustering: We determine α by fitting the gas composition in systems that already have a giant cluster.

5.4.3 Remixing

At high short rod densities ρ_s, we observe remixing, i.e., short rods that enter a giant cluster of long rods even for low $a_s = 9$; see Fig. 5.2(d). Short rods within the cluster are oriented parallel to the long rods, while short rods outside the cluster are not aligned. Fig. 5.9 shows two simulation snapshots of systems with equal ρ_l and two different ρ_s. In the left snapshot with a lower ρ_s, a giant cluster of long rods coexists with a gas of short and long rods in a steady state. The right snapshot with a higher ρ_s is initialized from a perfectly segregated configuration, where both rod types were initially parallel to the phase boundary. The snapshot is for a time just before remixing sets in. For both snapshots, we measure the spatial distribution of interaction energy per bead for each rod. The energy profiles are shown in the middle row of Fig. 5.9. While for the low-density system the energy per bead is considerably smaller outside the cluster than within

the cluster, for the high density system the energies per bead inside and outside the cluster are comparable.

We explain the remixing in the following way. The density of the system shown in the snapshot of Fig. 5.9 (right) is very high (total volume fraction is $A_{\mathrm{tot}} = r_{\mathrm{min}}(\rho_l L_l + \rho_s L_s) = 0.71$). As a result, and also due to the high angular diffusion of short rods [Eq. (5.6)], the rods outside of the giant cluster are always intersecting with several other rods, which leads to very high interaction energies. Consequently, there is effectively no empty space in the gas, and the potential energy landscape in such a dense gas is relatively smooth. Therefore the rods in the gas don't have to overcome energy barriers to cross other rods, and effectively move in a nearly homogeneous potential landscape. A similar smooth potential landscape also exists in the giant cluster, where the long rods are in a close-packed arrangement. As a result, the short rods can freely diffuse to any region in the simulation box, even the region of the giant cluster, without considerable gain or loss of potential energy.

After initial penetration, high rod energies indicate collision-induced mixing in locations where a laterally-moving giant cluster "collects" short rods. and compare Ref. [63]. This is the reason for the higher rod energies to the right of the giant cluster in the high-density system shown in Fig. 5.9, because this cluster slowly moves to the right. The computational costs for simulations at high rod densities are high, therefore we do not determine the exact location of the phase boundary by simulations. However, we predict the slope of the phase boundary between the giant cluster and the remixed phase in Fig. 5.3 by assuming constant volume fraction of short rods in the system.

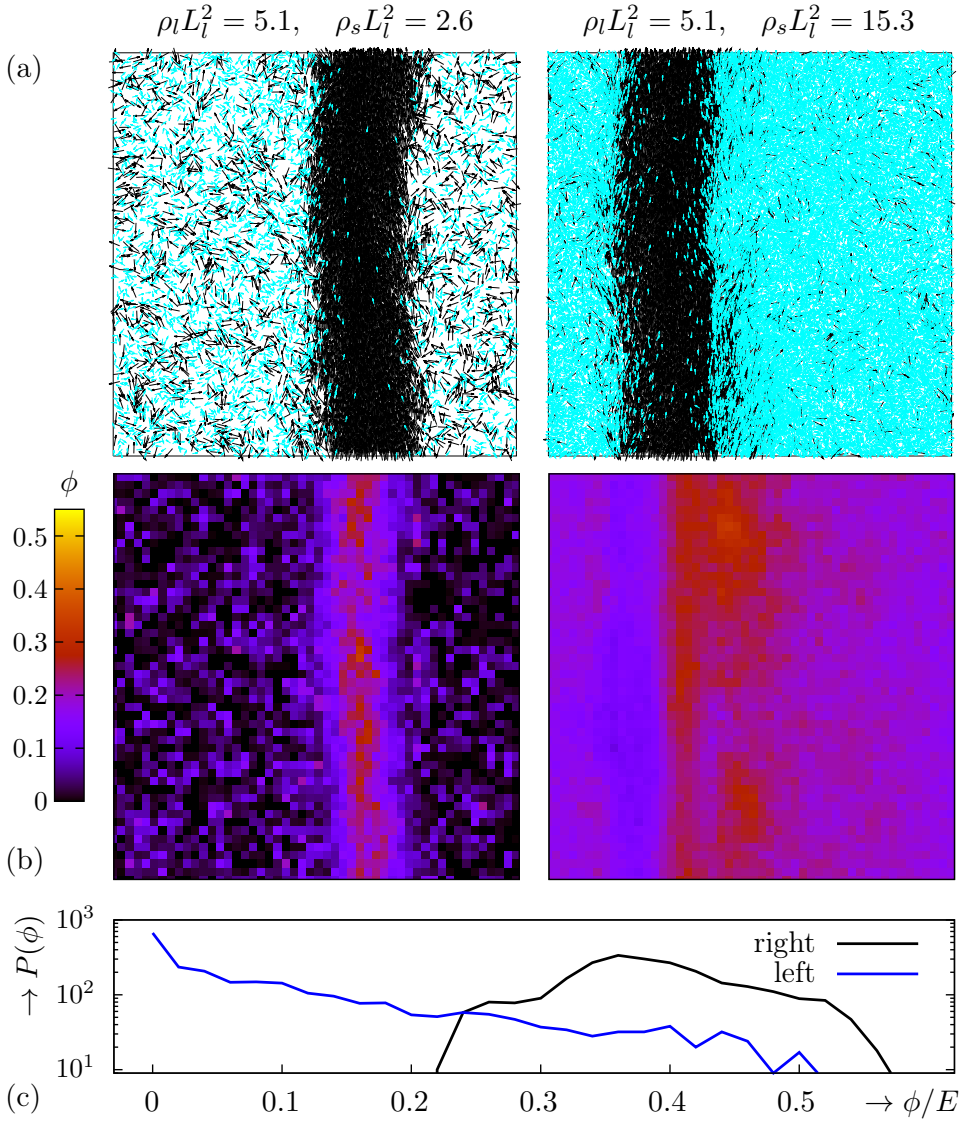

Figure 5.9: Simulation snapshots and rod energy distributions. Left: snapshot and spatial distribution of rod energy per bead in units of E for a system with a giant cluster of long rods at low short-rod density, $\rho_s L_l^2 = 2.6$. Right: system snapshot and spatial distribution of rod energy for $\rho_s L_l^2 = 15.3$. The system has been initialized with segregated and aligned rods, short and long rods will mix at later times of the simulation. Bottom: energy distribution of ϕ/E for $\rho_s L_l^2 = 2.6$ (blue) and $\rho_s L_l^2 = 15.3$ (black).

Chapter 6

Summary and Conclusions

We have studied collective behavior for self-propelled rigid rods in two dimensions constructed by single beads that interact with a separation-shifted Lennard Jones potential. The finite potential strength mimics the ability of microswimmers close to a wall and of filaments in motility assays to temporarily escape to the third dimension and cross each other. For a high potential barrier E, we recover the limit of impenetrable rods studied, for example, in Refs. [34, 62]. For most simulations, we have used an interaction energy $E = 1.5\,k_{\mathrm{B}}T$ that for complete overlap of two beads is of the order of the thermal energy; crossing of rods therefore occurs with a high probability; see Fig. 2.6. However, the interaction energy is much larger than the bead-bead interaction energy if rods cross at a small angle or if a single rod approaches a cluster. For our system with $n_{\mathrm{b}} = 18$ beads per rod, the energy for complete overlap is $n_b E = 27\,k_{\mathrm{B}}T$ and thus the probability for such events is very low.

6.1 Isotropic-nematic transition for passive rods

We have calculated a phase diagram for rod density and energy barrier to characterize the isotropic-nematic transition for passive rods. The isotropic-nematic transition is shifted to higher densities for reduced overlap energy, because of the reduced rod-rod interaction. We find significant deviations from the transition density calculated for hard rods [93, 114] if the bead-bead interaction energy is below $2\,k_{\mathrm{B}}T$. For $E = 1.5\,k_{\mathrm{B}}T$, the isotropic-nematic transition occurs for $\rho = 1.3\,\rho_c$, where ρ_c is the transition density for hard rods [93]. Our results using a modified Onsager theory show excellent agreement with our Monte Carlo simulations.

6.2 Crossing probability for protein filaments

Using Brownian dynamics simulations, we have determined the crossing probability for two colliding rods as function of their relative angles for several values of penetrability coefficient and Péclet number. The crossing probability is highest for almost perpendicular collisions, which is qualitatively similar to the crossing probability measured in experiments with microtubules propelled on surfaces. In Ref. [23], the maximum crossing probability for two microtubules in a motility assay is 40 % and corresponds to $Q = 5$ and $\mathrm{Pe} = 10$ in our simulations [1].

6.3 The clustering window

Self-propelled rods align due to their soft repulsive interaction [100]. For high rod densities, we find a laning phase. For intermediate rod densities and Péclet numbers, we observe the formation of giant clusters that span the entire simulation box, which we denote as "clustering window." Clusters break if the propulsion force is strong enough to overcome the repulsive force due to rod-rod interaction. We find a critical value $Q^* = 28$ for cluster break-up. We characterize our systems by cluster size distributions that can be fit by power-laws $\Pi(n) \propto n^{\beta}$ with $-1.5 \geq \beta \geq -3.5$, which is consistent with previous experimental and simulation results [20, 34]. By analyzing the autocorrelation function for rod orientation, we can separate the contributions from rods in a cluster from the contributions from free rods. We find that the free rods show almost the same orientational correlation as single rods.

6.4 The characteristic gas density

We can analytically estimate the density of free rods in systems with giant clusters, which we denote as "gas density," $\rho_{\mathrm{gas}} = 192/(\pi^2 L_{\mathrm{rod}}^2 \mathrm{Pe})$. The gas density is independent of the average rod density in the system, which is analogous to the molecule density in the gas phase for liquid-gas coexistence that does not depend on the volume of the liquid phase but only on temperature. Using $E_b = k_{\mathrm{B}}T \ln[192 r_{\mathrm{min}}/(\pi^2 L_{\mathrm{rod}}\mathrm{Pe})]$, we calculate effective binding energies for rods in the cluster. For aspect ratio 18 used in our simulations and $\mathrm{Pe} \approx 25$, we find effective binding energies of about $0.1\, k_{\mathrm{B}}T$, which is comparable to binding energies for the gas-liquid critical point for colloidal systems [103].

Phase separation into high-density and low-density regions is an intrinsic property of self-propelled particle systems and has also been observed for nonaligning spherical particles [45, 115–117]. As for the rods, the gas density of the spheres is inversely proportional to the propulsion velocity [45]. However, the nature of

[1] The same crossing probability may be achieved by increasing E and Pe at the same time.

cluster formation is different in the two models: While we observe motile clusters as a result of particle alignment, systems with nonaligning spheres exhibit jammed *non*motile clusters as a result of steric trapping. Moreover, the internal structure of clusters is nematic in our model, contrary to the isotropic structure for nonaligning spheres. Of course, also laning phases are only possible for anisotropic particles.

6.5 Bidisperse rod systems

We have studied bidisperse mixtures of self-propelled rods that in addition contain rods with shorter lengths. Short rods have the same free-swimming velocity as long rods, therefore their motion is characterized by smaller Péclet numbers compared with the motion of our long rods. We have simulated systems with different short rod lengths and densities and we find a phase where rods with both lengths are isotropic, a giant-cluster phase for the long rods, and a remixed phase where the short rods penetrate the cluster formed by long rods.

Addition of short rods into low-density suspensions of long rods induces clustering of long rods, whereas high densities of short rods in presence of a giant cluster of long rods leads to remixing and decreases the nematic order. This changes the rheological properties of the active systems for that already for monodisperse systems the activity leads to several new predictions compared with passive systems [118–120]. Geometric polydispersity has been found in bacteria and is naturally also expected in filament motility assays such as those presented in Refs. [20, 23, 30, 107]. Such effects of geometric polydispersity or a specific interaction that are employed in our simulations cannot be described using Vicsek models that otherwise are very successful to study swarm behavior. The mixed systems experience a rich phase behavior that is closely connected, but cannot be described alone by the intrinsic tendency of the rods to cluster. For specific aspects, our simulation data in combination with analytical arguments allows more quantitative predictions than the generic mechanism of collision frequency disparity discussed in Ref. [63].

The phase transition between the isotropic and the giant cluster phase of the long rods differs considerably from the passive phase transition between the isotropic and a nematic phase. We calculated the transition density for the phase transition for monodisperse passive rods. For long rods, we find $\rho_l^* L_l^2 = 3\pi/2/(1-\exp[-E/k_BT])$, which implies that the transition for short rods occurs for $\rho_s^* L_l^2 = 3\pi/2\,(L_l/L_s)^2/(1-\exp[-E/k_BT])$. For our systems, $\rho_c^l L_l^2 \approx 6$. Based on the transition density for long rods only and the gas densities of the long rods in mixed systems, we predict the transition density between the isotropic and the giant cluster phase for short rods to be $\rho_c^l L_l^2 \approx 24$. The phase transition for active long rods occurs already at lower densities than predicted for passive rods, while we predict the transition for active short rods for higher densities than for

passive short rods.

6.6 Remixing of short and long rods

For higher short rod densities that will finally lead to a remixed system, we find that the energy per rod in an initially demixed system is similar for short and long rods. Therefore, short rods can easily enter the cluster of long rods because their energy per bead in the isotropic phase of short rods is similar to the energy per bead in the cluster. For remixed systems, collision-induced remixing is also found, in particular at later stages of the simulation.

Remixing can be rationalized analogously to the screening of the excluded volume interaction in polymer solutions. The scaling of the size of linear polymers with their contour length depends on the density of the solution [121]: as soon as the polymer density is high enough, such that a monomer of a molecule interacts as frequently with monomers from other molecules as it interacts with its own monomers, the scaling between the radius of gyration of the polymer and the number of its monomers becomes identical to a hypothetical polymer without self-avoidance, $R_g \sim N^{0.5}$. In our case, remixing occurs as soon as the rods do not feel the difference between the phases. This argument allows to predict the slope of the phase boundary between the giant cluster and the remixed phase, which is given by constant volume fraction of short rods.

Chapter 7

Outlook

We have introduced and characterized a model of self-propelled rods that interact with a physical interaction that allows for crossing events. The model can now be used to interpret experiments for almost two-dimensional systems with good computational efficiency and allows predictions beyond those based on models using point particles with phenomenological alignment rules. The results presented in previous chapters form the basis for more detailed investigations and can be extended in several interesting directions. Some of these studies have already been initiated.

7.1 Comparison with experimental studies

Although qualitative agreement between models of self-propelled particles and experimental studies have been very promising [30,32], few studies could *quantitatively* connect theoretical and computational modeling with experiments [20,62]. We have characterized cluster formation in monodisperse and bidisperse suspensions of self-propelled rods in quasi-two dimensions. This work can be applied for example to experimental studies on the clustering of *Myxococcus xanthus* and *Escherichia coli*. Complementary to systems with variable motility [63], we have shown that bidisperse systems with different geometric and consequently different diffusive properties of self-propelled rods also lead to segregation without chemotaxis, signaling, and hydrodynamic interaction. Polydispersity is abundant in many biological and soft matter systems. Therefore, a systematic experimental study of polydisperse systems to test predictions based on the computer simulations appears to be feasible.

7.2 Phase diagram for bidisperse self-propelled rod systems

We have found a rich phenomenology for bidisperse suspensions of self-propelled rods in quasi-two dimensions for different densities and rod lengths. We currently present a phase diagram for different *densities* of short rods and long rods with double length (Fig. 5.3). For passive bidisperse systems, it is known that increasing the length difference between short and long rods amplifies segregation effects. A phase diagram for active rods with varying length ratios and total densities that can elucidate the effect of bidispersity more explicitly is desirable and within reach.

7.3 Effect of the overall activity on the mixing-demixing transition

In Sec. 5.3.4, we showed that changing the short rod length can induce a mixing-demixing transition between short and long rods, and we discussed in Sec. 5.4.1 that this transition can be explained by the characteristic gas density for each rod species. However, the activity in the system, i.e. the Péclet number, can also change the critical length of the short rods for mixing-demixing transition.

To test our quantitative prediction, we have run simulations with other Péclet numbers, i.e. where both rod types swim faster or slower compared to our simulations in Chapter 5. Some preliminary results are presented in the snapshots of Fig. 7.1, in which systems with three different Pe values (defined for the long rods) are shown. We expect theoretically that the transition for $\mathrm{Pe} = 5$ and $\mathrm{Pe} = 50$ happens near $a_s = 16$ and $a_s = 8$, respectively. Visual inspection of the snapshots in Fig. 7.1 reveals that indeed the critical length for the mixing-demixing transition has an inverse relation to the Péclet number. Quantitative comparison between theory and simulations is underway.

7.4 Bidispersity in swimming speed

Throughout Chapter 5, we assumed that the propulsion force F_{rod} of a rod is proportional to its length L_{rod}. This combined with the friction coefficient which is also proportional to the length, results in the same swimming speed for rods with different lengths, according to $v_{\mathrm{rod}} = F_{\mathrm{rod}}/\gamma_{\parallel}$. This choice for the dependence of F_{rod} on L_{rod} is justified for example in motility assays with protein filaments, since the propulsion force for the filaments comes from the number of molecular motors that they happen to be connected to, and this number is simply proportional to the filament length.

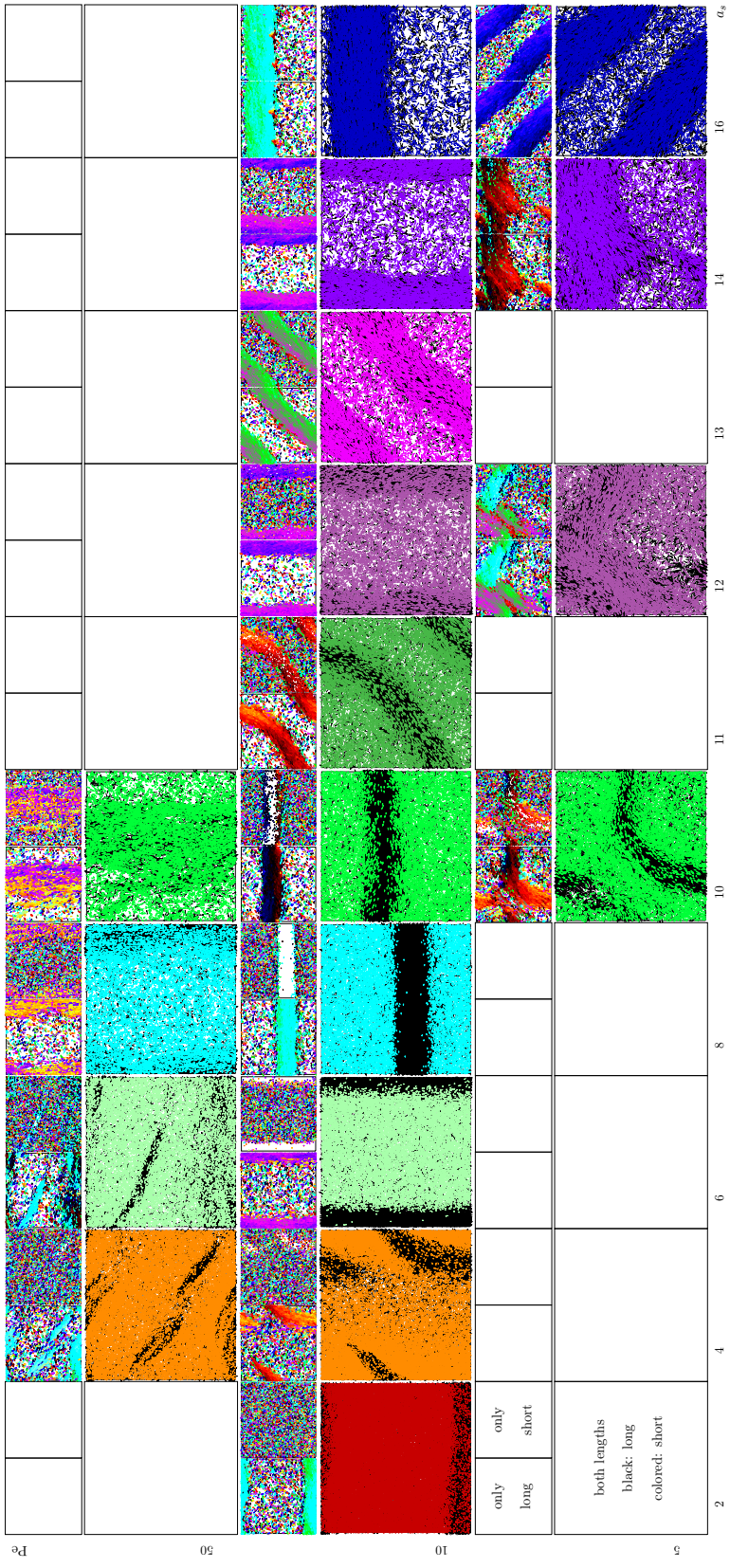

Figure 7.1: Simulation snapshots for two-component active rod systems with different Péclet numbers Pe and short rod aspect ratios a_s. The aspect ratio of long rods is $a_l = 18$, and that of short rods varies in the range $2 \leq a_s \leq 16$. For $\mathrm{Pe} = 50$, the mixing-demixing transition happens near $a_s \approx 4 \sim 8$. For $\mathrm{Pe} = 10$, it happens near $a_s \approx 12$; see also Fig. 5.8. For $\mathrm{Pe} = 5$, short and long rods are mixed in all of the shown snapshots.

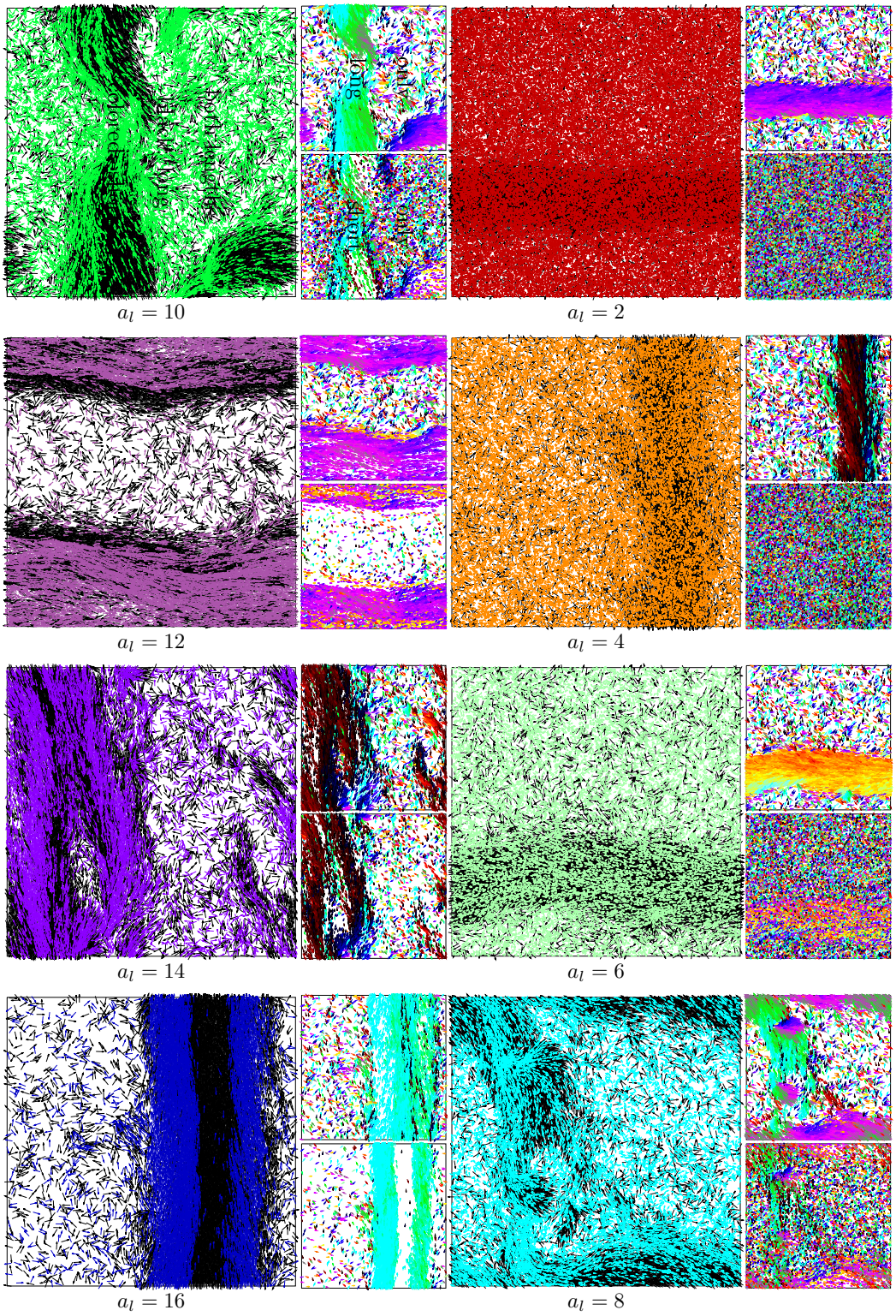

Figure 7.2: Snapshots of bidisperse active rod systems with different short rod aspect ratios a_s, where the free-swimming speed of the short rods inversely increases with their lenghts; see Sec. 7.4.

However, one can employ other possibilities for the dependence of F_{rod} on L_{rod}. For example, in bacterial locomotion with flagella, the swimming force is proportional to the number of flagella, but not directly on the body length. In this case, assuming the same number of flagella for long and short swimmers, leads to short swimmers to swim *faster* than the long ones, due to the smaller friction that they feel on their body.

We have also started to investigate this possibility in our simulations. Fig. 7.2 shows preliminary snapshots for the systems with different short rod lengths, where the propulsion force is the same for all rod species, and as a result, the swimming speed of the short rods inversely increases with their length. As visual inspection of the snapshots reveals, the segregation between the short and long rods is even more pronounced compared to the case of swimmers with the same speed (middle row in Fig. 7.1). This can be observed for example at high aspect ratio for short rods, where the length (and therefore the free-swimming speed) of short rods is very close to that of long rods. In this regime, although both of the rods participate in the formation of a giant cluster, short and long rods form segregated regions *within* the giant cluster. A systematic study of the collective behavior in such systems is underway.

7.5 Effect of noise on the cluster formation and segregation

We discussed shortly in Chapter 2 that the smoothness of the potential profile along a rod's axis (Fig. 2.5) affects the "friction" between rods, which in turn affects the collision scattering when two rods collide and move along each other. In fact, the friction alone has a drastic effect on the nature of cluster formation for self-propelled rods. For example, we think that the difference between the giant jammed clusters found in Ref. [34] [Fig. 1.12(c)] and the dynamic polar clusters that we presented in Chapter 4 [Fig. 1.15(c)] is mostly due to the difference in the rod "roughness" and consequently the rod-rod friction. The effect of this surface friction becomes very clear when we compare our results on self-propelled rods with the results of Vicsek-type models with nematic alignment rules—*point* particles that mimic rod-rod alignment interactions. While in our systems we observe *polar* worm-like clusters [e.g. Fig. 1.15(c)], in the Vicsek-type systems *nematic* worm-like clusters are found [Fig. 1.11(b)].

However, not only the potential profile, but also noise affects the rod-rod friction. Reduced noise causes the surface roughness of a rod to be more clearly felt during a collision. Therefore, we expect that a reduced noise makes the rods effectively less smooth, increases the surface fraction, and consequently, results in more jammed clusters.

Figure 7.3 shows snapshots of different bidisperse systems with various noise

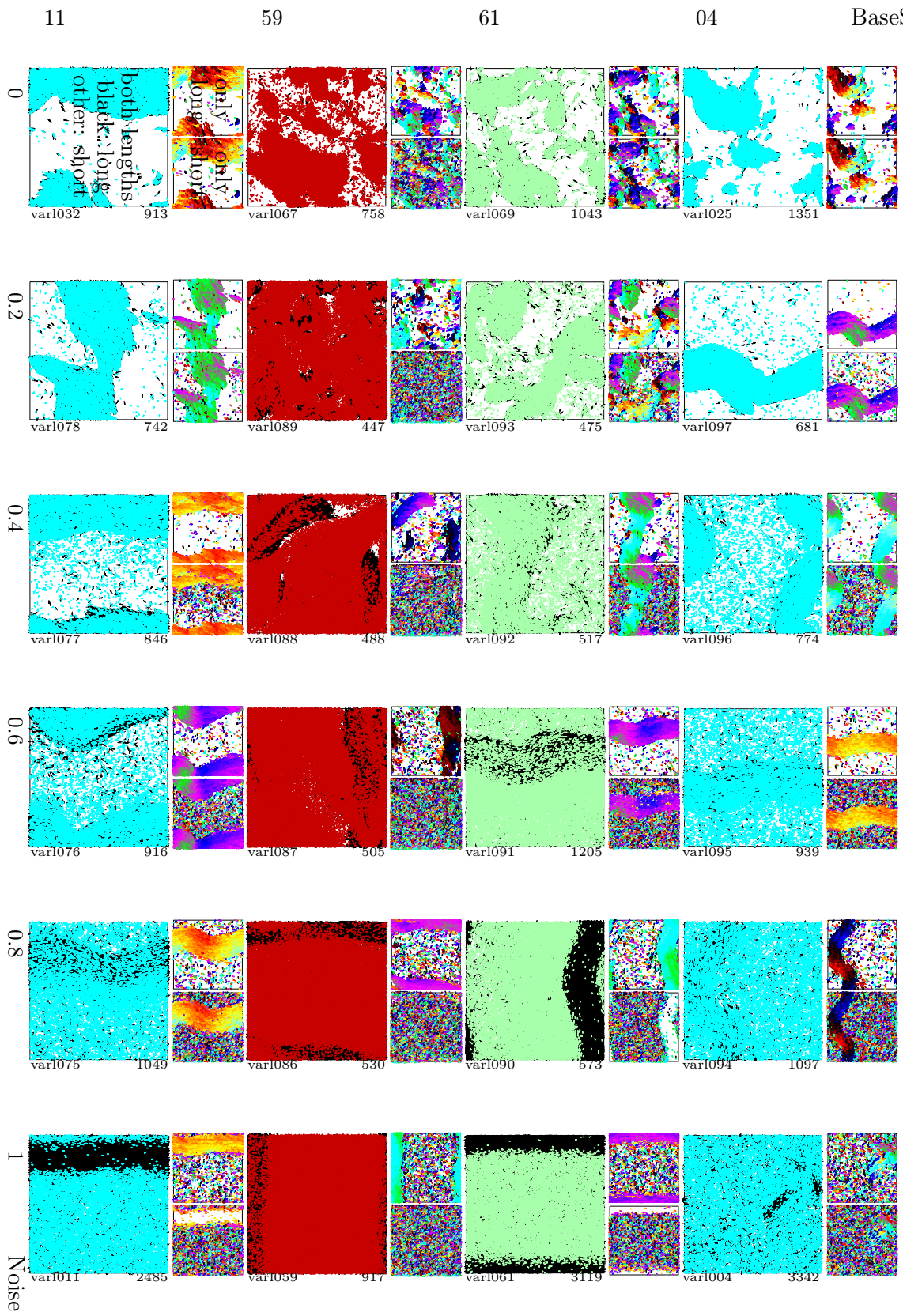

Figure 7.3: Collective behavior of bidisperse systems with varying noise. Each row shows systems with a fixed density and aspect ratio for short and long rods, but with varying noise.

values. The highest noise level in the snapshots corresponds to the noise that we have implemented for rods throughout this thesis. Visual inspection of the snapshots reveals that a reduced noise affects cluster shapes, and sometimes results in jammed nonmotile clusters. Moreover, reducing the noise results in a reduction in the segregation of otherwise highly segregated systems; compare the snapshots in the very left and the very right of each row. We have started to study these effects in more detail.

7.6 Polydispersity

In addition to bidisperse (two-component) systems, an interesting case for self-propelled rods is polydisperse (*multi*-component) systems, where the rods have a continuous distribution of lengths. Polydispersity is to some extent inevitable in most experimental studies of bacteria [20] and protein filaments [107].

We have simulated polydisperse systems where the aspect-ratio of the swimmers are drawn from a Gaussian distribution with the peak value $\langle a \rangle$ and the spread σ_a. Fig. 7.4 shows the snapshots of systems with $\langle a \rangle = 18$ and several σ_a values. A slight fractionation is evident from visual inspection of the snapshots, and the effect is more pronounced as σ_a increases. A systematic study of polydisperse suspensions both with respect to the cluster formation dynamics and the steady state results in a deeper insight into the collective behavior in many intrinsically polydisperse systems.

Figure 7.4: Snapshot of polydisperse systems with different spread in the aspect ratio of rods σ_a. The peak aspect ratio is on $\langle a \rangle = 18$. In the small upper squares in the left (right) of each snapshot, only rods with $a > \langle a \rangle$ ($a < \langle a \rangle$) are shown.

Bibliography

[1] Electron microscopy unit snow page, https://web.archive.org/web/20140331122248/http://emu.arsusda.gov/snowsite/, United States Department of Agriculture, Accessed: 2014-04-28.

[2] E. Ben-Jacob et al., *Generic modelling of cooperative growth patterns in bacterial colonies*, Nature **368**, 46 (1994).

[3] School of big eye scad, https://commons.wikimedia.org/wiki/File:School_of_big_eye_scad.jpg, Wikimedia Commons, Accessed: 2014-04-28.

[4] M. Moussaïd et al., *Experimental study of the behavioural mechanisms underlying self-organization in human crowds*, Proc. R. Soc. London, Ser. B **276**, 2755 (2009).

[5] Image ID: nssl0062, https://web.archive.org/web/20131203051515/http://www.photolib.noaa.gov/htmls/nssl0062.htm, NOAA's National Severe Storms Laboratory, Accessed: 2014-04-28.

[6] C. Brennen and H. Winet, *Fluid mechanics of propulsion by cilia and flagella*, Annu. Rev. Fluid Mech. **9**, 339 (1977).

[7] H. C. Berg, *E. coli in Motion*, Springer, 2004.

[8] H. C. Berg, *The rotary motor of bacterial flagella*, Biochemistry **72**, 19 (2003).

[9] N. C. Darnton, L. Turner, S. Rojevsky, and H. C. Berg, *On torque and tumbling in swimming Escherichia coli*, J. Bacteriol. **189**, 1756 (2007).

[10] Simplified spermatozoon diagram, https://commons.wikimedia.org/wiki/File:Simplified_spermatozoon_diagram.svg, Wikimedia Commons, Accessed: 2014-05-02.

[11] W. F. Paxton et al., *Catalytic nanomotors: Autonomous movement of striped nanorods*, J. Am. Chem. Soc. **126**, 13424 (2004).

[12] V. Magdanz, S. Sanchez, and O. G. Schmidt, *Development of a Sperm-Flagella Driven Micro-Bio-Robot*, Adv. Mater. **25**, 6581 (2013).

[13] How do you control a spermbot? Try a magnetic field, http://youtu.be/MP-Z7CRfGkQ, New Scientist, Accessed: 2014-05-02.

[14] E. M. Purcell, *Life at low Reynolds number*, Am. J. Phys **45**, 3 (1977).

[15] J. K. Parrish and W. M. Hamner, *Animal groups in three dimensions: how species aggregate*, Cambridge University Press, 1997.

[16] I. H. Riedel, K. Kruse, and J. Howard, *A Self-Organized Vortex Array of Hydrodynamically Entrained Sperm Cells*, Science **309**, 300 (2005).

[17] Y. Yang, J. Elgeti, and G. Gompper, *Cooperation of sperm in two dimensions: Synchronization, attraction, and aggregation through hydrodynamic interactions*, Phys. Rev. E **78**, 061903 (2008).

[18] E. Ben-Jacob, I. Cohen, and H. Levine, *Cooperative self-organization of microorganisms*, Adv. Phys. **49**, 395 (2000).

[19] A. Sokolov, I. S. Aranson, J. O. Kessler, and R. E. Goldstein, *Concentration Dependence of the Collective Dynamics of Swimming Bacteria*, Phys. Rev. Lett. **98**, 158102 (2007).

[20] F. Peruani et al., *Collective Motion and Nonequilibrium Cluster Formation in Colonies of Gliding Bacteria*, Phys. Rev. Lett. **108**, 098102 (2012).

[21] J. Gachelin et al., *Non-Newtonian Viscosity of Escherichia coli Suspensions*, Phys. Rev. Lett. **110**, 268103 (2013).

[22] V. Schaller, C. Weber, C. Semmrich, E. Frey, and A. R. Bausch, *Polar patterns of driven filaments*, Nature (London) **467**, 73 (2010).

[23] Y. Sumino et al., *Large-scale vortex lattice emerging from collectively moving microtubules*, Nature (London) **483**, 448 (2012).

[24] G. Volpe, I. Buttinoni, D. Vogt, H.-J. Kummerer, and C. Bechinger, *Microswimmers in patterned environments*, Soft Matter **7**, 8810 (2011).

[25] Y. Mei, A. A. Solovev, S. Sanchez, and O. G. Schmidt, *Rolled-up nanotech on polymers: from basic perception to self-propelled catalytic microengines*, Chem. Soc. Rev. **40**, 2109 (2011).

[26] S. Ebbens, M.-H. Tu, J. R. Howse, and R. Golestanian, *Size dependence of the propulsion velocity for catalytic Janus-sphere swimmers*, Phys. Rev. E **85**, 020401 (2012).

[27] M. Yang and M. Ripoll, *Simulations of thermophoretic nanoswimmers*, Phys. Rev. E **84**, 061401 (2011).

[28] A. Cavagna et al., *Scale-free correlations in starling flocks*, Proc. Natl. Acad. Sci. U.S.A. **107**, 11865 (2010).

[29] T. Vicsek and A. Zafeiris, *Collective motion*, Phys. Rep. **517**, 71 (2012).

[30] C. W. Harvey, M. Alber, L. S. Tsimring, and I. S. Aranson, *Continuum modeling of myxobacteria clustering*, New J. Phys. **15**, 035029 (2013).

[31] C. Huepe and M. Aldana, *Intermittency and Clustering in a System of Self-Driven Particles*, Phys. Rev. Lett. **92**, 168701 (2004).

[32] F. Peruani, A. Deutsch, and M. Bär, *Nonequilibrium clustering of self-propelled rods*, Phys. Rev. E **74**, 030904 (2006).

[33] C. Huepe and M. Aldana, *New tools for characterizing swarming systems: a comparison of minimal models*, Phys. A (Amsterdam, Neth.) **387**, 2809 (2008).

[34] Y. Yang, V. Marceau, and G. Gompper, *Swarm behavior of self-propelled rods and swimming flagella*, Phys. Rev. E **82**, 031904 (2010).

[35] M. Abkenar, K. Marx, T. Auth, and G. Gompper, *Collective behavior of penetrable self-propelled rods in two dimensions*, Phys. Rev. E **88**, 062314 (2013).

[36] T. Vicsek, A. Czirók, E. Ben-Jacob, I. Cohen, and O. Shochet, *Novel Type of Phase Transition in a System of Self-Driven Particles*, Phys. Rev. Lett. **75**, 1226 (1995).

[37] G. Grégoire and H. Chaté, *Onset of Collective and Cohesive Motion*, Phys. Rev. Lett. **92**, 025702 (2004).

[38] J. Toner and Y. Tu, *Long-Range Order in a Two-Dimensional Dynamical* XY *Model: How Birds Fly Together*, Phys. Rev. Lett. **75**, 4326 (1995).

[39] R. Aditi Simha and S. Ramaswamy, *Hydrodynamic Fluctuations and Instabilities in Ordered Suspensions of Self-Propelled Particles*, Phys. Rev. Lett. **89**, 058101 (2002).

[40] S. Ramaswamy, R. A. Simha, and J. Toner, *Active nematics on a substrate: Giant number fluctuations and long-time tails*, Europhys. Lett. **62**, 196 (2003).

[41] J. Toner, Y. Tu, and S. Ramaswamy, *Hydrodynamics and phases of flocks*, Ann. Phys. **318**, 170 (2005).

[42] F. Peruani, A. Deutsch, and M. Bär, *A mean-field theory for self-propelled particles interacting by velocity alignment mechanisms*, Eur. Phys. J. Special Topics **157**, 111 (2008).

[43] E. Bertin, M. Droz, and G. Grégoire, *Hydrodynamic equations for self-propelled particles: microscopic derivation and stability analysis*, J. Phys. A: Math. Theor. **42**, 445001 (2009).

[44] R. Golestanian, *Anomalous Diffusion of Symmetric and Asymmetric Active Colloids*, Phys. Rev. Lett. **102**, 188305 (2009).

[45] G. S. Redner, M. F. Hagan, and A. Baskaran, *Structure and Dynamics of a Phase-Separating Active Colloidal Fluid*, Phys. Rev. Lett. **110**, 055701 (2013).

[46] B. Szabó et al., *Phase transition in the collective migration of tissue cells: Experiment and model*, Phys. Rev. E **74**, 061908 (2006).

[47] M. R. D'Orsogna, Y. L. Chuang, A. L. Bertozzi, and L. S. Chayes, *Self-Propelled Particles with Soft-Core Interactions: Patterns, Stability, and Collapse*, Phys. Rev. Lett. **96**, 104302 (2006).

[48] M. Aldana, V. Dossetti, C. Huepe, V. M. Kenkre, and H. Larralde, *Phase Transitions in Systems of Self-Propelled Agents and Related Network Models*, Phys. Rev. Lett. **98**, 095702 (2007).

[49] H. Chaté, F. Ginelli, G. Grégoire, and F. Raynaud, *Collective motion of self-propelled particles interacting without cohesion*, Phys. Rev. E **77**, 046113 (2008).

[50] F. Ginelli, F. Peruani, M. Bär, and H. Chaté, *Large-Scale Collective Properties of Self-Propelled Rods*, Phys. Rev. Lett. **104**, 184502 (2010).

[51] J. Stenhammar, A. Tiribocchi, R. J. Allen, D. Marenduzzo, and M. E. Cates, *Continuum Theory of Phase Separation Kinetics for Active Brownian Particles*, Phys. Rev. Lett. **111**, 145702 (2013).

[52] Y. Fily, S. Henkes, and M. C. Marchetti, *Freezing and phase separation of self-propelled disks*, Soft Matter **10**, 2132 (2014).

[53] H. Chaté, F. Ginelli, G. Grégoire, F. Peruani, and F. Raynaud, *Modeling collective motion: variations on the Vicsek model*, Eur. Phys. J. B **64**, 451 (2008).

[54] G. Grégoire, H. Chaté, and Y. Tu, *Moving and staying together without a leader*, Physica D **181**, 157 (2003).

[55] J.-B. Caussin et al., *Emergent Spatial Structures in Flocking Models: A Dynamical System Insight*, Phys. Rev. Lett. **112**, 148102 (2014).

[56] D. Kaiser, *Coupling cell movement to multicellular development in myxobacteria*, Nat. Rev. Microbiol. **1**, 45 (2003).

[57] K. Drescher, J. Dunkel, L. H. Cisneros, S. Ganguly, and R. E. Goldstein, *Fluid dynamics and noise in bacterial cell–cell and cell–surface scattering*, Proc. Natl. Acad. Sci. U.S.A. **108**, 10940 (2011).

[58] P. Kraikivski, R. Lipowsky, and J. Kierfeld, *Enhanced Ordering of Interacting Filaments by Molecular Motors*, Phys. Rev. Lett. **96**, 258103 (2006).

[59] L. Onsager, *The Effects of Shape on the Interaction of Colloidal Particles*, Ann. N.Y. Acad. Sci. **51**, 627 (1949).

[60] A. Baskaran and M. C. Marchetti, *Enhanced Diffusion and Ordering of Self-Propelled Rods*, Phys. Rev. Lett. **101**, 268101 (2008).

[61] D. Saintillan and M. J. Shelley, *Orientational order and instabilities in suspensions of self-locomoting rods*, Phys. Rev. Lett. **99**, 58102 (2007).

[62] H. H. Wensink et al., *Meso-scale turbulence in living fluids*, Proc. Natl. Acad. Sci. U.S.A. **109**, 14308 (2012).

[63] S. R. McCandlish, A. Baskaran, and M. F. Hagan, *Spontaneous segregation of self-propelled particles with different motilities*, Soft Matter **8**, 2527 (2012).

[64] M. Abkenar, P. Roelli, K. Marx, T. Auth, and G. Gompper, *Phase behavior of mixtures of rodlike microswimmers with length bidispersity*, in preparation (2015).

[65] F. Ruhnow, D. Zwicker, and S. Diez, *Tracking Single Particles and Elongated Filaments with Nanometer Precision*, Biophys. J. **100**, 2820 (2011).

[66] M. Doi, *The theory of polymer dynamics*, Oxford University Press, 1988.

[67] J. Gray and G. J. Hancock, *The Propulsion of Sea-Urchin Spermatozoa*, J. Exp. Biol **32**, 802 (1955).

[68] C. Wolgemuth, E. Hoiczyk, D. Kaiser, and G. Oster, *How myxobacteria glide*, Curr. Biol. **12**, 369 (2002).

[69] A. P. Berke, L. Turner, H. C. Berg, and E. Lauga, *Hydrodynamic attraction of swimming microorganisms by surfaces*, Phys. Rev. Lett. **101**, 038102 (2008).

[70] J. Elgeti and G. Gompper, *Self-propelled rods near surfaces*, EPL **85**, 38002 (2009).

[71] J. Elgeti, U. B. Kaupp, and G. Gompper, *Hydrodynamics of sperm cells near surfaces*, Biophys. J. **99**, 1018 (2010).

[72] J. Elgeti and G. Gompper, *Wall accumulation of self-propelled spheres*, EPL **101**, 48003 (2013).

[73] J. E. Jones, *On the Determination of Molecular Fields. II. From the Equation of State of a Gas*, Proc. R. Soc. London, Ser. A **106**, 463 (1924).

[74] J. D. Weeks, D. Chandler, and H. C. Andersen, *Role of Repulsive Forces in Determining the Equilibrium Structure of Simple Liquids*, J. Chem. Phys **54**, 5237 (1971).

[75] M. E. Fisher and D. Ruelle, *The Stability of Many-Particle Systems*, J. Math. Phys. **7**, 260 (1966).

[76] H. Zocher, *Über freiwillige Strukturbildung in Solen. (Eine neue Art anisotrop flüssiger Medien.)*, Z. Anorg. Allg. Chem. **147**, 91 (1925).

[77] G. Oster, *Two-phase formation in solutions of tobacco mosaic virus and the problem of long-range forces*, J. Gen. Physiol. **33**, 445 (1950).

[78] M. P. B. van Bruggen, F. M. van der Kooij, and H. N. W. Lekkerkerker, *Liquid crystal phase transitions in dispersions of rod-like colloidal particles*, J. Phys. Condens. Matter **8**, 9451 (1996).

[79] P. A. Buining and H. N. W. Lekkerkerker, *Isotropic-nematic phase separation of a dispersion of organophilic boehmite rods*, J. Phys. Chem. **97**, 11510 (1993).

[80] E. B. Steager, C.-B. Kim, and M. J. Kim, *Dynamics of pattern formation in bacterial swarms*, Phys. Fluids **20**, 073601 (2008).

[81] L.-s. Li et al., *Isotropic-liquid crystalline phase diagram of a CdSe nanorod solution*, J. Chem. Phys **120**, 1149 (2004).

[82] H. Maeda and Y. Maeda, *Direct observation of brownian dynamics of hard colloidal nanorods*, Nano Lett. **7**, 3329 (2007).

[83] J. He, J. Viamontes, and J. X. Tang, *Counterion-induced abnormal slowdown of f-actin diffusion across the isotropic-to-nematic phase transition*, Phys. Rev. Lett. **99**, 068103 (2007).

[84] M. Van Bruggen, H. N. Lekkerkerker, G. Maret, and J. K. Dhont, *Long-time translational self-diffusion in isotropic and nematic dispersions of colloidal rods*, Phys. Rev. E **58**, 7668 (1998).

[85] P. S. Russo et al., *Self-diffusion of a semiflexible polymer measured across the lyotropic liquid-crystalline-phase boundary*, J. Chem. Phys **111**, 1746 (1999).

[86] M. P. Lettinga, E. Barry, and Z. Dogic, *Self-diffusion of rod-like viruses in the nematic phase*, Europhys. Lett. **71**, 692 (2005).

[87] D. Frenkel and R. Eppenga, *Evidence for algebraic orientational order in a two-dimensional hard-core nematic*, Phys. Rev. A **31**, 1776 (1985).

[88] P. Bolhuis and D. Frenkel, *Tracing the phase boundaries of hard spherocylinders*, J. Chem. Phys **106**, 666 (1997).

[89] R. Hentschke, L. Askadskaya, and J. Rabe, *A simple model for dense phases of two-dimensional hard rods and its application to mono-and bidisperse alkanes physisorbed on graphite*, J. Chem. Phys **97**, 6901 (1992).

[90] A. Stroobants, *Liquid crystal phase transitions in bidisperse hard-rod systems*, J. Phys. Condens. Matter **6**, A285 (1994).

[91] T. Odijk and H. N. Lekkerkerker, *Theory of the isotropic-liquid crystal phase separation for a solution of bidisperse rodlike macromolecules*, J. Phys. Chem. **89**, 2090 (1985).

[92] P. Sollich, *Predicting phase equilibria in polydisperse systems*, J. Phys. Condens. Matter **14**, R79 (2002).

[93] R. F. Kayser and H. J. Raveché, *Bifurcation in Onsager's model of the isotropic-nematic transition*, Phys. Rev. A **17**, 2067 (1978).

[94] W. H. Press, *Numerical recipes 3rd edition: The art of scientific computing*, Cambridge University Press, 2007.

[95] W. K. Hastings, *Monte Carlo sampling methods using Markov chains and their applications*, Biometrika **57**, 97 (1970).

[96] N. Metropolis, A. W. Rosenbluth, M. N. Rosenbluth, A. H. Teller, and E. Teller, *Equation of State Calculations by Fast Computing Machines*, J. Chem. Phys **21**, 1087 (1953).

[97] S. Kamiyama and A. Satoh, *Rheological properties of magnetic fluids with the formation of clusters: analysis of simple shear flow in a strong magnetic field*, J. Colloid Interface Sci. **127**, 173 (1989).

[98] F. W. Starr, J. F. Douglas, and S. C. Glotzer, *Origin of particle clustering in a simulated polymer nanocomposite and its impact on rheology*, J. Chem. Phys **119**, 1777 (2003).

[99] D. Susan-Resiga et al., *The influence of particle clustering on the rheological properties of highly concentrated magnetic nanofluids*, J. Colloid Interface Sci. **373**, 110 (2012).

[100] A. Baskaran and M. C. Marchetti, *Self-regulation in self-propelled nematic fluids*, Eur. Phys. J. E **35**, 1 (2012).

[101] A. Peshkov, I. S. Aranson, E. Bertin, H. Chaté, and F. Ginelli, *Nonlinear Field Equations for Aligning Self-Propelled Rods*, Phys. Rev. Lett. **109**, 268701 (2012).

[102] J. Stenhammar, D. Marenduzzo, R. J. Allen, and M. E. Cates, *Phase behaviour of active Brownian particles: the role of dimensionality*, Soft Matter **10**, 1489 (2014).

[103] G. Vliegenthart and H. N. Lekkerkerker, *Predicting the gas–liquid critical point from the second virial coefficient*, J. Chem. Phys. **112**, 5364 (2000).

[104] F. Abraham, *Homogeneous nucleation theory: the pretransition theory of vapor condensation*, volume 1, Elsevier, 2012.

[105] E. B. Moore and V. Molinero, *Structural transformation in supercooled water controls the crystallization rate of ice*, Nature **479**, 506 (2011).

[106] M. Marchetti et al., *Hydrodynamics of soft active matter*, Rev. Mod. Phys. **85**, 1143 (2013).

[107] V. Schaller and A. R. Bausch, *Topological defects and density fluctuations in collectively moving systems*, Proc. Natl. Acad. Sci. U.S.A. **110**, 4488 (2013).

[108] A. Speranza and P. Sollich, *Simplified Onsager theory for isotropic–nematic phase equilibria of length polydisperse hard rods*, J. Chem. Phys **117**, 5421 (2002).

[109] N. Clarke, J. A. Cuesta, R. Sear, P. Sollich, and A. Speranza, *Phase equilibria in the polydisperse Zwanzig model of hard rods*, J. Chem. Phys **113**, 5817 (2000).

[110] T. J. Sluckin, *Polydispersity in liquid crystal systems*, Liq. Cryst. **6**, 111 (1989).

[111] G. J. Vroege and H. N. W. Lekkerkerker, *Theory of the isotropic-nematic-nematic phase separation for a solution of bidisperse rodlike particles*, J. Phys. Chem. **97**, 3601 (1993).

[112] S. Varga and I. Szalai, *Phase diagrams of binary mixtures of hard rods in an external orientational field*, Phys. Chem. Chem. Phys. **2**, 1955 (2000).

[113] D. S. Massey and N. A. Denton, *The dimensions of residential segregation*, Soc. Forces **67**, 281 (1988).

[114] L. Onsager, *Crystal statistics. I. A two-dimensional model with an order-disorder transition*, Phys. Rev. **65**, 117 (1944).

[115] J. Tailleur and M. E. Cates, *Statistical Mechanics of Interacting Run-and-Tumble Bacteria*, Phys. Rev. Lett. **100**, 218103 (2008).

[116] Y. Fily and M. C. Marchetti, *Athermal Phase Separation of Self-Propelled Particles with No Alignment*, Phys. Rev. Lett. **108**, 235702 (2012).

[117] A. Wysocki, R. G. Winkler, and G. Gompper, *Cooperative motion of active Brownian spheres in three-dimensional dense suspensions*, EPL **105**, 48004 (2014).

[118] Y. Hatwalne, S. Ramaswamy, M. Rao, and R. A. Simha, *Rheology of active-particle suspensions*, Phys. Rev. Lett. **92**, 118101 (2004).

[119] R. Aditi Simha and S. Ramaswamy, *Hydrodynamic fluctuations and instabilities in ordered suspensions of self-propelled particles*, Phys. Rev. Lett. **89**, 058101_1 (2002).

[120] T. B. Liverpool and M. C. Marchetti, *Rheology of Active Filament Solutions*, Phys. Rev. Lett. **97**, 268101 (2006).

[121] P.-G. De Gennes, *Scaling concepts in polymer physics*, Cornell University Press, 1979.

Acknowledgements

Writing the acknowledgements for this thesis is no easy task. Fortunately, I was far from being alone in what I did during my PhD work. I would like to thank many people from whom I learned, the organizations that provided the necessary infrastructure, the places that gave me the comfort and concentration to work, and the developers who provided the tools I used for this thesis.

First and foremost, I would like to give my warmest thanks to my supervisor, Dr. Thorsten Auth. He was there for me every time I needed help, and he gave me new scientific ideas, encouragement, help with technical problems, and he even sometimes sat with me to debug my code. Thorsten did an amazing job of withstanding my mistakes, stupidities, and stubbornness for almost four years!

Also, I would like to thank my other supervisor, Prof. Dr. Gerhard Gompper, for giving me the opportunity to do my PhD here in the Research Center Jülich. Gerhard provided me with core ideas for my PhD project, and he was always my ultimate point of trust in everything that could happen during my work. In our many meetings and discussions, he helped me with his deep insight in physics to find my way in the complex field of my research topic.

I am grateful to many other colleagues and friends, and I am afraid I cannot do justice in thanking all of them in such a short time. I specially thank Kristian Marx, Philippe Roelli, Adam Wysocki, Guglielmo Saggiorato, Matti Peltomäki, Chien-Cheng Huang, Roland G. Winkler, Andrea Costanzo, Jens Elgeti, Helga Paffen, Josef Heinen, Dorothea Henkel, Elmar Westphal, and the entire Institute of Complex Systems and the Institute for Advanced Simulation (ICS-2/IAS-2) in the Research Center Jülich. I had a great time with a lot of fun in my office with Sabyasachi Dasgupta, and I am grateful for his many suggestions and advice on numerous scientific and unscientific issues. I also thank my old friend, Nima H. Siboni, for all the inspiration that he gave me since high school to the very day of my oral exam, and also for all the friendly (and at the same time hardcore scientific!) conversations that we had all these years.

I had the opportunity to be a member of the International Helmholtz Research School for Biophysics and Softmatter (IHRS-BioSoft). Being in this interdisciplinary school helped me to learn many theoretical and experimental concepts in physics, biology, and chemistry. I specially enjoyed the interesting lectures of Prof. Jan K. G. Dhont, Prof. Dr. Frank Müller, Jun.-Prof. Dr. Birgit Strodel, and stimulating discussions with my fellow students Axel Baumann, Falk Hoffmann, Donald Guu, and many others. I am also grateful to the Jülich Supercomputing Center (JSC) who provided me with the computational facilities, which was crucial in the completion of my PhD project.

Having a friendly and productive working environment is essential in doing research. I was lucky enough to spend most of my PhD time in "our" building, the Building No. 04.16, where I felt that we were all living and working like a family. In addition, I also worked frequently from outside of the office, where I

could enjoy (and get concentration from) the “white noise” from the strangers in restaurants, coffee shops, and trains. I would like to thank all of those strangers who (unintentionally) helped me to fix numerous bugs in my code, to write major parts of my thesis, and to read all the papers I could otherwise never read. I specifically thank Café Libresso (Fleischmengergaße 29 Köln) and my deceased friend Bijan Dadgari, the DB ServiceStore in the Düren train station, the Goldmund Literaturcafé (Glasstraße 2 Köln), and finally, the regional trains RE1 and RE9, for their long delays but comfortable and mostly empty seats.

My research topic demanded heavy use of high performance computing and scientific visualization. Although the tools that I used were often giant computer programs with very complicated functionality, many of them were written and developed by volunteer programmers from all around the world. As complicated as these programs were, the developers shared them without any restriction in running, modifying, sharing exact copies, or redistributing modified versions. I am indebted to all those programmers, who provided such great tools, and at the same time, respected the freedom of the users like me to control my own computing. Specifically, I benefited most from the developers of the great visualization software “gnuplot,” the GNU Compiler Collection “GCC,” the graphic programs “ImageMagick,” “Inkscape,” and “mencoder,” the spreadsheet application “LibreOffice Calc,” the typesetting engine “XeLaTeX,” the GNU/Linux distribution “Ubuntu,” and above all, the GNU project and its founder Richard M. Stallman who started the whole free software movement back in 1983.

Last but not least, I would like to thank my family for all the support they gave me all through the years. First, my parents, who raised me with love, fun, and discipline. I thank my mother, Seddigheh Banakar Moghaddam, for her patience, and for everything that are beyond words and I myself may never know. I thank my father, Ghasemali Pourmousa Abkenar, for all his advice to be persistent, to not lose hope in the way of learning, and also for showing me the power of small habits. I thank my two brothers and two sisters, for teaching countless things in life to their little brother. And finally, I thank my old friend, fellow PhD student, scientific consultant, weekend office-mate, thesis proofreader, fellow life-passenger, and beloved wife, Maryam.

Erklärung

Ich versichere, daß ich die von mir vorgelegte Dissertation selbständig angefertigt, die benutzten Quellen und Hilfsmittel vollständig angegeben und die Stellen der Arbeit—einschließlich Tabellen, Karten und Abbildungen—, die anderen Werken im Wortlaut oder dem Sinn nach entnommen sind, in jedem Einzelfall als Entlehnung kenntlich gemacht habe; daß diese Dissertation noch keiner anderen Fakultät oder Universität zur Prüfung vorgelegen hat; daß sie—abgesehen unten angegebenen Teilpublikationen—noch nicht veröffentlicht worden ist sowie, daß ich eine solche Veröffentlichung vor Abschluß des Promotionsverfahrens nicht vornehmen werde. Die Bestimmungen der Promotionsordnung sind mir bekannt. Die von mir vorgelegte Dissertation ist von Professor Gompper betreut worden.

1. Masoud Abkenar, Kristian Marx, Thorsten Auth, and Gerhard Gompper
   Collective behavior of penetrable self-propelled rods in two dimensions
   Phys. Rev. E **88,** 062314 (2013)

Jülich, den 5. Mai 2014